GALACTIC AND ANOMALOUS COSMIC RAYS IN THE INNER HELIOSPHERE: HELIOS E6 RESULTS

Dissertation
zur Erlangung des Doktorgrades
der Mathematisch-Naturwissenschaftlichen Fakultät
der Christian-Albrechts-Universität zu Kiel
vorgelegt von

JOHANNES MARQUARDT

– Kiel, 2019 –

Johannes Marquardt:
Galactic and Anomalous Cosmic Rays in the inner heliosphere: HELIOS E6 results,

ERSTER GUTACHTER (SUPERVISOR):
Prof. Dr. Bernd H. Heber

ZWEITER GUTACHTER :
Prof. Dr. Wolfgang Dröge

TAG DER MÜNDLICHEN PRÜFUNG:
25.11.2019

With magic, you can turn a frog into a prince. With science, you can turn a frog into a Ph.D and you still have the frog you started with.

— Terry Pratchett, The Science of Discworld

ABSTRACT

With *Parker Solar Probe* [Fox et al., 2016] and *Solar Orbiter* [Müller et al., 2013] there will be measurements in the inner heliosphere available in the near future. Over 40 years ago, the HELIOS mission was launched with the goal to improve our understanding of the inner heliosphere as well. While the two missions will drastically improve the availability of data, it seems worthwhile to revisit the HELIOS mission data to provide a unique dataset that will expand the upcoming data.

In this work, the measurements of the Experiment 6 (E6), one of three particle instruments on-board HELIOS was revisited and reanalysed. The E6 was capable of measuring electrons in the low MeV and elements from hydrogen to magnesium in the MeV to GeV range.

The data were completely recalibrated by using a sophisticated model of the instrument as well as taking into account effects like degrading of the detectors, complex temperature dependent behaviour and non-linearities of the detectors. All of these effects have been quantified and the properties of the installed optical detector have been obtained.

It is shown that with these data energy spectra of the different elements can be obtained in dependence of time and radial distance from the spacecraft to the Sun. From the hydrogen spectra the modulation parameter for the analysed time period was determined, which agrees with expectations for the analysed period of time. The gradient for anomalous oxygen was determined for the first time in the inner heliosphere and is with $(48 \pm 12)\%/\mathrm{AU}$ much larger than expected from measurements in the outer heliosphere. It agrees qualitatively with recent models of solar modulation. The gradient of galactic hydrogen above 200 MeV was determined to be $(2 \pm 2.5)\%/\mathrm{AU}$. This value agrees well with other measurements and predictions.

With the obtained recalibration it is also possible to analyse Solar Energetic Particle (SEP) events as well as spectra of elements heavier than helium up to very high energies.

ZUSAMMENFASSUNG

Mit *Parker Solar Probe* [Fox et al., 2016] und *Solar Orbiter* [Müller et al., 2013] werden in Kürze Messungen aus der inneren Heliosphäre vorliegen. Bereits vor über 40 Jahren startete die HELIOS Mission, ebenfalls mit dem Ziel, unser Verständnis der inneren Heliosphäre zu verbessern. Zwar werden die beiden Missionen die Datenlage drastisch verbessern, es erscheint aber dennoch sinnvoll, die HELIOS Mission erneut zu untersuchen um die neuen Messungen zu erweitern.

In dieser Arbeit werden die Messungen des E6, eines von drei Teilcheninstrumenten auf HELIOS, neu aufgearbeitet und ausgewertet. Das E6 konnte Elektronen im niedrigen MeV Bereich und Elemente von Wasserstoff bis Magnesium im MeV bis GeV Bereich messen.

Es wird gezeigt, dass mit diesen Daten die Energiespektren der verschiedenen Elemente in Abhängigkeit von Zeit und und radialem Abstand zwischen Sonde und Sonne gewonnen werden können. Aus den Wasserstoff-Spektren wurde der Modulationsparameter für den analysierten Zeitraum bestimmt, welcher gut mit den Erwartungen für diesen Zeitraum übereinstimmt. Der Gradient für Anomalen Kosmischen Sauerstoff wurde zum ersten Mal für die innere Heliosphäre bestimmt und ist mit $(48 \pm 12)\%/\mathrm{AU}$ deutlich größer als, ausgehend von Messungen in der äußeren Heliosphäre, bisher angenommen. Er stimmt allerdings qualitativ mit neuen Modellen der solaren Modulation überein. Der Gradient von galaktischem Wasserstoff über 200 MeV wurde auf $(2 \pm 2.5)\%/\mathrm{AU}$ bestimmt. Dieser Wert stimmt sowohl mit anderen Messungen als auch Vorhersagen gut überein.

Mit den in dieser Arbeit entwickelten Datenrekalibrationsmethode ist es außerdem möglich, solare Teilchenereignisse und die Spektren bei sehr hohen Energien von Elementen, die schwerer als Helium sind, zu bestimmen.

PUBLICATIONS: PEER REVIEWED

Galactic cosmic ray hydrogen spectra and radial gradients in the inner heliosphere measured by the HELIOS Experiment 6
J. Marquardt, B. Heber, Astronomy & Astrophysics, Volume 625, id.A153, 7 pp,(2019), DOI: 10.1051/0004-6361/201935413
Own contribution: 90%

Data based correction of HELIOS E6 Measurements - Proton Contamination of relativistic electron measurements
M. Hörlöck, B. Heber, J. Marquardt and P. Kühl, Central European Astrophysical Bulletin(2019), accepted for publication
Own contribution: 40%

Energy spectra of carbon and oxygen with HELIOS E6. Radial gradients of anomalous cosmic ray oxygen within 1 AU
J. Marquardt, B. Heber, M. S. Potgieter, R. D. Strauss, Astronomy & Astrophysics, Volume 610, id.A42, 5 pp.(2018), DOI: 10.1051/0004-6361/201731490 Own contribution: 80%

GEANT 4 simulation of the Helios cosmic ray telescope E6: Feasibility of chemical composition studies
J. Marquardt, B. Heber, M. Hörlöck, P. Kühl, R.F. Wimmer-Schweingruber, Journal of Physics: Conference Series, Volume 632, Issue 1, article id. 012016 (2015), DOI: 10.1088/1742-6596/632/1/012016
Own contribution: 80%

PUBLICATIONS: NOT REVIEWED

Near-real time forecasts of MeV protons based on sub-relativistic electrons: communicating the outputs to the end users
C. Sarlanis, B. Heber, J. Labrenz, P. Kühl, J. Marquardt, J. Dimitroulakos, A. Papaioannou, A. Posner, 19th EGU General Assembly, EGU2017, proceedings from the conference held 23-28 April, 2017 in Vienna, Austria., p.17174 Own contribution: 5%

The chemical composition of galactic cosmic rays during solar minimum of solar cycle 20/21 - Helios E6 results
J. Marquardt, B. Heber, P. Kühl, R.F. Wimmer-Schweingruber, Proceedings of the 34th International Cosmic Ray Conference (ICRC2015) id.123 Own contribution: 85%

CONTENTS

ACRONYMS

E6 Experiment 6

ACR Anomalous Cosmic Ray

GCR Galactic Cosmic Ray

IMP Interplanetary Monitoring Platform

GEANT GEometry And Tracking

SEP Solar Energetic Particle

GLE Ground Level Enhancement

CPME Charged Particle Measurements Experiment

PHA Pulse Height Analysis

CIR Corotating Interaction region

PMT photomultiplier

AU Astronomical Unit

GLE Ground Level Enhancement

MIP Minimal Ionizing Particle

FFS Force Field Solution

ADC Analog-to-digital converter

INTRODUCTION

The HELIOS mission was a collaboration between the Bundesrepublik Deutschland (BRD) and the United States of America (USA) in the 1970s. Two nearly identical, spinning spacecraft were launched into the inner heliosphere in the ecliptic. Among their payload was the Experiment 6 (E6), a particle instrument designed and built in the Christian-Albrechts-Universität zu Kiel. HELIOS A collected data from the 10th of December 1974 to the 16th of June 1986 while HELIOS B collected data from 15th of January 1976 to the 3rd of March 1980. These data will be subject of this work.

"Why revisit such old data?" is the most important question to answer in this thesis.

First, the most obvious reason: Every point of data matters in this field. To study the heliosphere, in an optimal situation there would be a fleet of spacecrafts covering every thinkable angle and distance from the Sun, at all times. While we may approach this situation in the future, in the current situation we have very few snapshots at very distinct positions at the heliosphere.

The second reason is the uniqueness of the HELIOS mission: Two nearly identical spacecraft were launched in the 1970s to explore the heliosphere within mercury's orbit. Since the heliosphere is far from being static, it is desirable to analyse data from different time periods, so the very early date of this mission is an advantage to point out. Having the data from two spacecraft makes it possible to investigate spatial phenomena with the same set of instrumentation.

So if the data are valuable, why is there still analysis to be done? In fact, the HELIOS data was analysed and used continuously since the mission launch. But because no spacecraft had been so close to the Sun before, people didn't know what exactly to expect and models had to be developed or adapted to explain the measured data. Furthermore, our possibilities and understanding have increased dramatically since the mission start: computing power, particle matter interaction cross-sections, understanding of effects like quenching in scintillators etc. So with new analysis methods and the opportunity to compare the data to new, similar missions data, there are enough reasons to take yet another look on the data.

In this thesis, the data will be re-processed completely and particle fluxes and gradients will be determined. These quantities will be compared to different instrument data as well as to theory.

The main scientific goal of this analysis is the investigation of the interaction between particles originating outside the heliosphere and the solar wind, more specifically how the magnetic field of the so-

lar wind influences the Galactic Cosmic Rays (GCRs) and Anomalous Cosmic Rays (ACRs).

The understanding of the interaction between particles and magnetic fields in space is crucial for the understanding the propagation of every particle in space, from the solar wind to the galactic cosmic rays travelling between galaxies.

1

SCIENTIFIC BACKGROUND

The heliosphere is populated by different particles of different origin. In Figure 1 all those different origin spectra are shown on the example of oxygen. Shown as the blue curve is the fluence accumulated over roughly 2 years, consisting of oxygen particles of every known origin. In the range from 0.3 to 100 MeV/nuc the spectrum results from superposition of different acceleration mechanisms inside the heliosphere. At low energies we mostly find particles originating from the Sun, the solar wind. At energies above 100 MeV/nuc every species but GCR plays a very minor role.

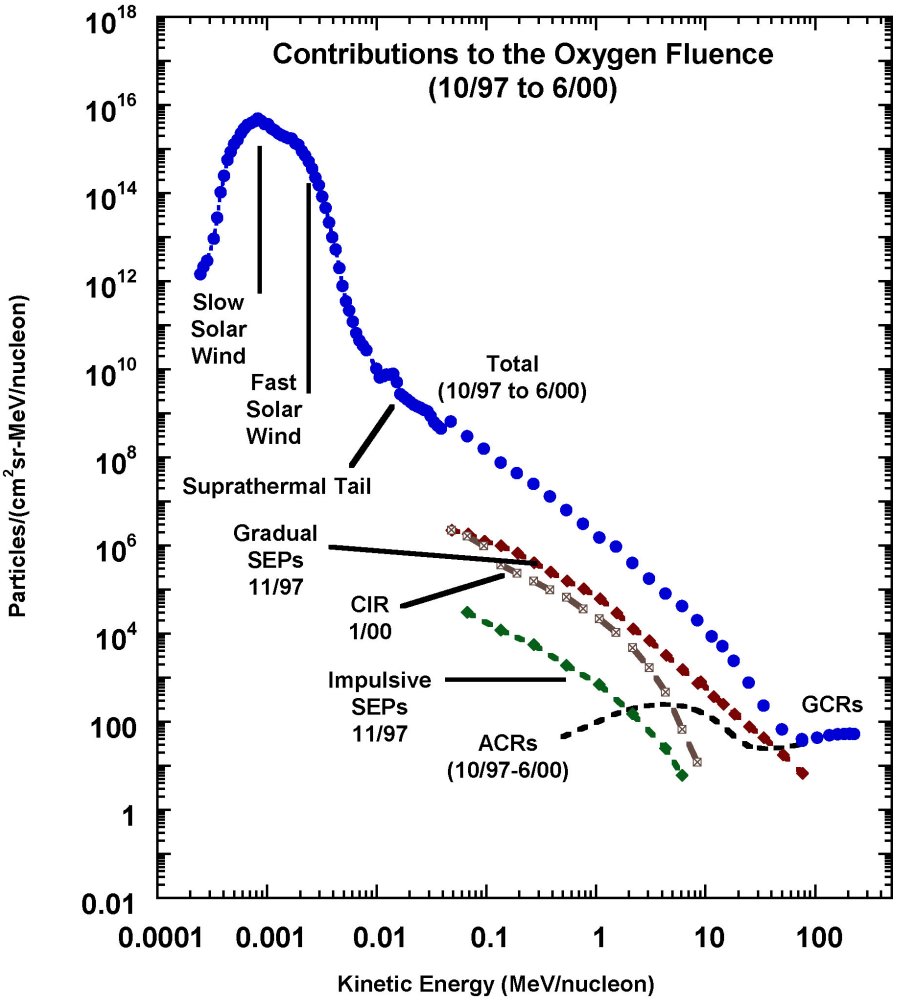

Figure 1: time-integrated intensity (fluence) of oxygen from 300 eV/nucleon to 300 MeV/nucleon[Mewaldt, 2003]

1

This work concentrates on the spectra of oxygen, carbon and hydrogen in the energy range from > 4 MeV/nuc up to > 100 MeV/nuc. Those particles are mainly GCR, ACR or particles accelerated by Corotating Interaction region (CIR) or by Solar Energetic Particle (SEP) events. This last type of particles is beyond the focus of this work, however, since SEP events do not give much information about the modulation of particles by the solar Wind.

GCRs are fully ionized particles originating outside the heliosphere. Their flux is assumed to be isotropic and constant in time before they enter the heliosphere. They consist to 90% of hydrogen with the remaining 10% being heavier elements as well as electrons, positrons and antiprotons.

ACRs originate from neutral interstellar particles being ionized in the vicinity of the Sun, so called pick-up ions [Pogorelov et al., 2017]. These ions propagate with the solar wind to the outer heliosphere, where they are accelerated and propagate back. The source of this acceleration was assumed to be shock acceleration at the Termination Shock. When Voyager crossed the Termination Shock and no sign of a drastic change in the anomalous oxygen flux could be found, this theory has been ruled out and the acceleration process is unclear and under investigation [Senanayake et al., 2015].

1.1 INTERACTION OF PARTICLES WITH MATTER AND THEIR MEASUREMENT

Every charged particle passing through matter looses energy due to the Coulomb collisions with the shell electrons. This interaction can be understood as inelastic collisions between the passing particle and the electrons. The electrons are excited or detached from their atom. While the particle also interacts with the positively charged nuclei, the energy transfer is usually negligible compared to the before mentioned.

For energies above 1 MeV the energy loss by this inelastic collisions can be determined fairly accurately by the Bethe-Bloch-Formula [Longair, 1992]. Figure 2 displays the relation between β, kinetic energy and energy loss of a proton in silicon. The energy loss shows a global minimum at roughly 3 times the rest energy of the proton. Particles with those energies are thus called Minimal Ionizing Particles (MIPs).

$$-\frac{dE}{dx} = \frac{4\pi}{m_e c^2}\left(\frac{e^2}{4\pi\epsilon_0}\right)^2 \cdot \frac{nz^2}{\beta^2} \cdot \left[\log\left(\frac{2m_e c^2\beta^2}{I(1-\beta^2)}\right) - \beta^2\right]$$

v = speed of the particle
z = charge of particle in multiples of electron charge
c = speed of light
β = $\frac{v}{c}$
m_e = mass of the electron
ϵ_0 = vacuum permittivity
e = electron charge
n = electron number density
I = mean excitation potential

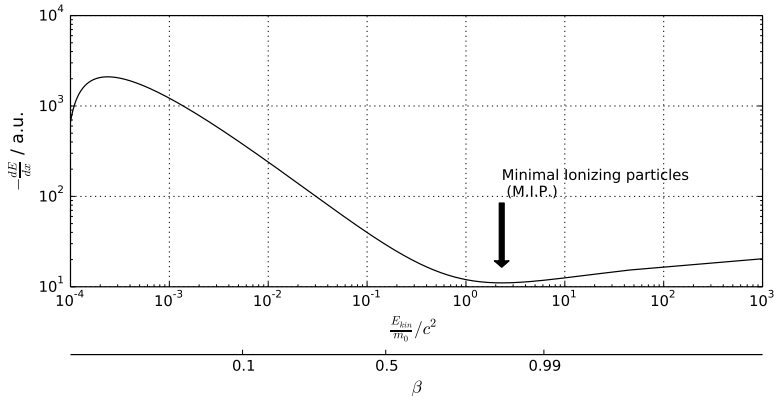

Figure 2: energy transfer per unit length of protons in silicon in arbitrary units

1.1.1 *Anorganic Scintillator*

In an insulator or semiconductor, electrons only have discrete bands available: The lower valence band, where electrons are bound to the lattice, and the conduction band, where electrons can perform elastic scattering.

An electron can move from the valence band to the conduction band by absorbing energy, from ionizing radiation for example. By returning to a position in the valence band, the energy difference can be emitted as a photon.

Since the energy of the emitted photon is in the same order of magnitude as the band gap, those photons can be absorbed by other electrons in the material, so called self-absorption, making this a rather inefficient process. The efficiency can be enhanced by adding impurities in the crystal, so called activators. The band gab of those activators is smaller than the gap of the base material, making the emitted energy during de-excitation smaller and thus preventing self-absorption[Knoll, 2000], see Figure 3.

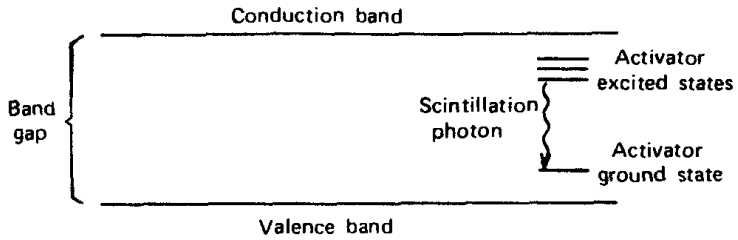

Figure 3: Energy structure of an activated crystalline scintillator [Knoll, 2000]

There are possible radiation-free transitions as well as transitions with energies much different from the desired visible light. The probability of those transitions is not constant, but may vary depending on dE/dx and charge of a incident particle.

This results in non-linearities between deposited energy and the total amount of emitted light in a certain wavelength range, called quenching.

The scintillator is optically coupled to a photomultiplier (PMT) as shown in Figure 4. In the photocathode, an electron is emitted via photo-ionization. This electron is accelerated by a high voltage, typically around 1kV. The accelerated electron hits dynode 1 in the picture, producing several new free electrons in the process. Those electrons are accelerated as well and hit the next dynode. So a cascade develops, amplifying the initial signal by $\sim 10^6$.

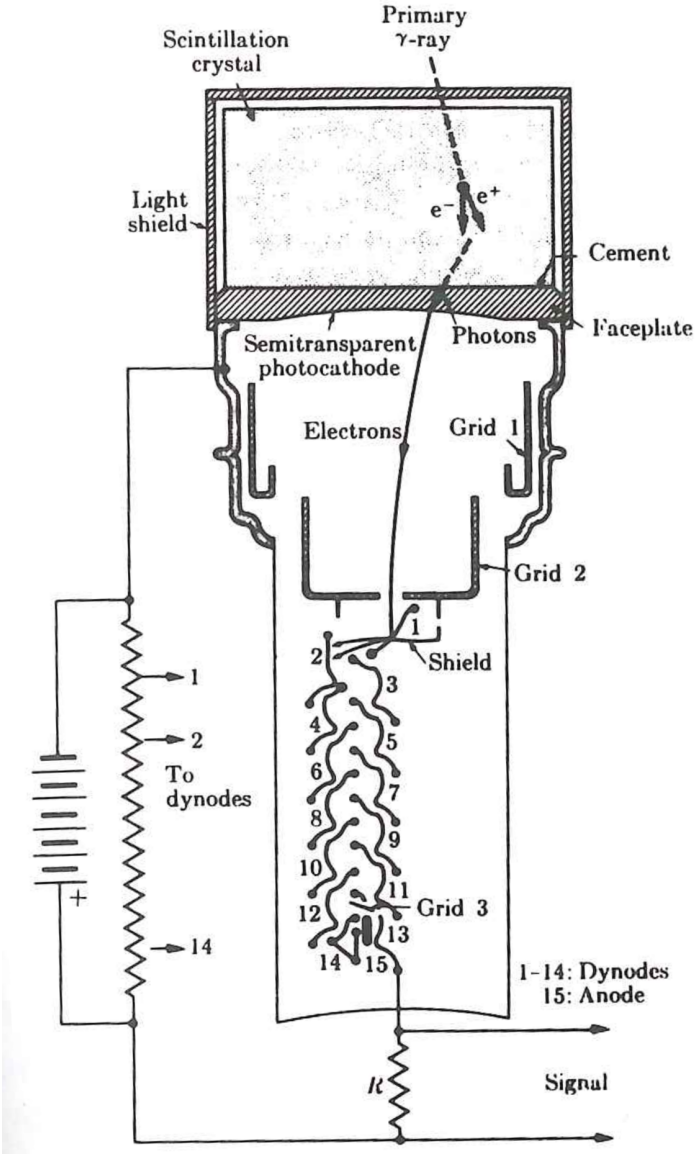

Figure 4: A scintillation detector showing the large scintillating crystal and the photomultiplier tube[Enge, 1966]

1.1.2 *Solid State Detector*

In Figure 5 the basic band structure of insulators and semiconductors is shown. The number of electrons exactly matches the number of available sites in the valence band. However, at temperatures different from zero, electrons from the valence band can gain sufficient energy to be elevated to the conduction band. This process creates a electron in the otherwise free conduction band and an empty place, called hole, in the otherwise completely filled valence band. Both the electron and the hole can move under the influence of an electric field

which increases the conductivity of a semiconductor with increasing temperature.

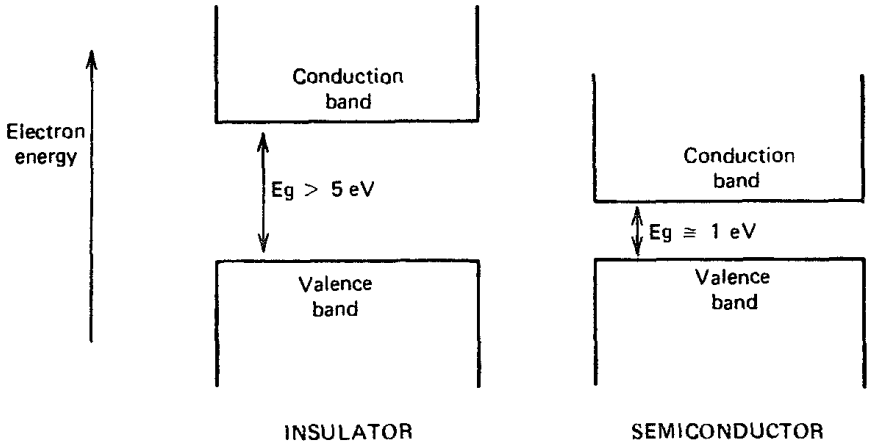

Figure 5: Band structures for electron energies in insulators and semiconductors [Knoll, 2000]

In a pure semiconductor, the number of holes and electrons are always equal. Doping the material will tip the equilibrium in favour of one charge carrier. The electrons in the conduction band and the holes in the valence band will migrate until they reach an electrode or recombine.

This diffusion of charge carriers can surpass the junction of a p-doted and an n-doted semi-conductor. After passing the junction, the charge carriers will recombine, thereby removing free charge carriers and creating a net charge. This charge will eventually prevent further charge carriers from passing the junction. The so formed region will not have free charge carries left and is called depletion zone.

By applying a voltage the size of this depletion zone can now be increased, see Figure 6. Ionizing radiation produces an equal number of electrons and holes, which will migrate to their corresponding electrodes. This electric current is integrated over time, resulting in a linear dependency of deposited energy and integrated current.

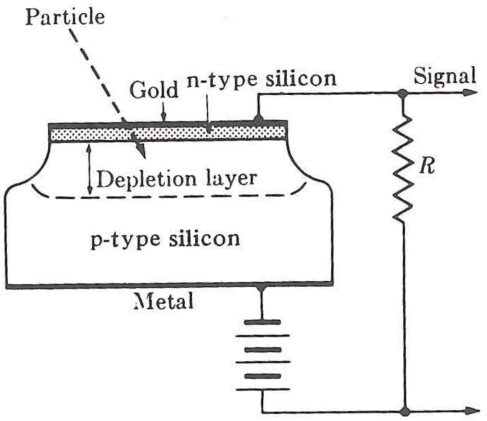

Figure 6: A schematic diagram of a basic semiconductor, solid state detector[Enge, 1966]

1.1.3 *Cerenkov-Detector*

Charged particles moving through dielectric matter with a higher speed than the phase velocity of light in that matter emit photons, called Cerenkov-Radiation.

When a particle's speed v_p is higher than the phase velocity of electromagnetic radiation c in the medium with refraction index n

$$\frac{c}{n} < v_p$$

the particle overtakes it's own electromagnetic field, like a jet fighter overtaking it's own sound. From this results, like in the analogy, a shock front.

The photons are emitted with a constant angle

$$\beta = \frac{v_p}{c}$$

as a stark contrast to the isotropically emitted photons from scintillation, though both radiation types usually have the same wavelength.

Because of this, it is not possible to distinguish between photons emitted by Cerenkov-Radiation and Scintillation.

2

THE HELIOS EXPERIMENT 6

All analysed data in this thesis were gathered by the E6 instrument which was mounted on both HELIOS spacecraft.

2.1 THE HELIOS MISSION

The two HELIOS space probes were launched into highly eccentric, elliptic orbits in the ecliptic on 10.06.1974 and 15.01.1976 between roughly 0.3 and 1 Astronomical Unit (AU), see Figure 7. HELIOS 1 lost contact in March 1986 while HELIOS 2 lost contact 6 years earlier in March 1980. They were spinning around the axis that is perpendicular to the ecliptic, at 60 rpm. On board they carried 12 experiments to investigate the inner heliosphere, which can be divided into three groups with different objectives:

- Investigation of plasma and electromagnetic fields (E1-E5)
  - measurements of the energy spectra and angular distribution of electrons, protons and α-particles
  - measurement of the magnetic field up to 5 Hz and magnetic field oscillations up to 2 kHz
  - measurement of electric field oscillations up to 3 MHz
- Investigation of cosmic rays (E6-E8)
  - measurement of mass, energy and angular distribution of cosmic rays
  - observation of solar x-ray activity
  - registration of galactic and extragalactic gamma-ray bursts
- Investigation of micrometeorites and dust (E9-E12)
  - measurement of the intensity and polarization of zodiacal light
  - determination of the intensity of dust particles in interplanetary space
  - determination of mass, velocity and composition of micrometeorites

In this thesis data from the E6 were recalibrated and analysed.

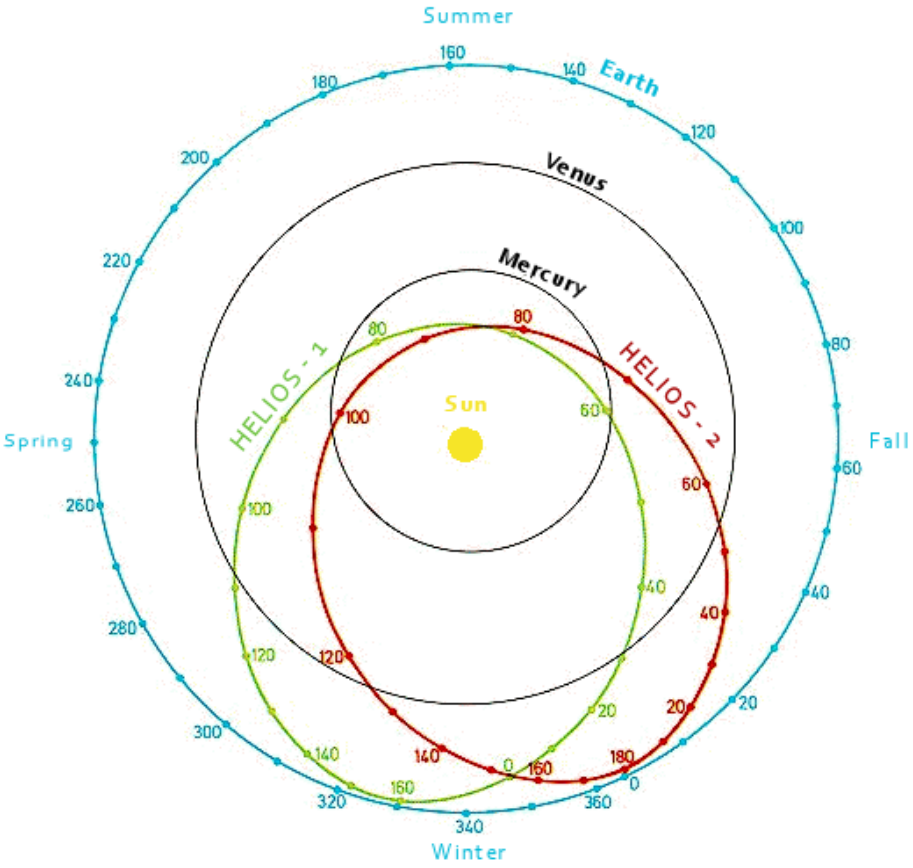

Figure 7: Helios 1 and Helios 2 trajectory around the Sun[NASA, 2004]

2.2 EXPERIMENT 6 SETUP AND DATA PRODUCTS

A detailed description of the E6 instrument can be found in [Kunow et al., 1981] and [Mueller-Mellin et al., 1982]. The E6 had been build as a particle telescope to measure ionizing particles, ions as well as electrons. A particle telescope consists of at least two detectors which store information about the deposited energy in each detector. Since charge z and speed v determine the energy loss of the particles, different species as well as isotopes result in different deposited energy patterns in the detectors of the telescope: v is not constant as the particle looses energy in the detector, this allows conclusions about z, atomic mass A and energy E of the particle.

The E6 consists of 7 detectors: 5 semiconductor detectors (D1-D5) and an undoped sapphire (often called Cerenkov-detector or detector C) arranged as a telescope and a plastic scintillator as anti-coincidence as shown in Figure 8. The signals of the sapphire and the anti-coincidence are read out by two separated PMTs: One directly below the Cerenkov-detector and one at the side of the plastic anti-coincidence. The two

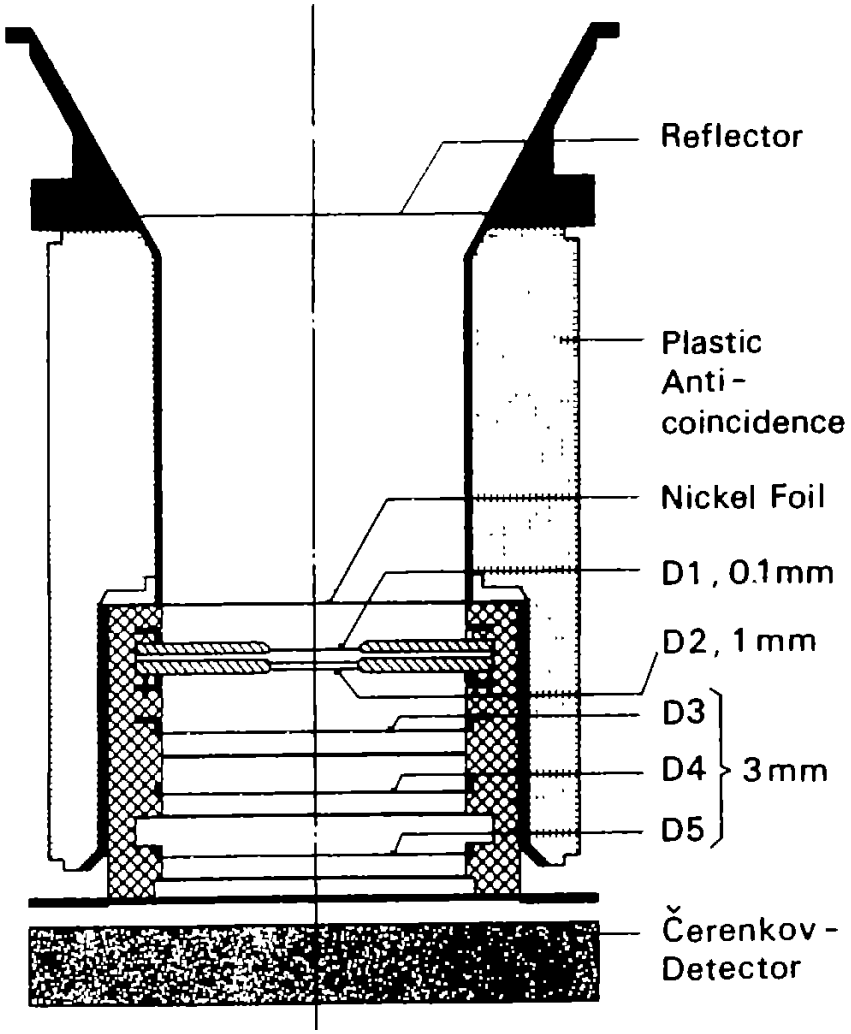

Figure 8: sketch of the E6 detector. Adapted from [Heber, 1991]

foils keep light and dust out of the detector and are otherwise passive materials.

properties of particles that get stuck in one of the silicon detectors and come from the front can be determined easily: In this case the total energy of the particle roughly corresponds to the sum of deposited energies. The information about the deposited energy in a detector is called Pulse Height Analysis (PHA) data (see next section). It is usually enough to also determine z and A, see e.g. [Marquardt et al., 2015].

Since the sapphire was not doped, the photon number from scintillation and the Cerenkov-effect fall in the same order of magnitude. Cerenkov-Radiation is only emitted for particles with a very high speed, so for low energies the detector functions only as a scintillator: The number of emitted photons is (roughly) proportional to the deposited energy.

On top and on the sides of the sapphire a layer of epoxy has been applied to absorb photons in the visible range. Since Cerenkov-Radiation is highly anisotropic, mainly in the direction of the particle trajectory, while scintillated photons are isotropic, this results in an angular dependence for the total number of registered photons for particles fast enough to produce Cerenkov-Radiation. High energy particles penetrating the detector from the front produce the same number of photons and deposit the same energy in every detector as particles penetrating from the back. However a large share of the photons produced by backwards particles is absorbed by the epoxy, so the total number of **registered** photons differs. This allows for forwards-backwards discrimination of relativistic particles.

All PHA data from particles which also hit the last detector are stored in the so-called integral channel. For those particles it is difficult to determine their initial energy when entering the detector. The procedure is described in detail in [Marquardt and Heber, 2019].

One has to keep in mind that because of limited telemetry bandwidth it was impossible to send the PHA data for every particle via telemetry. So, every particle event was also be classified onboard the spacecraft in a much broader way: By implementing thresholds for every detector. Every detector has two thresholds. Depending on the thresholds that were exceeded, the event is assigned an energy range and one of the three particle types following a (simplified) logic:

- electron, if detector 1 was below all thresholds
- proton, if every detector was between the lower and upper threshold
- (heavier than protons) ion, if one detector exceeded it's upper threshold

These classifications are called channels and for every particle event the assigned channel is incremented. Those channels as well as the complete coincidence logic are listed in table 1. At the end of a measurement cycle these counter readings are compressed and transmitted. So because of the counters, the total number of particles hitting the detector is accounted for, while the PHA data is available only for a statistical sample.

For PHA data only particles not hitting the anti-coincidence are registered. Corresponding counters are stored as well as counters for every single detector independent of other detector hits, called single counters.

2.2.1 *Telemetry and data groups*

The data rate of the telemetry system of the spacecraft varies greatly in dependence of the position relative to earth; there are time periods

channel name	nominal particles	coincidence	nominal energy per nuc	sectorized
P1	p^+	$\underline{1}\overline{2}$	1.3 - 3.8	yes
P4	p^+	$\underline{\underline{12}}\overline{3}$	3.8 - 12.8	yes
P13	p^+	$1\underline{\underline{23}}\overline{4}$	12.8 - 26.8	yes
P27	p^+	$12\underline{\underline{34}}\overline{5}$	26.8 - 36.6	yes
P37	p^+	$23\underline{\underline{45}}\overline{C}$	36.6 - 50.7	no
P51	p^+	$34\underline{\underline{5C}}$	> 50.7	yes
A2	He to Mg	$\underline{1}\overline{2}$	1.7 - 3.7	yes
A4	He to Mg	$\underline{12}\overline{3}$	3.7 - 12.7	yes
A12	He to Mg	$1\underline{23}\overline{4}$	12.7 - 26.6	yes
A27	He to Mg	$12\underline{34}\overline{5}$	26.6 - 36.5	no
A37	He to Mg	$12\underline{345}\overline{C}$	36.5 - 48.1	no
A48	He to Fe	$34\underline{5C}$	> 48.1	no
E0.3	e^-	$\overline{1}\underline{\underline{2}}\overline{3}$	0.3 - 0.8	yes
E0.8	e^-	$\overline{1}\underline{23}\overline{4}$	0.8 - 2.0	yes
E2	e^-	$\overline{1}2\underline{\underline{34}}\overline{5}$	2.0 - 3.0	no
E3	e^-	$\overline{1}2\underline{\underline{345}}\overline{C}$	3.0 - 4.0	no

Table 1: coincidence logic for the E6. $\overline{\text{N}}$ means no threshold of detector N was exceeded. N means the lower or the upper threshold of detector N was exceeded. $\underline{\underline{\text{N}}}$ means only the lower threshold of detector N was exceeded. $\underline{\text{NM}}$ means the lower thresholds of detectors N and M were exceeded as well as the upper threshold of N **or** M.

with no connection at all. While connected, the rate of the spacecraft fell between 8 and 4096 bit/sec.

The E6 data sets consists of 1872 bits. One revolution of the spacecraft is divided into 8 sectors by the E6. The counter readings and PHA data are divided into those sectors. Exceptions are the channels P37, E2, E3, A27, A37 and A48 in table 1. Only omnidirectional counters were transmitted from these channels.

Every data set is divided into three groups. Every group consists of data from a different set of channels. The data from one group contains housekeeping data, the information of the last sector, duration of the data acquisition, 32 single and coincidence counter readings and 6 to 16 PHA words, depending on the length of the counters.

All counter readings in one group are only from the channels that are covered by this group. This means for example that counters from channel P13 and P4 are never transmitted in the same data package, as they are in different groups.

The first 6 PHA words will be overwritten in priority mode, which will be triggered when all 16 words are used. The priority mode en-

sures that for selected channels at least one PHA word is saved. This doesn't change the distribution of PHA words inside one channel, but rather implicates some channels will gather more PHA data than other channels.

One PHA word consist of

- coincidence type (see table 1)
- the logarithmic pulse height in the last three detectors including the sapphire, whose thresholds were exceeded
- sector
- priority mode bit (0: normal, 1: priority mode)
- parity bit

While one full measurement is theoretically formed by the data from all three groups, the exact time covered for each group might differ by small amounts.

Depending on the data rate the spacecraft transmitted a complete data set every 13.5 to 2592 seconds, resulting in a higher time resolution during better telemetry. To take into account this effect and foreseeable loss of communication, the measured data could be buffered slower in the internal 55 kbit memory. For a long loss of communication even only every n-th dataset can be saved to make the data more continuous in time.

3

PRE-FLIGHT CALIBRATION OF THE EXPERIMENT E6

All data used in the following analysis of this thesis were recalibrated. The prior existing calibration data and the techniques for recalibration are explained in this chapter.

The E6 had been calibrated before the mission launch. However, the calibration data poses several problems.

3.1 SAPPHIRE-DETECTOR

This section concentrates on the dependence of the photon number from the incident particles speed and direction. These investigations were done by Reinhard [1970]. Since the number of photons and thus the signal is not proportional to the deposited energy, the calibration is way more complicated.

A cosmic muon, for example, produces the same cone of Cerenkov-Radiation entering the detector forwards and backwards, but the majority of the photons produced by the backwards muon are absorbed by the epoxy, resulting in a totally different number of photons reaching the PMT below the detector. The number of scintillation photons from the muon is nearly independent from its direction.

For quantification of the absorption as well as the ratio between scintillated and Cerenkov photons for a given charge z and velocity ν several calibration measurements with muons and α-particles had been taken with the sapphire before the instrument was built. The results for backwards and forwards muons are shown in Figure 9.

A measurement with 5.48 MeV α-particles resulted in the spectrum shown in Figure 10. Since α-particles with this low energy only produce scintillation light, the measurement is independent of direction of the particles.

The amount of scintillated photons from the α-particles roughly corresponds to the amount of photons from the backwards muons. The number of photons produced by a forward muon exceeds this by a factor of roughly 7.

From those measurements the ratio of scintillated photons to Cerenkov photons S/C was concluded to be 0.154[Reinhard, 1970] for a cosmic muon. This leads to the curves shown in Figure 11. The absorption of photons by the epoxy was determined to be 0.976[Reinhard, 1970].

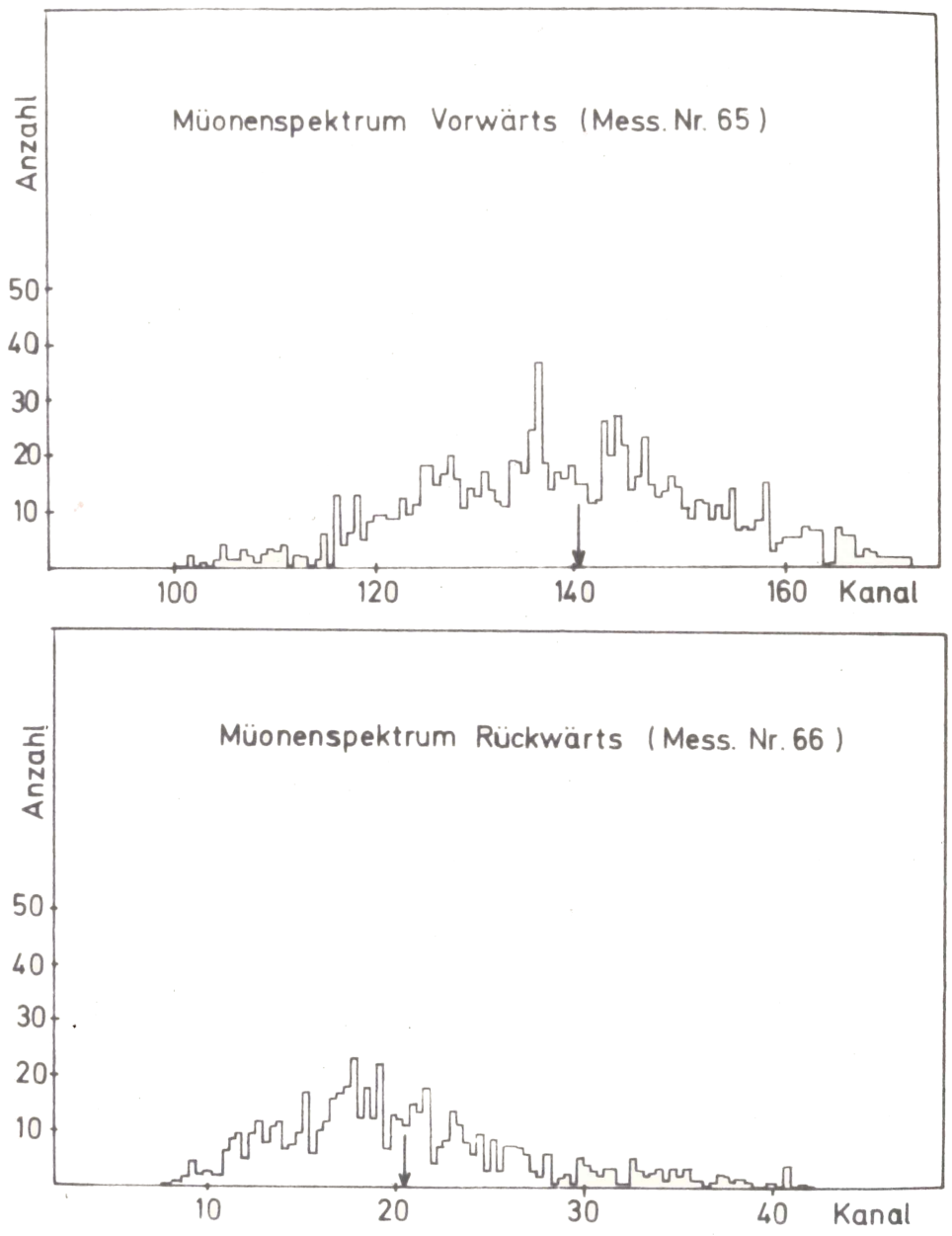

Figure 9: highly relativistic muon spectra measured in detector C from [Reinhard, 1970]. Forwards in the top panel and backwards in the bottom panel. The photon numbers are Cerenkov-light dominated, thus the massive difference in the spectra

3.2 PRE-FLIGHT TEMPERATURE CALIBRATION DATA

The electronic components of most instruments change their behaviour depending on their temperature. When an instrument is calibrated, these effects are determined and corrected for. This has been done for the E6 by Fuckner [1974] and Iwers [1976]. Their results form the basis of the following analysis.

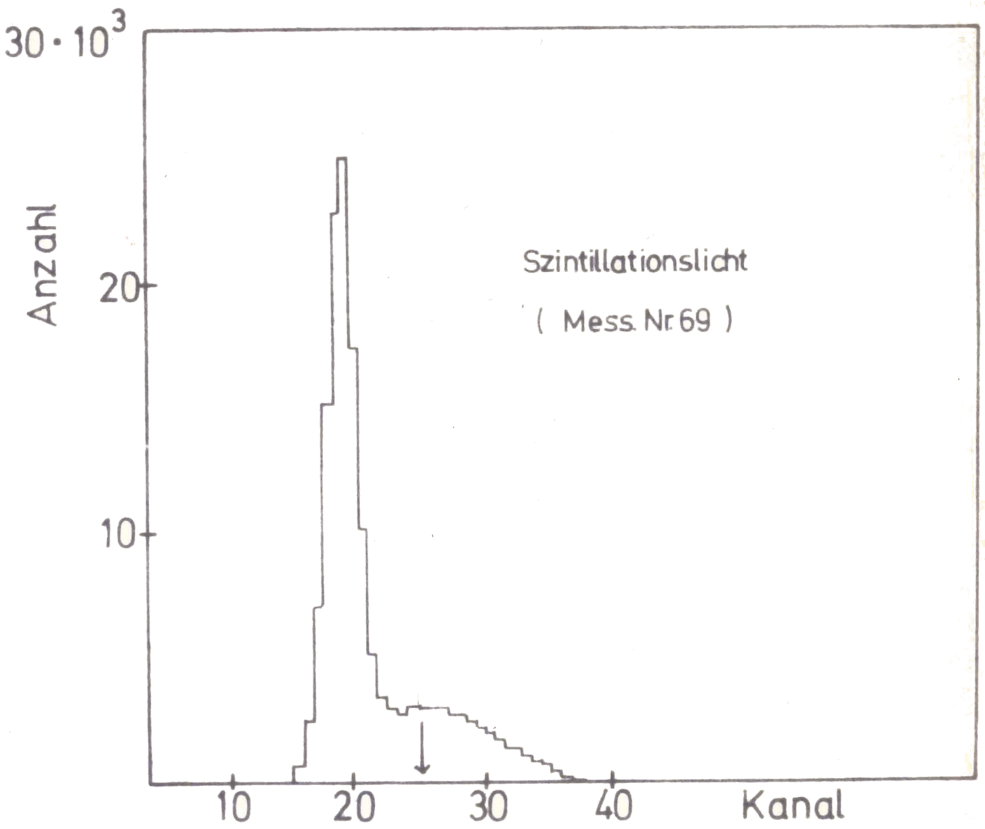

Figure 10: measured 5.48 MeV α-particle spectra in detector C from [Reinhard, 1970]

An example of this calibration for detector 5 and several temperatures can be seen in Figure 12. The upper panel shows the logarithm of the upper energy bin edge for channels between 50 and 70 for five different temperatures. Since there are no gaps in energy coverage, the lower bin edge of a channel corresponds to the upper bin edge of the previous channel. The middle panel shows the energy coverage of the channels 56-58 in dependence of the temperature. The lower panel shows the relative response of every channel between 45 and 65 to particles depositing between 0.5 and 0.7 MeV.

In this figure, one can notice several features:

- The temperature dependence is not monotone (and therefore also not linear): In the upper panel the 17°C line is below the 31°C line. The temperature dependence in the middle panel has the form of a parabola instead of a straight line.
- The logarithmic bin width are not constant: The bars in the middle panel have different sizes depending on channel and temperature
- The relative responses vary greatly depending on the temperature: In the lower panel the response of channel 53 at 6°C is

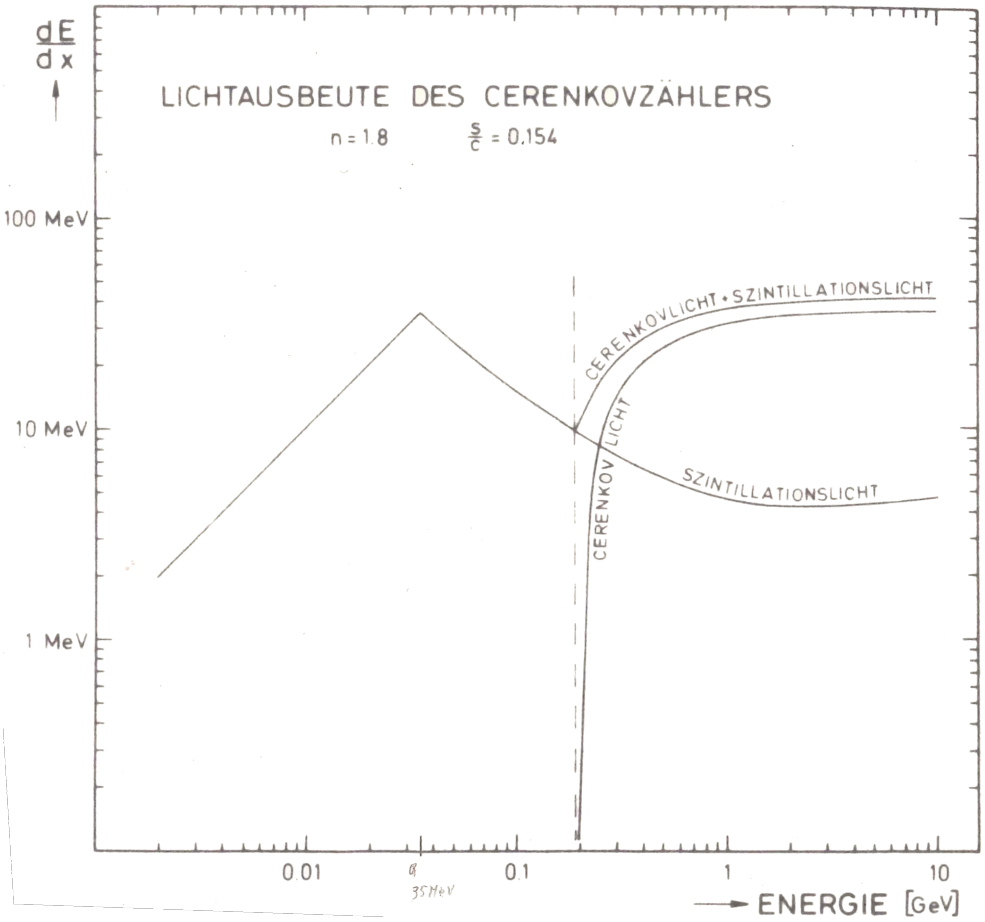

Figure 11: light yield from scintillation and Cerenkov-radiation in dependence of energy for detector C [Reinhard, 1970]

nearly zero while the response of channel 57 is twice as high at 6°C than at 17°C

These features should be present in the in-flight data as well, so two easily recognizable patterns per detector have been chosen to check this: For detectors 4 and 5 this is the peak of minimal ionizing particles. Since only the PHA data of the last three detectors will be saved and those are always 4,5 and C for a MIP, for the first 3 detectors the puncture point is used, which will be defined as the maximum energy deposit before the particles penetrates the detector from now on.

In Figure 13 these patterns used for the following analysis are illustrated based on the in-flight data: The upper panel shows a 2D histogram of the channel in detector 5 versus the channel in detector C. The minimal ionizing patterns of H and He haven been marked by boxes. The lower panel shows a 2D histogram of the channel in detector 1 versus the channel in detector 2. Here, the puncture points of H and He have been marked by boxes.

Now, the the counts inside the boxes are integrated over the channel number in detector C for every temperature, resulting in a distinct count distribution in detector 5 depending on temperature. These patterns have all been normalized to their maximum for each temperature and are shown versus temperature in the upper panel of Figure 14. The same has been done by integrating the boxes in the lower panel of Figure 13 over the channel of detector 1 and norming, resulting in the lower panel in Figure 14.

So, in Figure 14 the in-flight histogram of the flux of minimal ionizing He in detector 5 as well as the puncture point of detector 2 depending of the temperature of the detector is shown. The temperature dependence is shown by the position of the contour lines from the histogram: The contour lines change with temperature, but the slope is monotone and nearly linear. The distance of the contour lines to one another is nearly constant, implicating a constant logarithmic bin width of the energy coverage of the channels. Also there is no sign of varying relative responses: The pattern shifts as a hole depending on temperature but does not change apart from that. The existing bumps of the contour line do not appear to be depending on temperature since they don't go through the whole pattern but rather result from the low statistics for some temperatures.

From this it is concluded that the old calibration data is faulty and a new calibration, based on the in-flight data, is necessary.

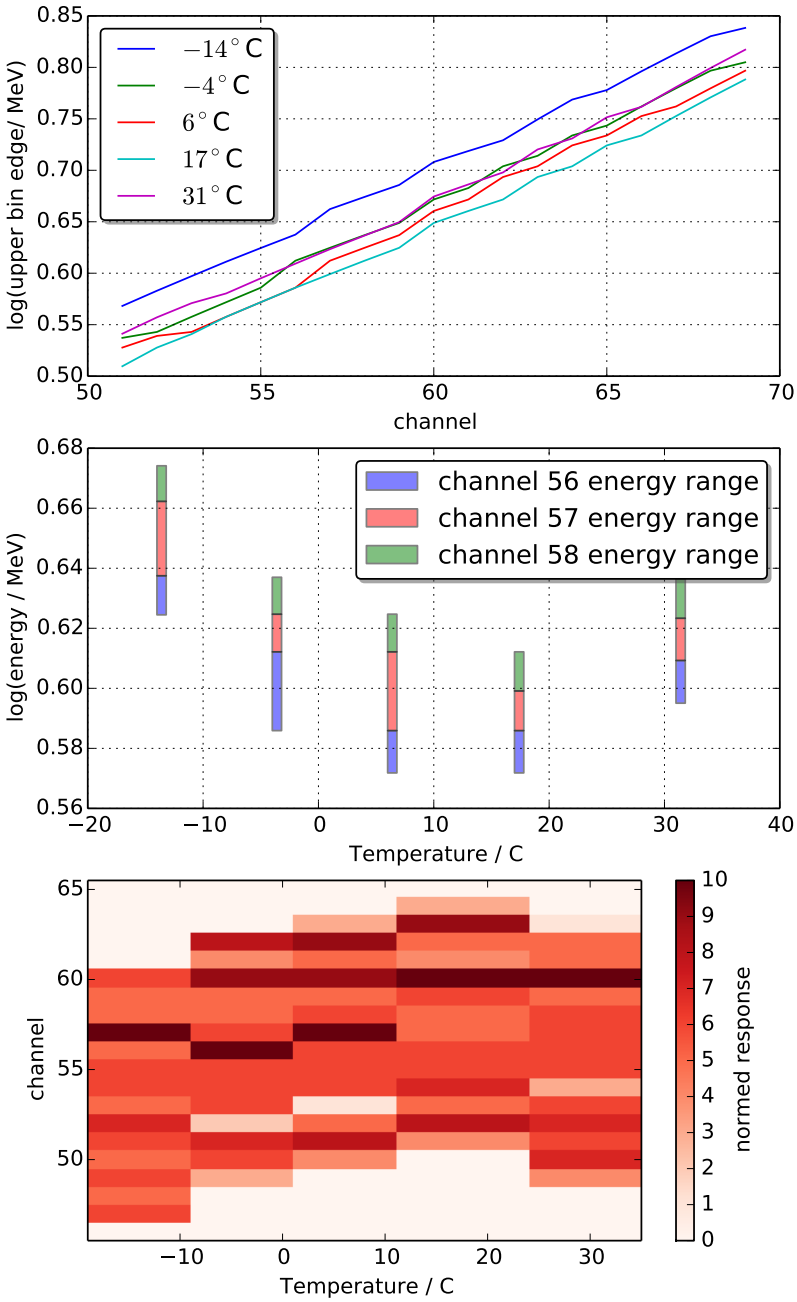

Figure 12: upper panel: calibration lines for detector 5 and several temperatures. middle panel: energy bins for three selected channels in dependence of the temperature. The bin widths are not constant and the dependence from temperature of the bins position is not monotone. Lower panel: Resulting relative responses of particles depositing between 0.5 to 0.7 MeV. As a result of the aforementioned effects, the responses for the channels vary strongly depending on temperature.

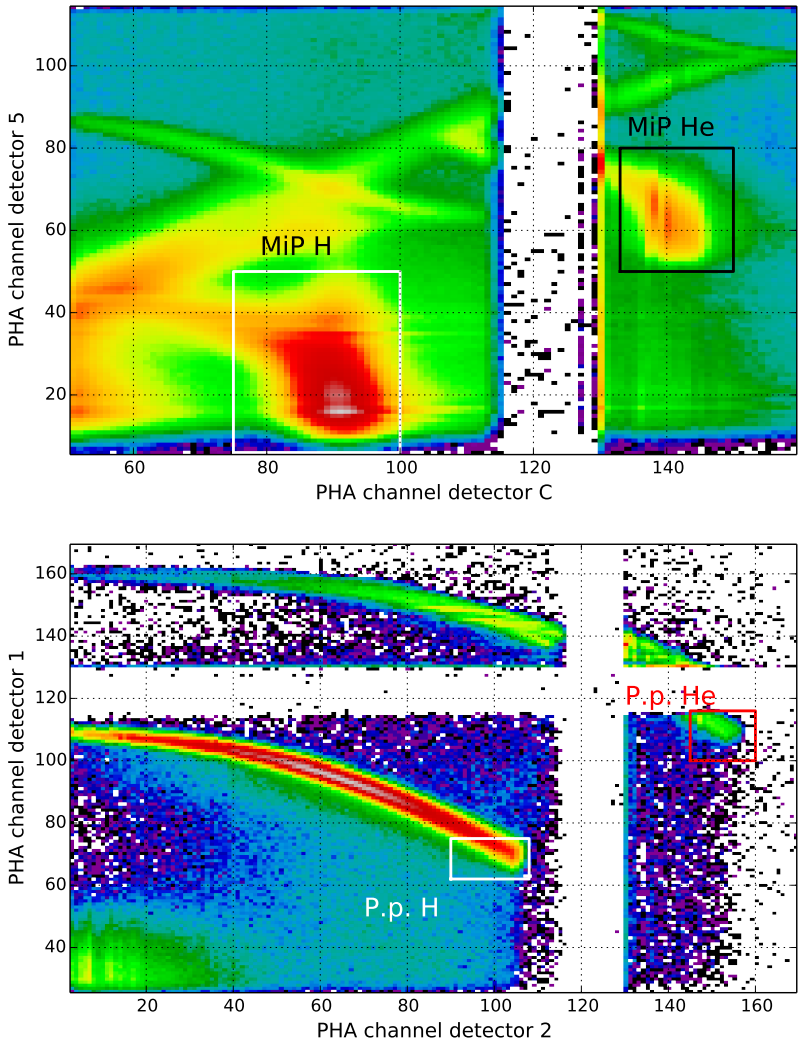

Figure 13: illustration of the minimal ionizing particle pattern in detector 5 and C on the upper panel and of the puncture points in detector 2 and 1 in the lower panel. For more details see text.

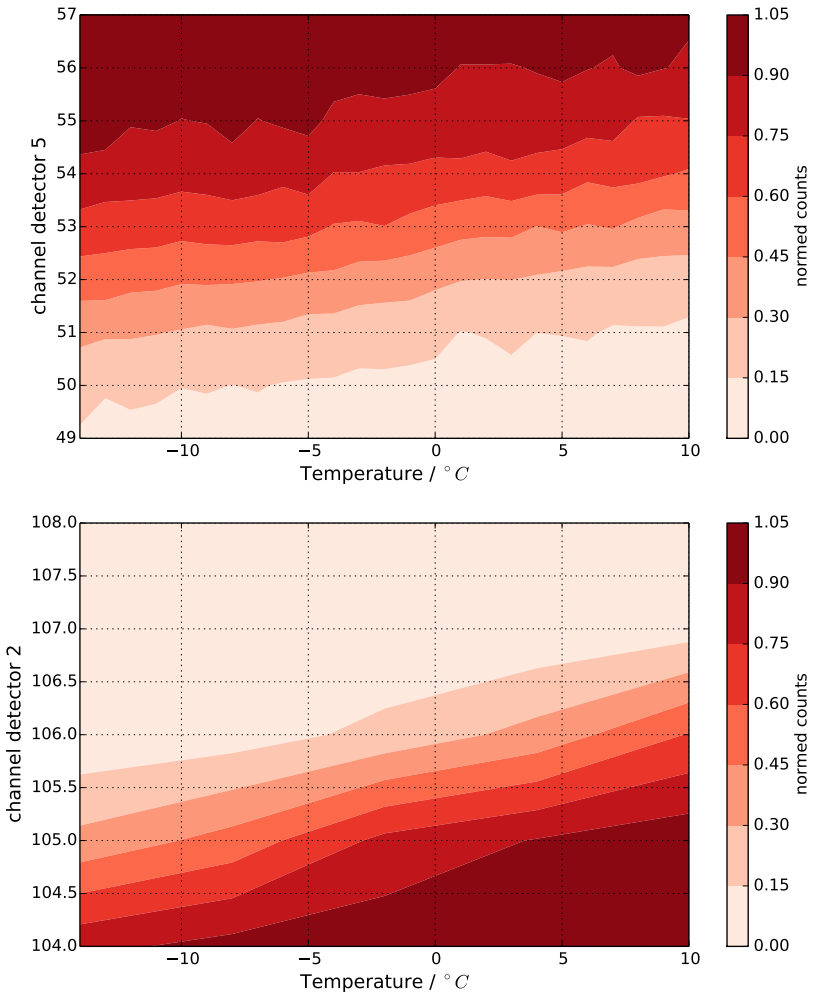

Figure 14: upper panel: 2D histogram of the minimal ionizing He peak in detector 5, normalized to maximum for each temperature bin. Lower panel: 2D histogram of the H puncture point in detector 2, normalized to maximum for each temperature bin.

4

SIMULATION SETUP AND RECALIBRATION

As mentioned in the previous chapter, the comparison of in-flight data with pre-flight calibration data poses some inconsistencies. In this chapter, a new calibration based on simulations of the instruments and some of the pre-flight calibration data is attempted.

The simulation of the E6 was conducted with the Monte-Carlo based GEometry And Tracking (GEANT) 4 toolkit [Agostinelli, 2003]. This simulation toolkit allows to simulate the interaction of different test particles with a given detector setup.

The simulated geometry of the E6 is visualized in Figure15.

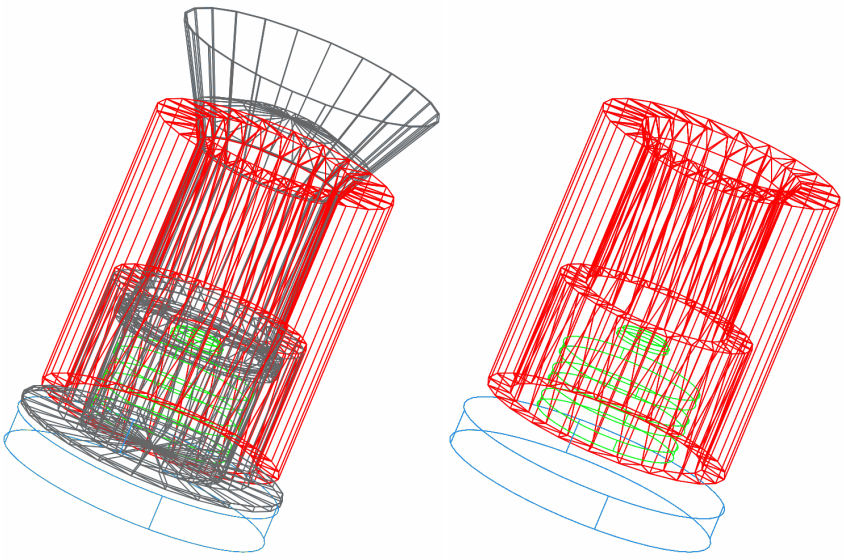

Figure 15: visualization of the instrument geometry as used in the simulation. While the right side displays the active detectors only, the left side also shows passive material like mounting structure. In green the semiconductor detectors, in red the anti-coincidence and in blue the C-detector

For the simulation conducted in this work the energy deposited was simulated and the responsiveness of the detector system for different particles has been determined. Especially the amount of photons produced in the sapphire from particles for different charges z and velocities v was analysed by using the optical tracking toolkit of GEANT 4. The propagation of the photons was tracked as well, until they either leave the detector setup completely, are absorbed or hit the photo-cathode of the PMT, so an accurate reconstruction of all occurring optical processes is discussed in the following section.

4.1 REPRODUCING THE PHOTON EMITTANCE FROM THE PRE-FLIGHT CALIBRATION

Using the ratio of scintillation photons to Cerenkov photons 0.154 for a cosmic muon and absorption chance for photons by the epoxy of 0.976 from [Reinhard, 1970] for the simulation, the simulated muons and alpha particles result in the spectra shown in Figure 16. This reproduces the old calibration measurements in Figures 9 and 10: Backwards muon and α particle roughly correspond to each other while the forwards muon exceeds those photon numbers by a factor of 7.

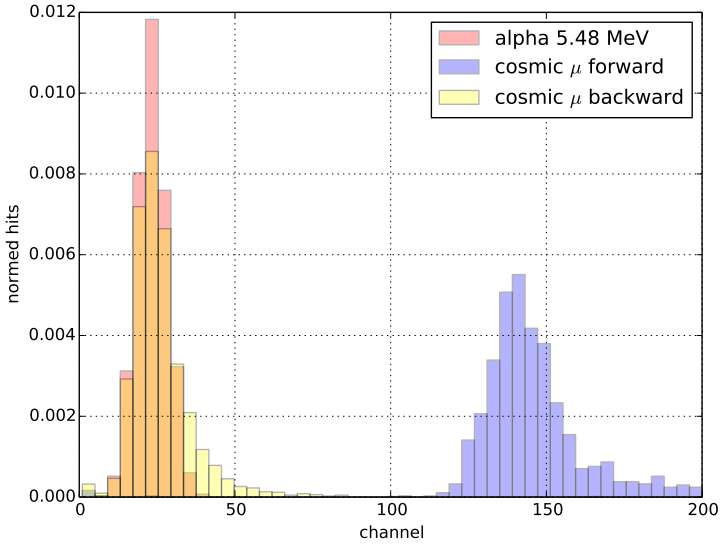

Figure 16: simulated photon numbers from forwards and backwards cosmic muons and from α-particles with 5.48 MeV in detector C

Figure 17 shows the comparison of simulated and inflight protons in the detectors 5 or 4 versus C. Plotted is the 2D-histogram of the relative counts in the minimum of the channel in detector 4 or 5 versus the channel in detector C. The left panel only shows simulated forward protons. The contour lines come from an Gaussian interpolation of the histogram, while the points are a sample of the distribution that clearly shows the broadening of the distribution with higher energies of the particles. The minimum of detector 4 and 5 was chosen as this results in a more narrow distribution for higher energies. The colour indicates the primary energy of the protons, binned logarithmically equidistant with the exception of the last bin which is much wider and serves as an integral bin. The simulated spectrum corresponds to the expected GCR spectrum.

In the middle panel the forward protons from the left panel are shown as filled contours, while backwards protons are shown as solid contour lines and backwards helium as dashed contour lines with

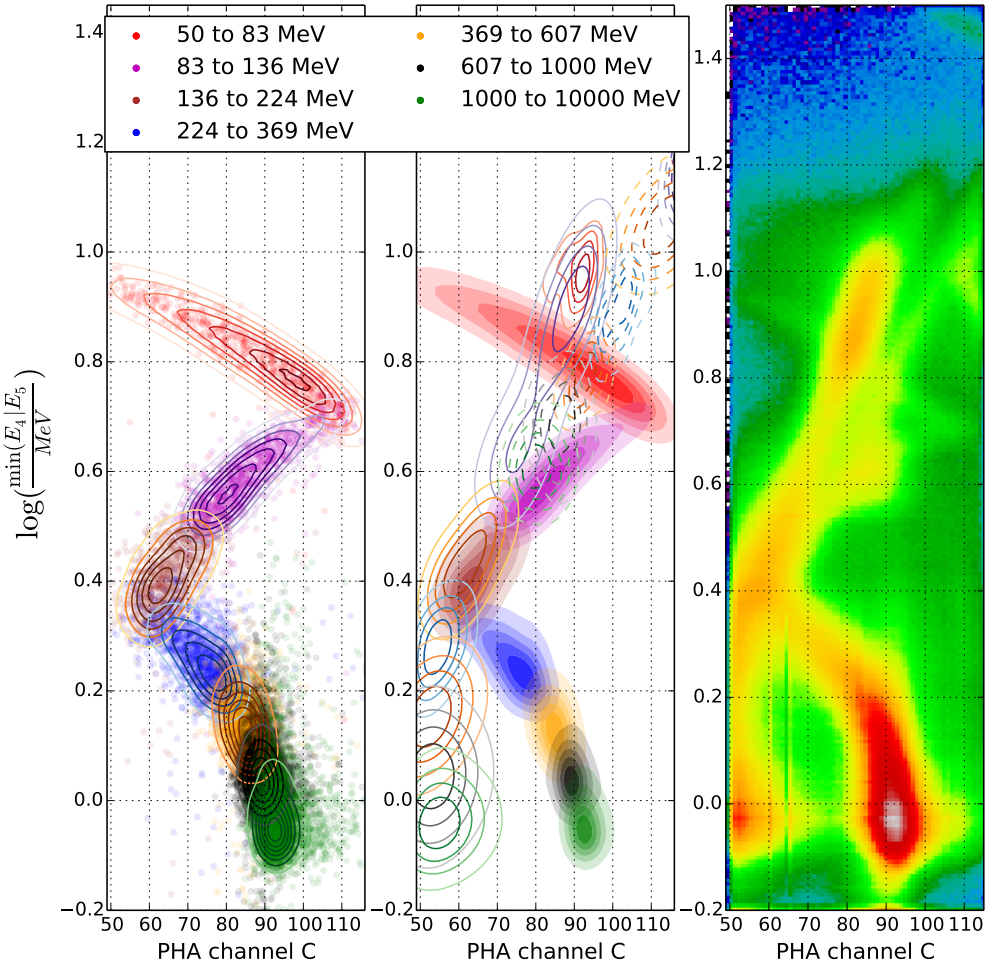

Figure 17: Comparison of a simulated proton spectra with a measured spectrum, colour-coded the simulation energy. On the left panel only forward protons, on the middle panel additional backwards protons in solid lines and backwards helium in dashed lines. On the right panel in-flight data from the first 3 years of HELIOS A [Marquardt and Heber, 2019]. For more details see text.

the same colour coding. It shows clearly the overlapping of the backwards particles distributions with the forwards protons.

The right panel shows the 2D-histogram of the inflight data. In this panel the colour coding indicated the relative count number. All simulated patterns are visible and are at the expected channel numbers. Thus, the simulation of protons and helium yields good agreement with the inflight data and allows the determination of the response and energy for given PHA data using the simulation.

Figure 18 shows a comparison of simulated protons, helium, carbon, nitrogen and oxygen with measurements. These elements have been chosen as they are the most abundant in the GCR and can thus be analysed with comparatively good statistics. In the upper panel the simulated 2D-histogram of energy deposit in detector 5 versus

channel in detector C is shown. The black line marks the MIP part of the spectra.

The lowest panel shows the same for inflight data, with the line from the upper panel. Two discrepancies between simulated and inflight data are obvious for elements heavier than helium:

- the whole pattern is shifted to the left in the measured data
- the difference between maximum scintillation light and maximum Cerenkov-light for a given element is to small in the simulation; the particles emit to much scintillation light

The first effect can be explained by saturation of the PMT, the second effect can be explained by quenching, see 1.1.1. So both effects have been taken into account and lead to the complete simulation in the middle panel of Figure 18.

4.2 IN-FLIGHT TEMPERATURE CALIBRATION

For the new calibration a approach in two steps is chosen: First, the detectors temperature dependence needs first to be taken into account.

As the dependence from temperature is nearly linear as seen in Figure 14, a line is fitted to the pattern and the temperature dependences are corrected this way. A similar approach had been chosen by Bialk [1996], who fitted the puncture point of energy spectra at several temperatures.

Secondly, the energy calibration lines are redone: The energy for the puncture points or MIP peak illustrated in Figure 13 is known from the simulation, so since H and He have sufficient statistics to determine those points in the data, there are two points per detector with known energy for recalibration. Together with the Analog-to-digital converter (ADC) characteristics measured by Fuckner [1974], this is sufficient for recalibration: For a logarithmic amplifier, the slope of the ADC characteristic line is the same as for the energy calibration line.

In Figure 19 the temperature corrected measured and the simulated normalized histograms for minimal ionizing H and He in detector 5 are shown. The simulation has only been conducted up to 5 times the resting energy for every species with a GCR spectrum. The increase of the flux with higher energy for He might be a result of very high energy particles, which have a higher energy deposit according to Bethes formula, or a result from electronic noise prevalent close to the second detector threshold. So for the calibration the left flanks of the peaks have been chosen.

In Figure 20 the temperature corrected measured and the simulated normalized histograms for the puncture points of H and He are shown in detector 2. The increase of the flux with lower energies

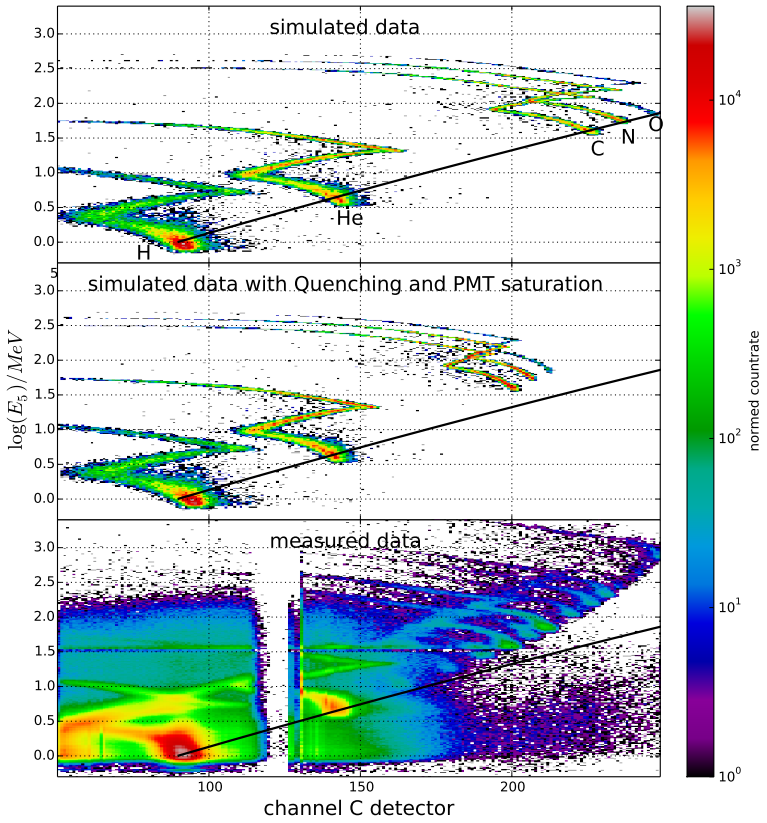

Figure 18: the top panel shows the logarithm of the deposited energy in detector 5 versus the channel in detector C of simulated protons, helium, carbon, nitrogen and oxygen without taking PMT saturation and Quenching into account. The middle panel shows the same simulations,taking PMT saturation and Quenching into account. The bottom panel shows measured date for comparison. The black line represents the expected power law from theory. The simulated spectra and element ratios don't match the measured ones, but rather only illustrate the patterns.

results from a deviation from the expected GCR spectrum caused by particles accelerated in the heliosphere or at the Sun. The measured He peak at roughly 1.5 results from second detector threshold at this energy. For both elements the right edges of the spectra have been used.

The slope of the new calibration lines from in-flight data is roughly consistent with the averaged slope of the pre-flight calibration, as shown in Figure 21. Furthermore, the calibration lines of the detectors 3,4 and 5 are practically identical, which implies their construction quality is better than previously assumed.

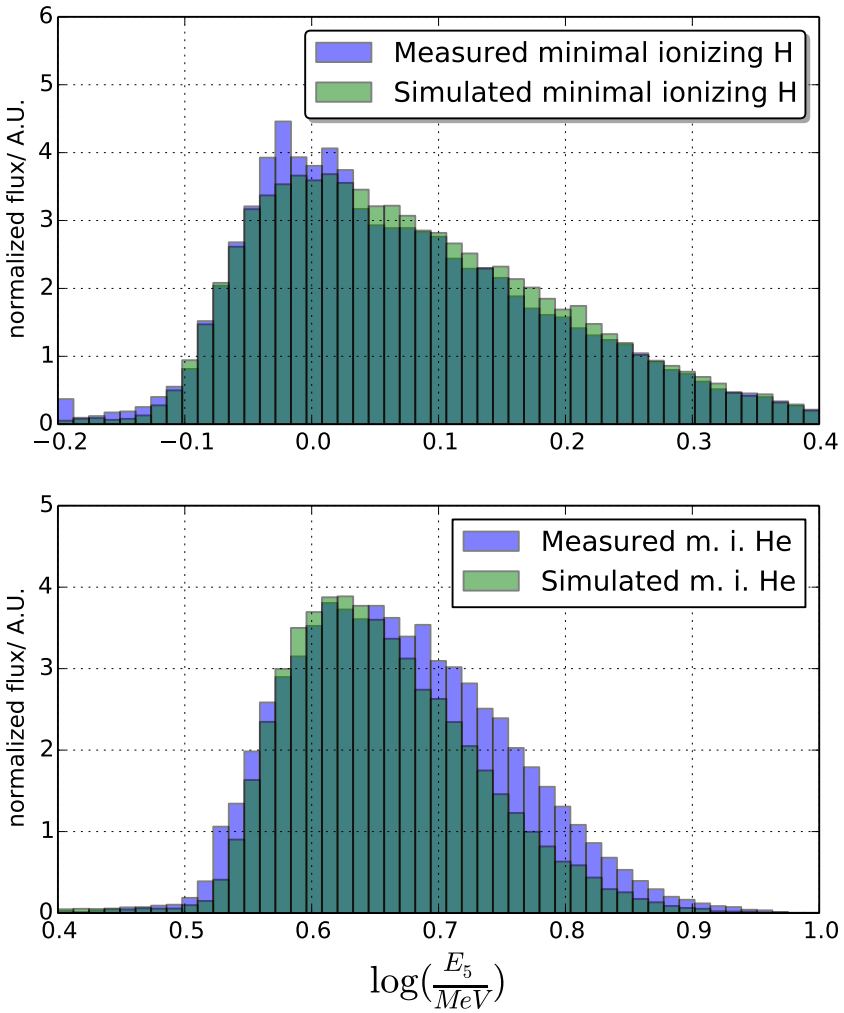

Figure 19: histogram of the minimal ionizing H and He peak in detector 5, simulated and measured

4.2.1 *Calibration of detector C*

The aforementioned method can not be applied to detector C, as is shown in Figure 22. In this figure the photon number of highly relativistic protons, as shown in Figure 13, is analysed.

The upper panel shows the dependency of the channel from the temperature. While it looks nearly constant at first, it is neither monotone nor linear. The reason for this can be found by closer examination of the temporal dependence: In the middle panel the temperature of the spacecraft sensors versus time is shown, while in the lower panel the channels versus time are shown.

While there is clearly a trend depending on the temperature, the pattern shows some kind of hysteresis as well as general degrada-

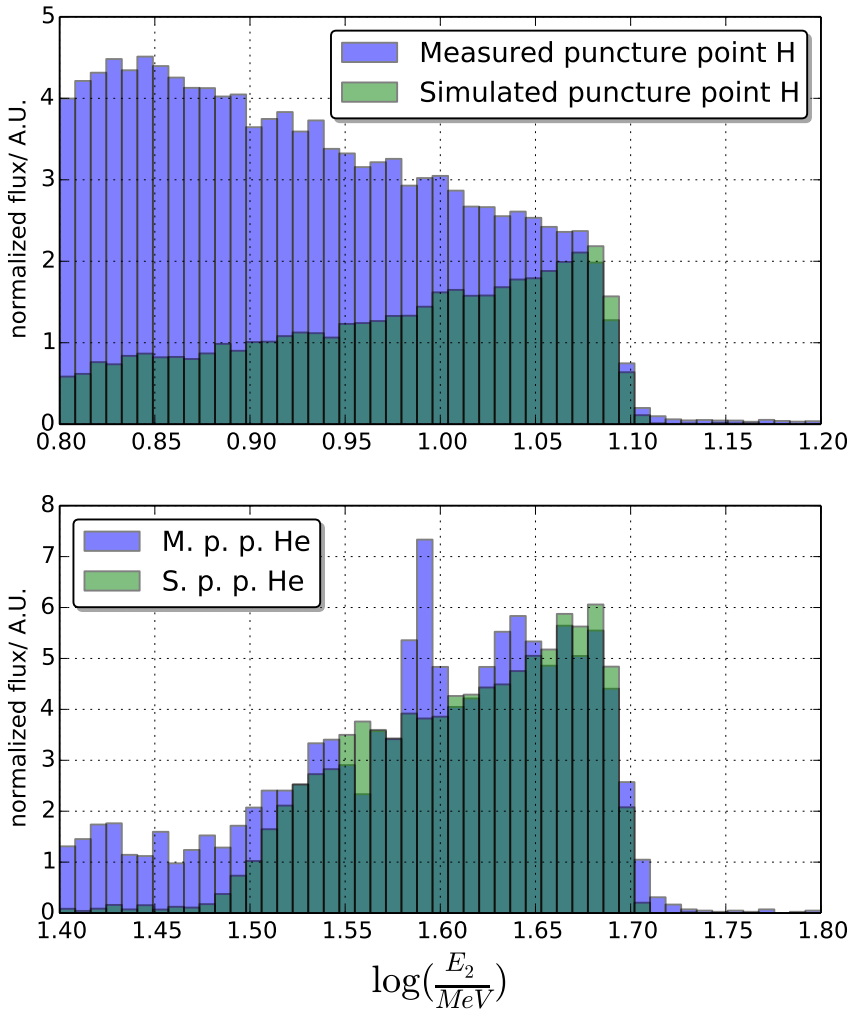

Figure 20: histogram of the puncture points of H and He in detector 2, simulated and measured

tion. The closest point to Sun is marked by a blue line for a randomly selected revolution. A black line marks 20 days before the blue line. While the temperature behaves as expected in this 20 days, the position of the peak doesn't:

At the blue line, the position is closest to Sun, the temperature is at a local maximum as well as the channel of the particle peak.

At the black line, however, the particle peak shows a local minimum, which would neither be expected from the temperature nor the distance to Sun.

Thus the temperature correction can not be done by the temperature, but has to be done by the elapsed time.

This pattern is exclusive to signals caused by the Cerenkov-effect, as Figure 23 shows. In the figure the histogram of the signals in the

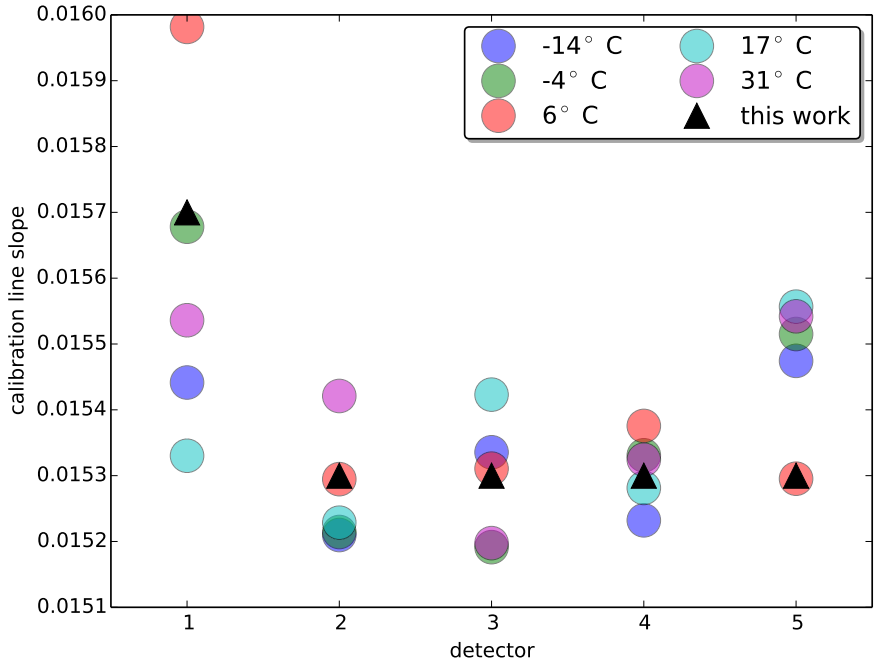

Figure 21: energy calibration line slopes for every detector from pre-flight calibration and from this work

p51 is shown for two periods of time lying 20 days apart, marked by the blue and black lines in Figure 22. While there is a clear shift in the lower part of the histogram, there is no shift in the upper part. This implicates the effect can't be caused by the electronic processing.

Since the signal in the lower part is produced by the Cerenkov-effect while the upper part in caused by scintillation and the corresponding photons have different energies, only two possible explanations remain: the optical properties of the sapphire or the wavelength dependency of the PMT drastically change in those 20 days.

As this thesis is written, it is unclear, which of this effects applies and what the physical reasons for this possible effect are.

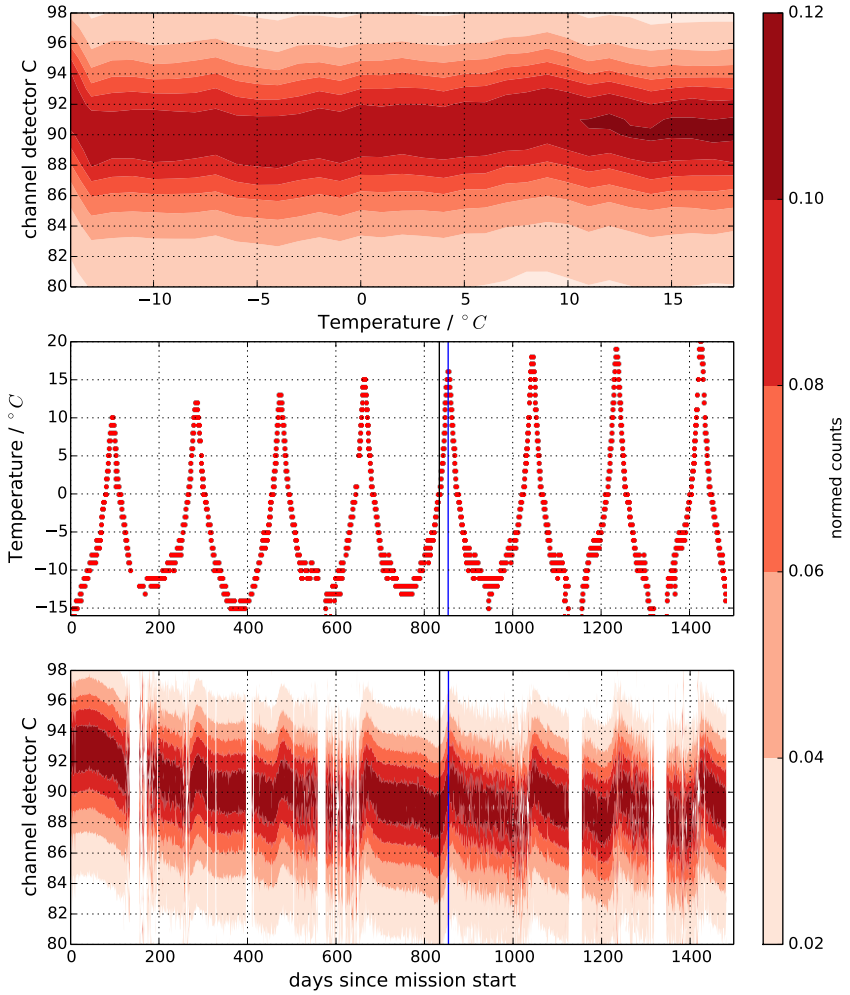

Figure 22: upper panel: 2D-histogram of the near light-speed H peak in detector C versus the temperature, normalized to the sum for each temperature bin. Middle panel: Temperature versus elapsed mission days. Lower panel: 2D-histogram of the near light-speed H peak in detector C versus elapsed mission days, normalized to the sum for each day. The blue line marks the closest point to Sun for a randomly selected revolution. A black line marks 20 days before the blue line. White lines are because of data gaps.

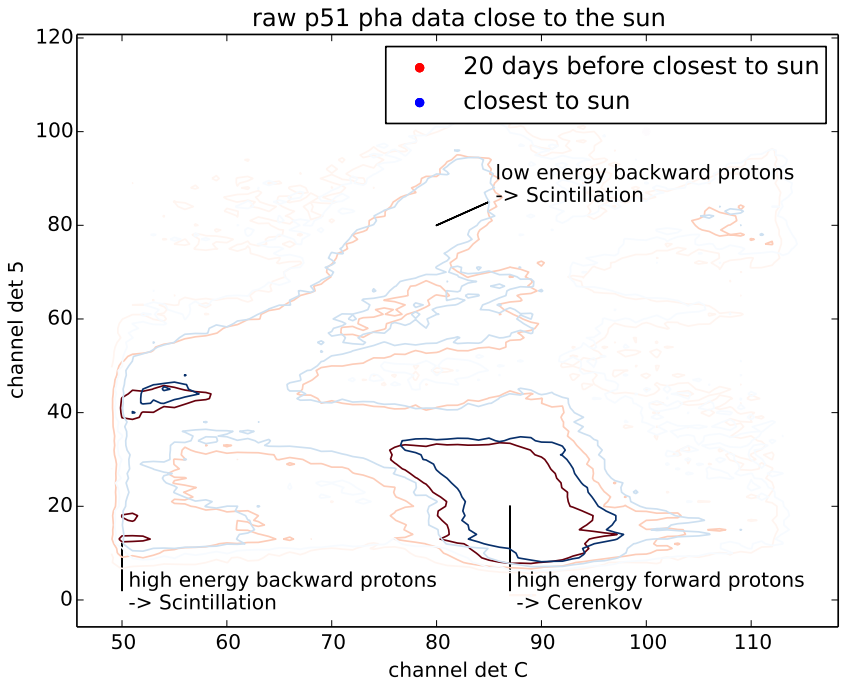

Figure 23: Gaussian interpolated contour lines of the uncorrected, uncalibrated p51 data histogram. The lower part of the histogram shows a clear shift of about two channels, while the upper part doesn't show this shift.

5

GALACTIC COSMIC RAY ORIGIN AND ABUNDANCES

Most particles measured with energies between 30 and 10^{12} MeV/nuc measured at Earth originate from within our galaxy but outside the solar system. This GCR particles are assumed to be accelerated by shock fronts of super-nova remnants, cosmic jets from black holes and pulsars; they can be divided into primary and secondary elements: those elements which are produced in large abundances in the sources are called primary elements, while those produced by spallation in the interstellar gas are called secondary elements.

Thus, from primary elements we can learn about the acceleration and interstellar modulation while from secondary elements we can learn about travel time and the difference in path length for spallation processes. The unmodulated primary element spectra show the typical power law spectra with exponents between 2.5 and 2.7 originating from shock acceleration. The spectra of the secondary elements on the other hand can vary greatly.

Shown in Figure 24 are the relative abundances to Si from He to Ni in the solar system and in GCRs. It is evident that elements like Li, Be and B are orders of magnitude more abundant in GCRs than in the solar system. Those elements are good examples for secondary GCR elements: Primary GCRs hit interstellar atoms with which they interact spallation processes resulting in the secondary GCRs.

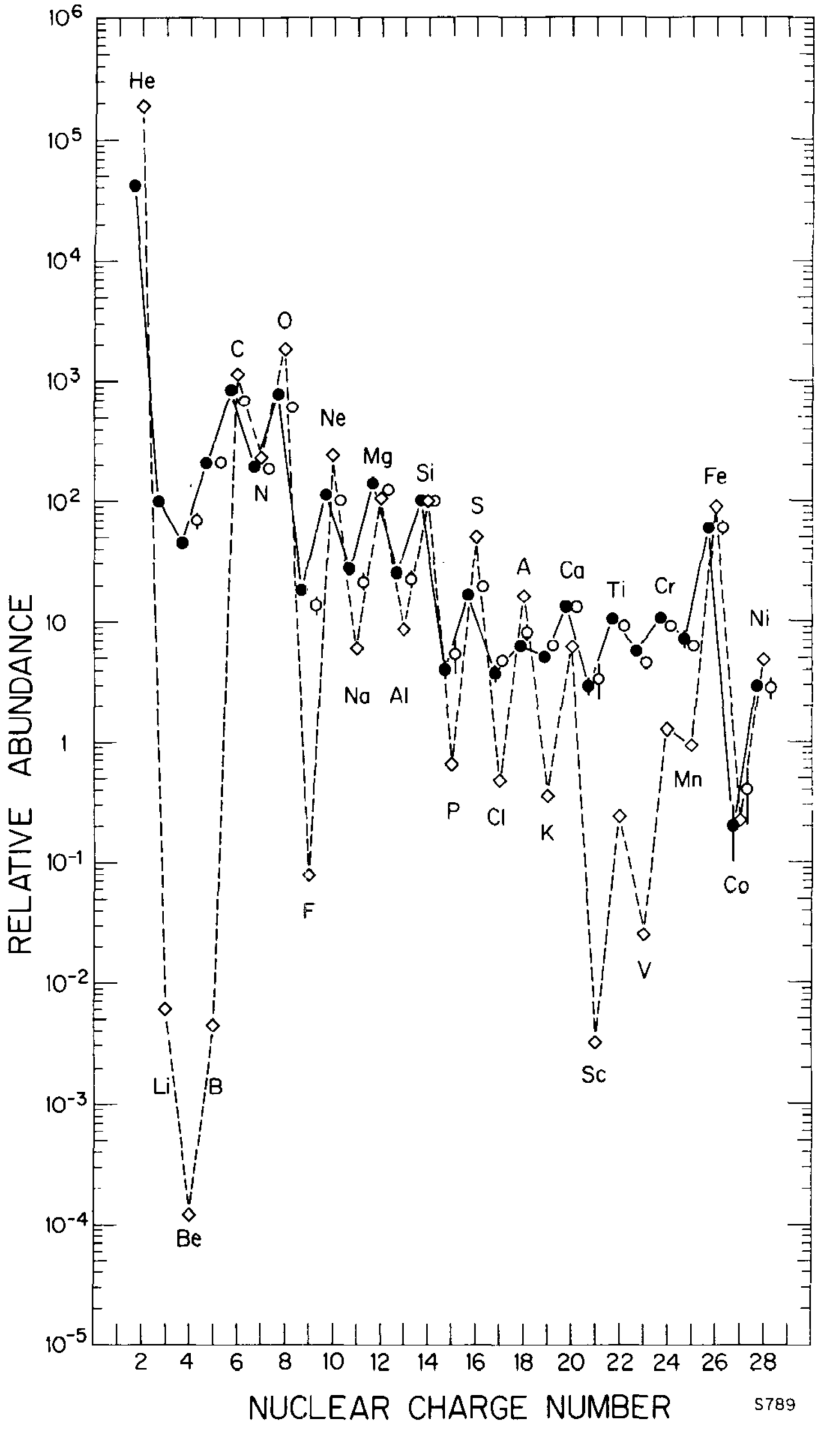

Figure 24: the cosmic ray element abundances (He-Ni) measured at Earth compared to the solar system abundances, all relative to silicon. solid circles: 70-280 MeV/nuc open circles: compilation of high energy measurements, 1000-2000 MeV/nuc diamonds: solar system [Simpson, 1983]

5.1 PUBLICATION 1: GEANT 4 SIMULATION OF THE HELIOS COSMIC RAY TELESCOPE E6: FEASIBILITY OF CHEMICAL COMPOSITION STUDIES

In order to study the composition of the GCRs, one needs an appropriate instrument. Since elements heavier than helium are much less abundant and the E6 is as comparably small instrument, some basic calculations have been conducted to study the total number of counted particles heavier than hydrogen and compare those numbers to literature as well as to determine a sensible binning for energy histograms.

A different effect results from the silicon detectors being glued into their holdings without a guard ring. At the edges of a silicon detector, as the one being described in chapter 2, the electric field inside the detector doesn't drop to zero immediately. Instead the field strength slowly decreases, resulting in a decreasing efficiency of the detector. The resulting effects are discussed in this publication.

In Figure 25 the fluences of several elements integrated over the whole measurement period used in this publication are shown. The results indicate the possibility to obtain energy spectra for at least carbon and oxygen.

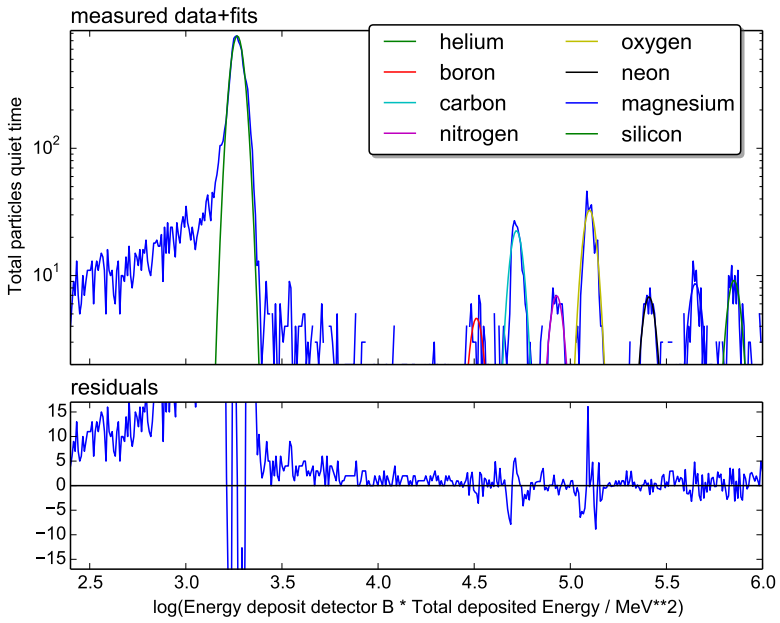

Figure 25: The blue curves show the left projection (1-dimensional representation) of the different measured elements. The other coloured curves are the result of fits by a Gaussian to the data. The bottom panels display the residuals of the fit, indicating the goodness of the fit. Note that the y-axis are on logarithmic and linear scale on the top and bottom, respectively.[Marquardt et al., 2015]

GEANT 4 simulation of the Helios cosmic ray telescope E6: Feasibility of chemical composition studies

Journal of Physics: Conference Series **632** (2015) 012016 doi:10.1088/1742-6596/632/1/012016

GEANT 4 simulation of the Helios cosmic ray telescope E6: Feasibility of chemical composition studies

J Marquardt, B Heber, M Hörlöck, P Kühl, R F Wimmer-Schweingruber
Christian-Albrechts-Universität zu Kiel

Abstract. In October 2011, ESA announced the selection of Solar Orbiter as one of the Cosmic Vision M missions. It's launch is foreseen in 2018. Therefore it is worthwhile to revisit the energetic particle measurements together with the solar wind and magnetic field data from Helios in light of better theoretical understanding and advanced analysis and modelling techniques developed during the past 20 years. In this contribution we will present a GEANT 4 simulation of the response function of the Helios E6 experiment, that measured electrons in the energy range from a few 100 keV to above 10 MeV, ions from 1 MeV/nucleon to above 50 MeV/nucleon, and its application to the data analysis with respect to the chemical composition of the Galactic Cosmic Rays.

1. Introduction

The elemental composition of the cosmic rays in the heliosphere has been measured a number of times during different phases in the solar cycle [1; 2] and different radial distances from the Sun beyond the Earth orbit[e.g. 3; 4].

One of these measurements was carried out by the Experiment 6 (E6) on Helios. Helios 1 and Helios 2 were launched on December 10, 1974 and January 15, 1976, respectively. The two almost identical space probes were sent into ecliptic orbits around the Sun. The orbital period around the Sun was 190 days for Helios 1 and 185 days for Helios 2. Their perihelia were 0.3095 AU and 0.290 AU, respectively.

The E6 particle telescope relies on the $\frac{dE}{dx} - E$-method [see e.g. 5]. In order to interpret the measured data a detailed understanding of the instrument is needed and can be obtained by modelling the physical processes inside the detector taking into account the instrument geometry as well as environment. [e.g. 6].

The instrument consists of a stack of 5 semiconductor, a sapphire and a plastic scintillation detector (see Fig. 1), which measures the number of particles hitting each detector and their energy losses. A rough particle identification (species, energy and incoming direction) can be obtained by analyzing the count rate data that are obtained in (anti)-coincidence of a set of active detectors [see 7]. For a statistical ensemble not only the (anti-)coincidence conditions but also the energy loss in the last three detectors are known. The channel that is analyzed here in detail counts particles in the energy range from ~13 MeV/nucleon to ~27 MeV/nucleon protons and helium.

In order to determine the chemical composition of cosmic rays, the detailed instrument response for different particle species is calculated utilizing a newly developed model of the E6 instrument. The calculations are based on the program library Geant4 that is a toolkit for the simulation of the passage of particles through matter [8]. The purpose of this contribution is to show that the Helios E6-Experiment is capable of determining the chemical composition of particles that are stopped in the detector sensor up to

Table 1. Relative Elemental Abundances at 160 MeV/Nucleon from ACE/CRIS [2; 9]

Element	Solar Minimum 1997/1998 [2]	Solar Minimum 2009-2010 [9]	Solar Maximum 1998-2001 [2]
	at 160 MeV/nucleon		
B	1803.8 ± 10.4	1725.7 ± 19.4	1986.4 ± 11.3
C	7337.0 ± 18.4	7235.4 ± 45	6780.2 ± 18.4
N	1713.7 ± 8.4	1678.9 ± 12.3	1836.1 ± 9
O	7082.6 ± 16	7137.0 ± 42.7	6520.6 ± 15.6
Ne	998.7 ± 5.6	998.9 ± 8.4	1050 ± 5.8
Mg	1368 ± 6.1	1375.3 ± 10.3	1367.3 ± 6
Si	1000 ± 5	1000 ± 7.8	1000 ± 4.8

silicon. The chemical abundances of some light elements at 1 AU known from literature are summarized in Tab. 1.

2. Instrumentation

The Kiel experiment E6 for studying energetic cosmic rays was built as an universal detector. It was supposed to measure most effects of the cosmic radiation which occur in interplanetary space. The energy range extends from 1.3 MeV/n to > 1000 MeV/n for nuclei and from approximately 0.3 to 8 MeV for electrons. The on-board data processing system evaluates the measured pulses created during the particle transition.

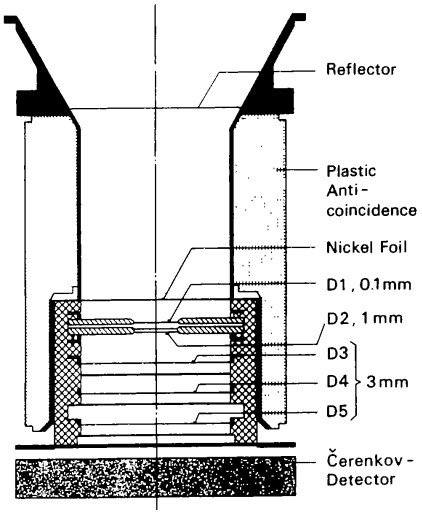

Figure 1. Schematic of the Helios E6

The detector system consists of five semiconductor-detectors of increasing thickness that are shown in Fig. 1. The figure also indicates the thicknesses of the detectors. While detectors D1(A) and D2(B) are silicon-surface-barrier-detectors with a thickness of 100 and 1000 μm, the other three are lithium drifted detectors with a thickness of 3000 μm. The first two (D1 and D2) are used for the determination of the lowest energy channels, for the definition of the geometry factor for stopping particles (energy ranges below 51 MeV/N) as well as for the discrimination between electrons and nuclei. The first detector does not respond to relativistic electrons (above 300 keV), the discrimination between electrons and nuclei is

that the first detector is not triggered for electrons. To avoid false identifications by these discrimination conditions, the first and second detectors have been placed on top of each other, as close as possible. Charged particles, which penetrate the fifth detector and the aluminum absorber beneath, are detected in the Sapphire-Cerenkov-detector. The Cerenkov-threshold for this material (n=1.8) is $E_s = 210$ MeV/nucleon. Because the Sapphire-Cerenkov-detector also delivers scintillation light, particles in the energy range above 51 MeV/nucleon are counted in an integral channel.

3. Data Analysis

In order to determine the chemical and the isotopic abundance together with the energy spectra of each species it is common to design a detector telescope based on a stack of detectors that are surrounded by an anticoincidence detector. The characteristics for stopping particles can then be determined by the $\frac{\Delta E}{\Delta x} - E$-method [e.g., McDonald and Ludwig 5]. The principle of this method shall be explained by means of the left panel of Fig. 2. A charged particle with the energy E_0 penetrates the thin first detector

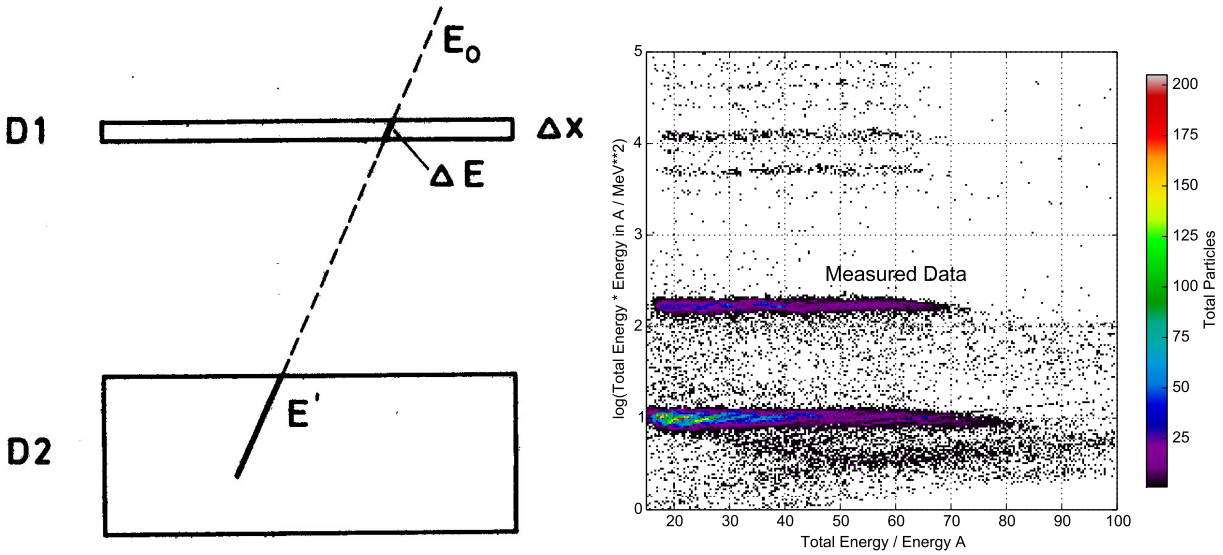

Figure 2. Left: Sample particle trajectory in a dE/dx-E-telescope. Right: $\Delta E \cdot E_0$ versus $E_0/\Delta E$-distribution for (from the bottom to the top) protons, helium, C, N, O, Ne and Si using the energy loss ΔE of the first detector and the sum of the measured energy losses in the first three detectors as E_0. The entries below the curves are caused by the non uniformity of first detector (for details see text).

D1 and stops in the thick detector D2. In the first detector, with a thickness of Δx, the particle loses the energy ΔE by ionization. The residual energy $E^{'}$ is deposited in the second detector. The entire kinetic energy E_0 results from the sum of ΔE and $E^{'}$, the energy losses in both detectors. From the Bethe-Bloch relation [5], the energy loss in both detectors can be determined for a known detector material and for particles of a known species. If $\Delta E = dE/dx \cdot \delta x \ll E^{'}$ and for non-relativistic particles of mass M with $E = \frac{1}{2}Mv^2$ we obtain the following relation:

$$\Delta E \cdot E_0 \propto Z^2 \cdot M = const. \tag{1}$$

This constitutes a typical quantity for a particle-species. Since Z and M can only take discrete values, the relation offers a possibility to separate various particles, i.e., in addition to their energy, to determine their mass and nuclear charge. However, note that ΔE may vary due to the statistical variation of the ionization and because of the different path-lengths, Δx, due to the opening angle of the telescope. Thus in order to separate different isotopes from each other the path-length variations have to be minimized.

The concept of the $\Delta E \cdot E_0$ is best realized for particles that stop in the third detector. The ratio of the thin to thick detector is smaller than 1:10. Due to the limited telemetry, only the energy loss in the last three detectors was transmitted. Thus, for particles stopping deeper in the instrument, the corresponding ratios are 1:3 and 1:1 for particles that stop in detectors four and five, respectively. In what follows we concentrate on the measurements for ions that stop in the third detector.

Using in-flight measurements it has been become common to display the quantity $\Delta E \cdot E_0$ versus $E_0/\Delta E$. The total measured energy and the energy loss in the first detector increase with the charge number and mass. The right panel of Fig. 2 displays the quantity $\Delta E \cdot E_0$ versus $E_0/\Delta E$ using the energy loss ΔE in the first detector D1 and the total measured energy E from detector D1 to detector D3. Indeed the traces of the different elements are visible ranging from hydrogen to the CNO group and above. The entries below the curves are mainly caused by the fact that the charge collection of the first detector is non uniform from a certain radius outward - decreasing with increasing radius.

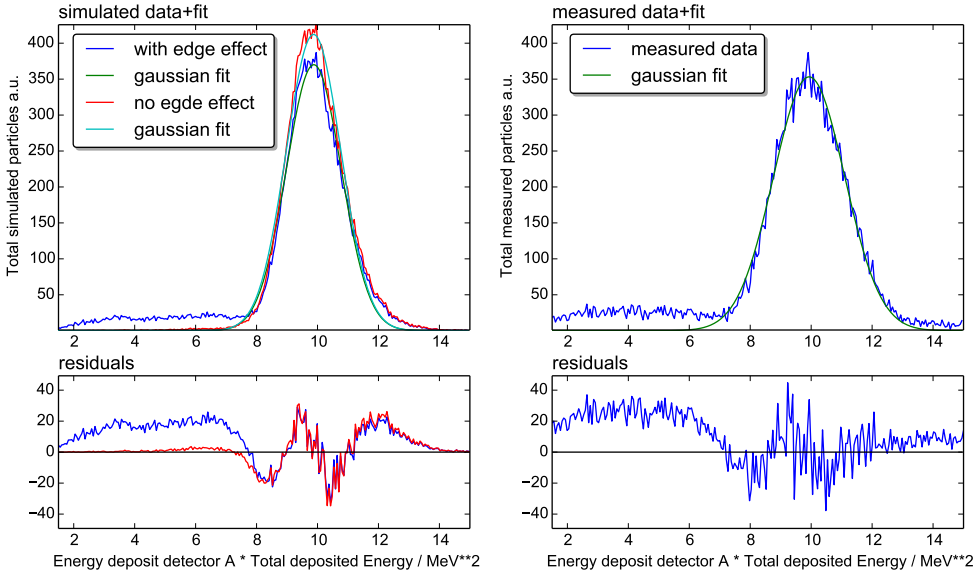

Figure 3. Measured and simulated $\Delta E \cdot E_0$ distribution of the proton peak in detector D1, demonstrating the measured and modelled edge effect.

In order to investigate this effect in more detail, the right hand panel of Fig 3 shows the measured $\Delta E \cdot E_0$-distribution close to the proton peak. The residuals to the left of the proton peak result from the so called ”edge effect”. Particles penetrating the detectors beyond their active region produce fewer charge carrier pairs because the electrical field does not drop immediately to zero. To confirm this, a GEANT4 (version 10.0) simulation utilizing the Bertini Cascade and the Quark Gluon string model was set up. The edge effect was modelled by multiplying a radius dependent efficiency to the signal. The corresponding results are displayed in the left panel of Fig. 3. From that figure it is evident that the model is capable to describe the edge effect in the first detector. Electronic effects like the amplification switch between high-gain and low-gain, responsible for the particle population between protons and helium, as well as noise were ignored in the simulation.

The chemical composition of galactic cosmic rays shows that a high signal to noise ratio is needed to determine the chemical composition for the CNO-group. Investigations from in-flight measurements of the second detector show an ”edge effect” with a significant smaller impact than that of the first detector.

Fig. 4 displays in the upper panel on the left and on the right the measured and corrected $\Delta E \cdot E$ versus $E/\Delta E$ distribution utilizing the energy loss ΔE in the second detector. Corrections include excluding rear electrons and rear particles by comparing energy deposits in the first two detectors as well as temperature corrections. In contrast to Fig. 2 we find a deviation from a straight line at low values of $\frac{E}{\Delta E}$. This is due

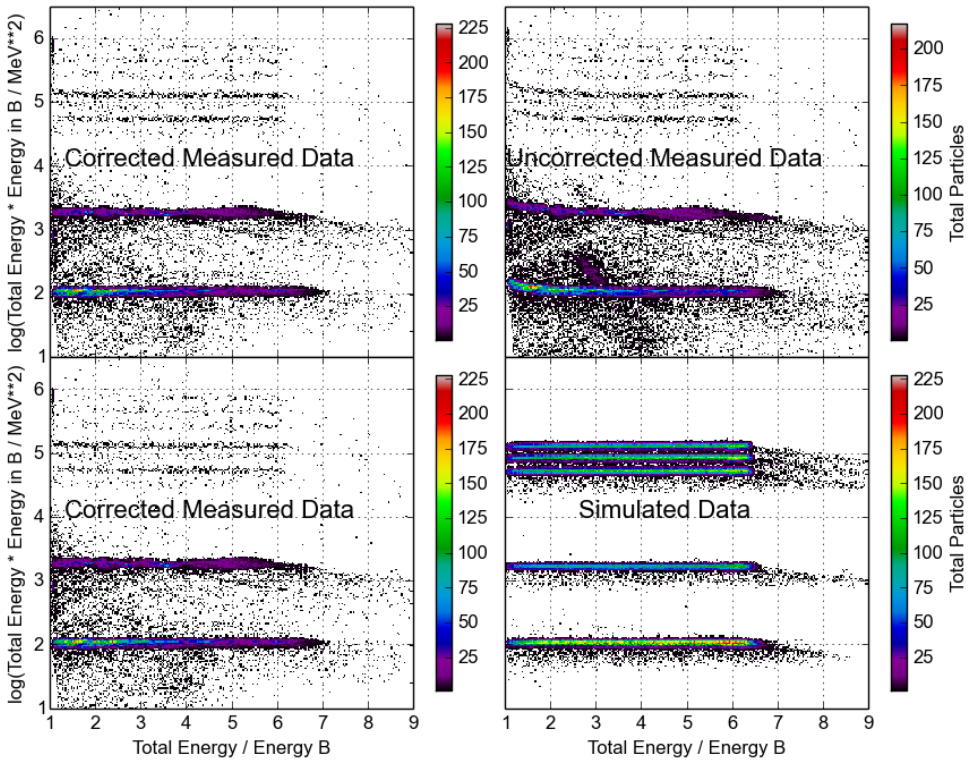

Figure 4. Upper panel uncorrected and corrected $\Delta E \cdot E$ vs. $\frac{E}{\delta E}$-measurements for particles that stop in the third detector utilizing the energy loss ΔE in the second detector. The lower panel displays the corresponding corrected simulated and measured matrix. Note that details can not be compared due to the different intensity energy spectra. For details see text.

to the fact that the energy loss is comparable to the total energy. However, that effect may be corrected by fitting a second order polynomial to the proton track. Multiplying the data by the corresponding inverse function leads to lines that are parallel to the $\frac{E}{\Delta E}$-axis. The lower row in Fig. 4 compares the simulation using an adapted model for the edge effects in the second detector and a flat energy spectrum with the measured and corrected distribution. The simulation was performed with a large number of particles in order to clearly show the tracks of protons, helium, carbon, nitrogen and oxygen. Comparing the simulated and measured corrected distributions we find a good agreement if we take into account that neither energy spectra, abundance, electrons nor and like ^{3}He have been taken into account.

4. Results

Energy spectra for galactic and if present, anomalous, protons, helium, carbon, nitrogen, and oxygen in the energy range from a few MeV/nucleon to several 100 MeV/nucleon were determined by Christian 1989, [10]. Fig. 5 displays 12 hour averaged count rates of ~13 to ~ 27 MeV/nucleon protons (black curve) and ions (red curve) from Helios 1 and Helios 2 from launch to September 1977, respectively. For our analysis only data with a proton count rate below 0.002 counts/second was used. The lower panel of Fig. 6 shows the simulated $\Delta E \cdot E$ distribution for helium and above. From that figure we find peaks that correspond to boron, carbon, nitrogen, oxygen, and neon. In order to determine the abundances, each peak was fitted with a corresponding Gaussian function. The corresponding lower panel shows the fit residuals which demonstrate the goodness of the fit. We find a typical width σ of 0.03 that allows us to separate between C, N , O, and Ne by more than 3σ. Note the small impact of the edge effect on the data between the fits compared to the strong edge effect on protons in detector A (Fig. 3). The

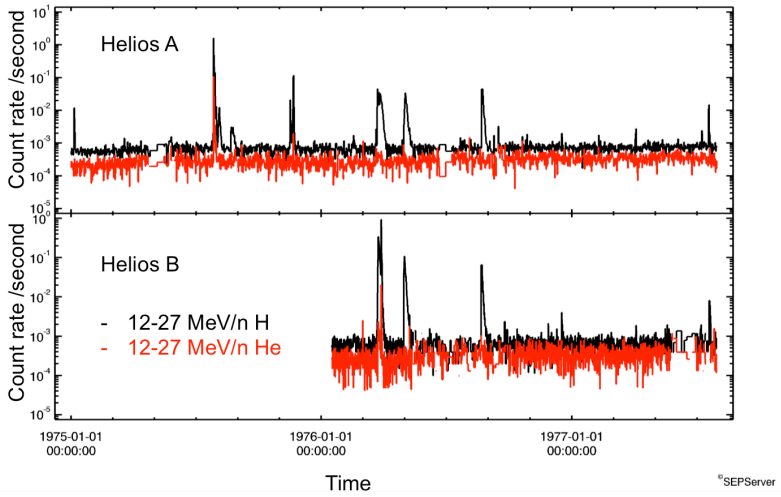

Figure 5. The upper and lower panel display the 12 hour averaged count rates of ~13 to ~ 27 MeV/nucleon protons (black curve) and ions (red curve) from Helios 1 and Helios 2 from launch to September 1977, respectively. For details see text.

Element	Position	σ	Total number	relative abundance (Si)
helium	3.27	0.03	11849	95500
boron	4.52	0.03	71	570
carbon	4.73	0.03	348	2790
nitrogen	4.94	0.03	102	820
oxygen	5.11	0.03	460	3700
neon	5.42	0.03	89	720
magnesium	5.66	0.03	119	960
silicon	5.86	0.03	124	1000

Table 2. Results of the fit using a Gaussion to the data in Fig.6. The position and σ give the position of the maximum and the width of the Gaussian in $\log(E_B \cdot E_{tot}/MeV^2)$. The total number is calculated by integration of the Gaussian function. The relative abundance is given with respect to silicon.

same was done with the measured data, leading to the results summarized in Tab. 2. In order to estimate the elemental separation of the instrument the figure displays the Gaussian fits for B, C, N, O, Ne, Mg, and Si. From this the background distribution can be analyzed further and the edge effect and possible further nuclei like ^{3}He can be investigated in more detail. The total number of counts varies between 70 for boron and 12000 for helium. Since abundances are given relative to silicon, the statistical accuracy cannot be better than 10% for helium and increases to more than 15% for boron. However, the relative abundances differ significantly from the ones given in Tab. 1. This can be explained mainly by the fact that in contrast to the work by [George et al. 2] the values are not normalized to a reference energy. While the channel analyzed here covers an energy range from 13 to 27 MeV/nucleon for helium, it measures heavier elements at much higher energies. Thus an extended analysis is needed that includes other energy channels from the Helios instrument in order to define a single energy range that is covered by all species.

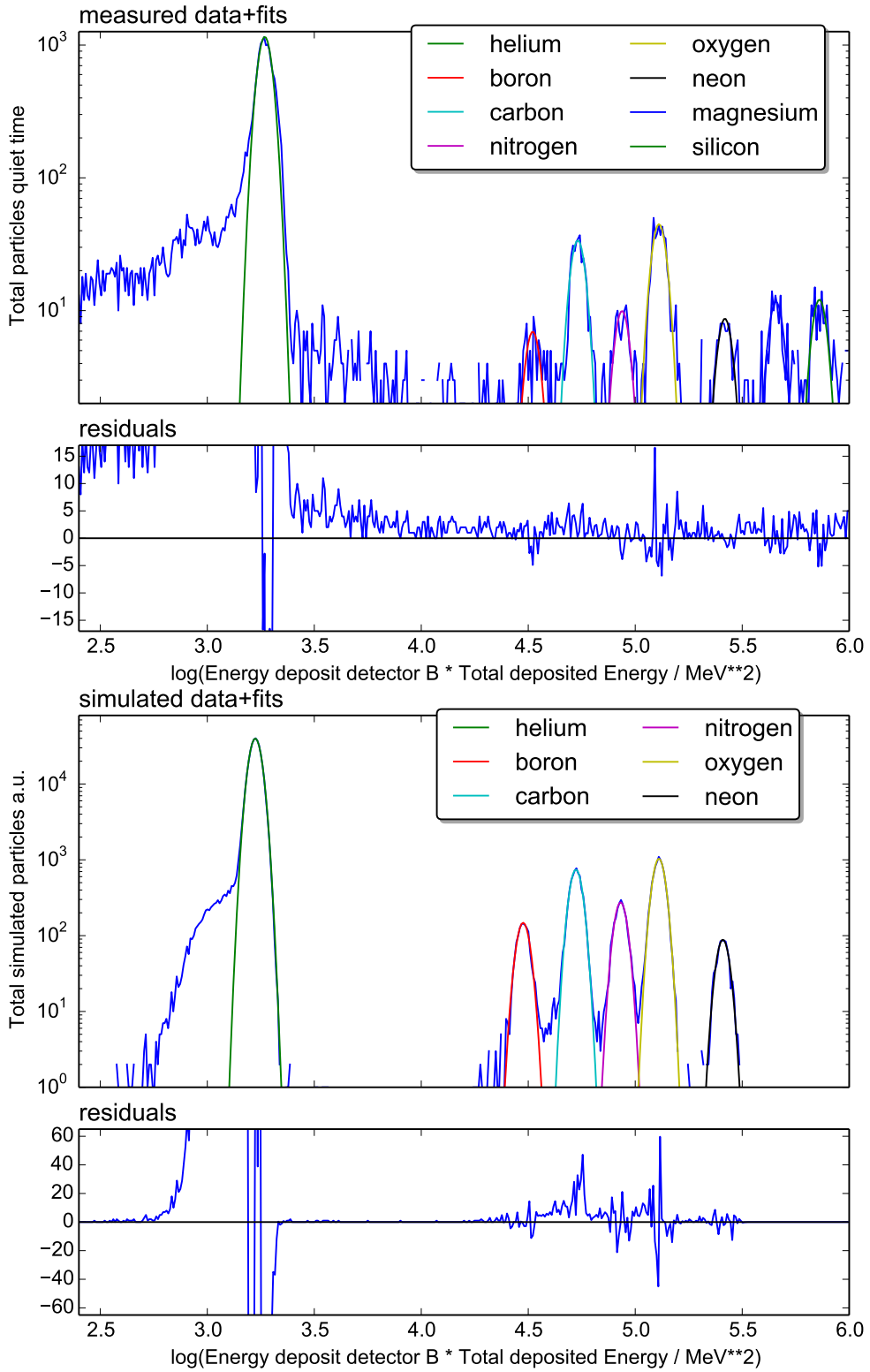

Figure 6. The blue curves show the left projection (1-dimensional representation) of the different measured elements and simulated distribution. The other colored curves are the result of fits by a Gaussian to the data. The bottom panels display the residuals of the fit, indicating the goodness of the fit. Note that the y-axis are on logarithmic and linear scale on the top and bottom, respectively.

5. Summary and future work

Here we analyzed in detail a channel that counts particles in the energy range from ~13 MeV/nucleon to ~27 MeV/nucleon for protons and helium. Using a modified $dE/dx - E$ method we could show that the instrument is capable of separating all major chemical elements from hydrogen to silicon. In order to determine their chemical composition a detailed instrument simulation for different particle species has been performed utilizing a newly developed model of the E6 instrument. This model includes the edge effect. Using a total quiet time span of four years measurements the instrument counted more than 10000 helium, about 350 carbon and 460 oxygen nuclei. This allows to investigate radial structures within the inner heliosphere. In order to determine the chemical composition at single energy intervals, other coincidence channels need to be evaluated and the corresponding response function calculated. The result of this analysis will allow us to investigate the chemical composition during the solar minimum from 1974 to 1977.

Acknowledgements

We acknowledge the use of the SEPServer data base: The SEPServer project has received funding from the European Community's Seventh Framework Programme (FP7/2007-2013) under grant agreement nr 262773.

Further we acknowledge the International Space Science Institute (ISSI) and the ISSI Team "Exploration of the inner Heliosphere what we have learned from Helios and what we want to study with Solar Orbiter".

References

[1] Engelmann J J, Ferrando P, Soutoul A, Goret P and Juliusson E 1990 *Astronomy and Astrophysics* **233** 96–111 1

[2] George J S, Lave K A, Wiedenbeck M E, Binns W R, Cummings A C, Davis A J, de Nolfo G A, Hink P L, Israel M H, Leske R A, Mewaldt R A, Scott L M, Stone E C, von Rosenvinge T T and Yanasak N E 2009 *Astrophysical Journal* **698** 1666–1681 1, 1, 4

[3] Ferrando P, Lal N, McDonald F B and Webber W R 1991 *Astronomy and Astrophysics* **247** 163–172 1

[4] Duvernois M A and Thayer M R 1996 *Astrophysical Journal* **465** 982 1

[5] McDonald F B and Ludwig G H 1964 *Physical Review Letters* **13** 783–785 1, 3, 3

[6] Heber B, Kopp A, Fichtner H and Ferreira S E S 2005 *Advances in Space Research* **35** 605–610 1

[7] Kunow H, Wibberenz G, Green G, Müller-Mellin R and Kallenrode M B 1991 *Physics of the Inner Heliosphere II. Series: Physics and Chemistry in Space* **21** 243–342 1

[8] Agostinelli S e 2003 *Nuclear Instruments and Methods in Physics Research Section A: Accelerators, Spectrometers, Detectors and Associated Equipment* **506** 250–303 1

[9] Lave K A, Wiedenbeck M E, Binns W R, Christian E R, Cummings A C, Davis A J, de Nolfo G A, Israel M H, Leske R A, Mewaldt R A, Stone E C and von Rosenvinge T T 2013 *Astrophysical Journal* **770** 117 1

[10] Christian E R 1989 *Evidence for anomalous cosmic ray hydrogen* Ph.D. thesis California Institute of Technology, Pasadena. 4

5.1.1 *Supplemental material: Edge effect*

As shown in Publication 1 (section 5.1), the edge effect of the first two detectors leads to several unintentional effects:

- From particles penetrating the edges of the detectors only a fraction of the deposited energy can be measured. This has the following implications:
  - Protons penetrating the edge of detector 1 can be interpreted as electrons in the countrates
  - The properties from particles penetrating the edges can't be correctly identified in the PHA data.
- The exact effective size of the detectors is unknown. The response function depends on the exact size, efficiency and thresholds of the detectors as well as deposited energy in the detector. Because of the edge effects, the response can vary significantly depending on the particle energy.

In Figure 26 the left panel displays PHA data from the E08 (nominally electrons from 0.8 to 2 MeV) for the year 1978. Without the edge effect, there would be no particles above the red line. Those entries are from protons penetrating the edge of detector 1, as shown in the middle panel, or the edges of detectors 1 and 2, as shown in the right panel.

To correct for this effect, the exact function of the efficiency decrease needs to be determined. There are two approaches to do this: Heber [1989] measured the efficiency decrease function with a spare model of the E6 several years after launch. In this work, it is attempted to reconstruct the function with the inflight data.

The reconstruction utilizes proton PHA data from the P13 (nominally protons from 13 to 27 MeV) and the E08. Protons will only be detected in the E08 channel, if they didn't surpass the first detectors threshold. In Figure 27 the upper panel shows the different efficiency models for detector 1 and 2. The lower two panels show the $dE/dx \cdot E$ distributions for the channels P13 and E08, respectively. The $dE/dx \cdot E$ distribution in the P13 channel is mostly dependent from the edge effect of the first detector, while the $dE/dx \cdot E$ distribution in the E08 channel depends only from the edge effect of the second detector. Therefore, the colour used in these panels correspond to the edge models used in the simulation: For example, the edge model from [Heber, 1989] for detector 1 (blue) results in the blue distribution in the middle panel.

Also shown in the lower two panels are the measured $dE/dx \cdot E$ distributions from inflight data for comparison. The new model from this work was created by reproducing the measured distribution in the simulation.

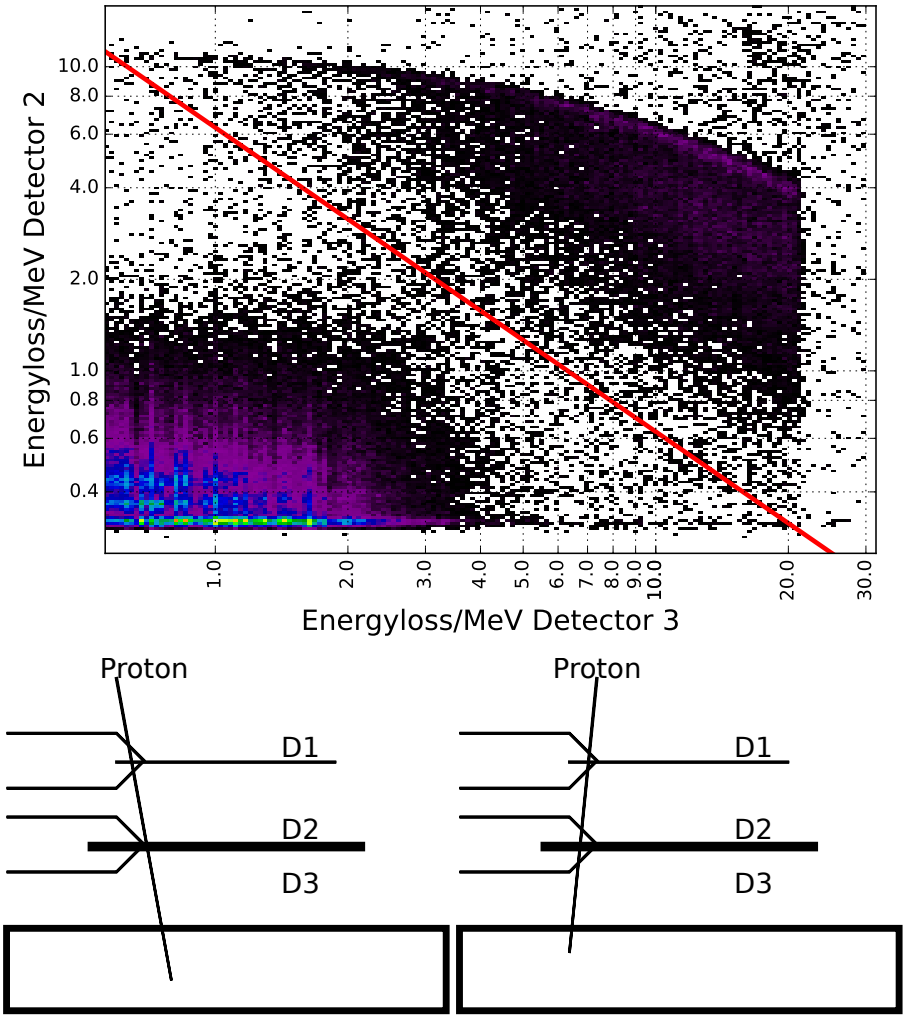

Figure 26: top: Energy loss in detector 2 versus detector 3 measured in the E08-channel in 1978. The red line separates electrons (below) and protons from each other. The lower left and right panels display particle trajectories that lead to entries along and below the proton track, respectively. Adapted from [Hörlöck et al., 2019]

The fluxes in the two bottom panels are to the same scale, meaning that a substantial amount of protons falls below the threshold of the first detector. A sizeable amount of this population deposits the nominal amount of energy in the second detector at roughly 3.05 in the lower panel. This implicates that the nominal size of the second detector already extends beyond the total sensitive area of the first detector.

The ratio of protons lost from the P13 to the E08 is given by summing up the flux in the lower panel and dividing it by the summed up flux of the middle panel. This ratio is 0.38, which means that the mean effective size of detector 2 is 1.37 time larger than detector 1. This can result in a large proton contribution in the electron countrates, depending on the fluxes.

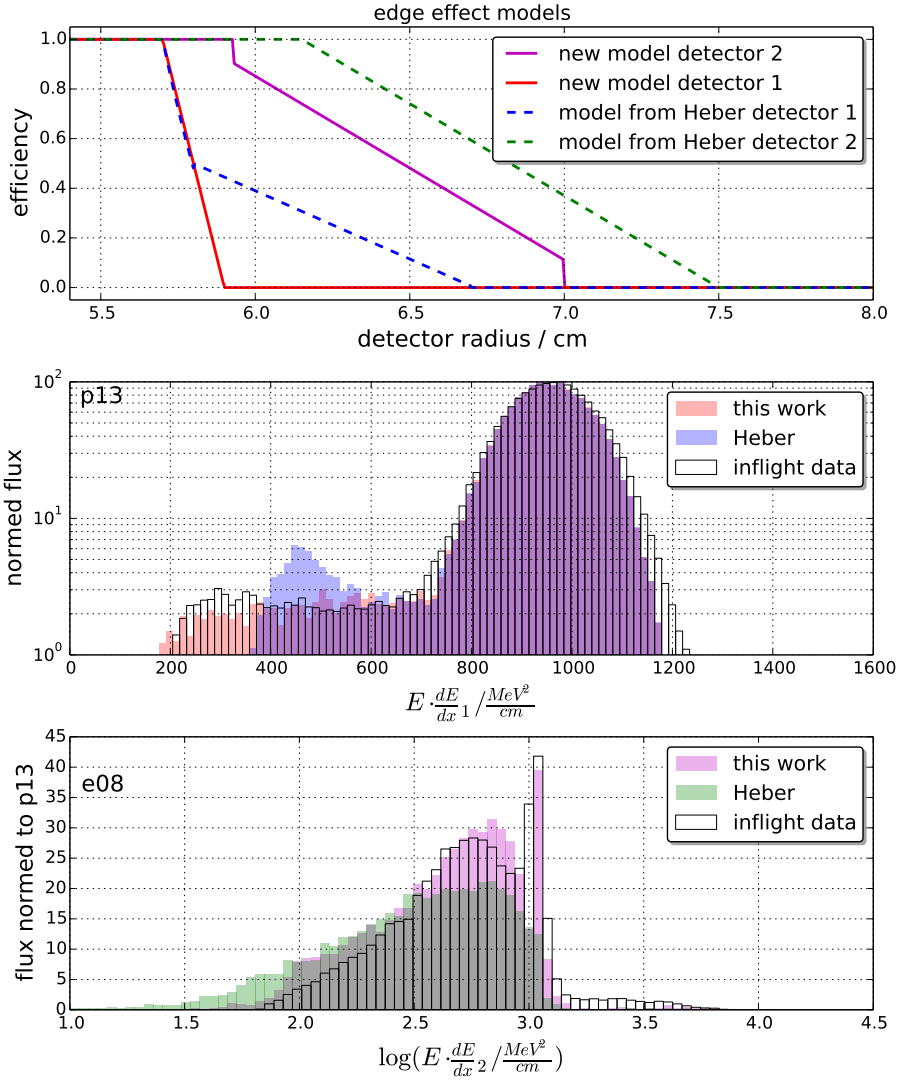

Figure 27: reconstructions of the edge effects of detector 1 and 2 in the top panel. The lower two panels show the $\frac{dE}{dx}$E distributions for the channels P13 and E08, respectively. The colours in the lower two panels correspond to the edge models in the top panel used for the simulation. The fluxes in the middle panel and the bottom panel have both been normed to the maximum flux in the P13 channel.

6

MODULATION OF THE COSMIC RADIATION

GCRs enter the heliosphere from outside and are modulated by the heliospheric plasma originating from the Sun, the solar wind. The solar wind flows radially outwards from the rotating Sun, resulting in an Archimedean spiral, called Parker spiral.

Embedded in the solar wind is it's magnetic field, which remains rooted in the photosphere of the Sun and thus follows the Parker spiral. The boundary surface between the two magnetic polarity hemispheres of the Sun's dipole field is called heliospheric current sheet. The magnetic field dipole axis and the solar rotation axis are tilted with respect to each other, so the structure will resemble a ballerina skirt, see Figure 28.

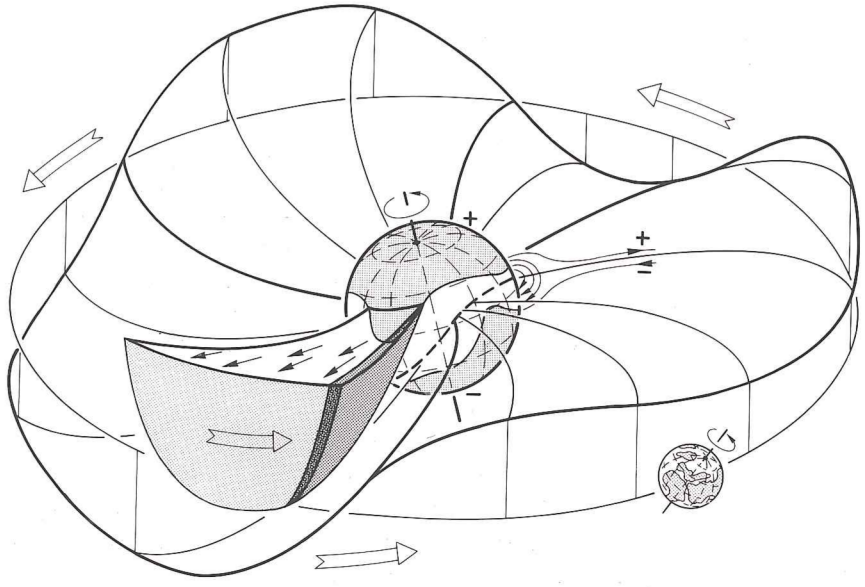

Figure 28: Model of the inner heliosphere during solar minimum, in terms of the "ballerina" model [Schwenn and Marsch, 1990][Schwenn, 1981]

On top of this global structure, there are non static small scale variations of the magnetic filed, like Alven-waves. Those small scale variations serve as scattering centres for the Cosmic Rays. Some possible particle-wave-interactions are shown in Figure 29. Those scattering centres are assumed to be frozen in the solar wind and travel with the solar wind speed v_S and direction and thus in general radially outwards from the Sun. The Cosmic Rays are convected with them.

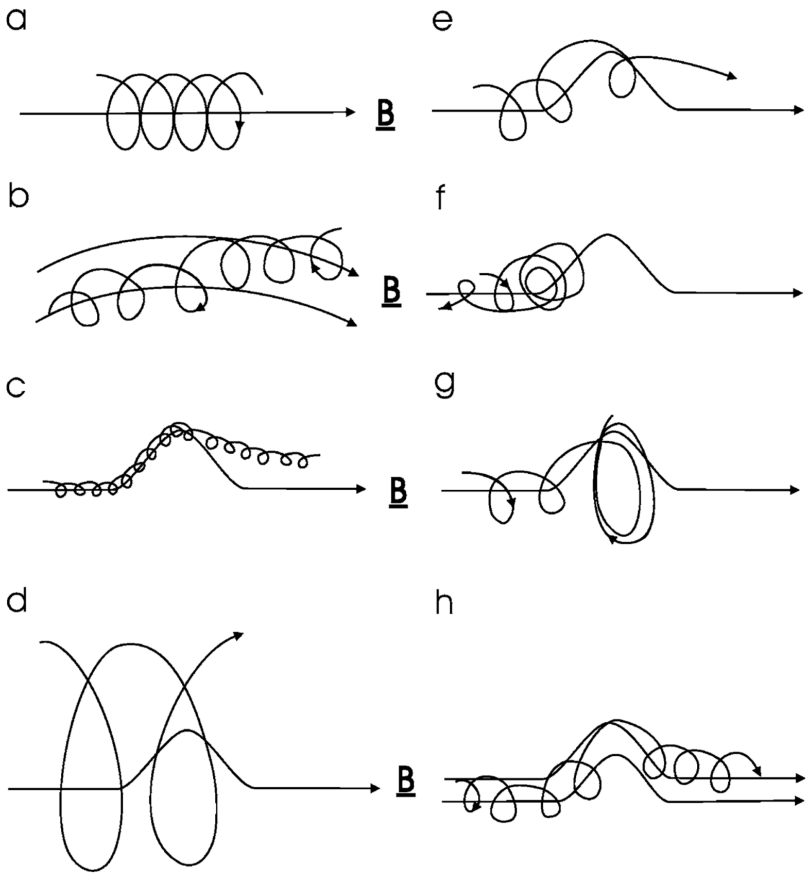

Figure 29: several magnetic field configurations and corresponding charged particle trajectories with different gyro-radii from [Moraal, 2013]

Opposed to this convection is the diffusion. The Cosmic rays are assumed to diffuse inside the heliosphere with a given, non constant diffusion coefficient, κ.

The one dimensional diffusion-convection-equation is obtained by setting the total particle flux J as the difference of these two opposing processes:

$$J = \kappa \cdot \frac{\partial n}{\partial r} - v_S \cdot n$$

where n is the number density of particles. The three dimensional differential form in polar coordinates can be shown to be

$$\frac{\partial n}{\partial t} + \frac{v_S}{r^2}\frac{\partial}{\partial r}(r^2 n) - \frac{1}{r^2}\frac{\partial}{\partial r}\left(\kappa r^2 \frac{\partial n}{\partial r}\right) = 0$$

by assuming $\nabla \cdot N = -\partial n/\partial t$, v_S =konst. and the flow to be spherically symmetric.

Now we also take into account possible Energy changes of the particles. For any given $\frac{\partial E}{\partial t} \neq 0$ this leads to an additional term in the equation.

Parker assumed that the solar wind cools down adiabatically like an expanding, ideal gas. The Energy change of an ideal expanding gas equals

$$\frac{\partial E}{\partial t} = -\frac{2}{3}(\boldsymbol{\nabla} \cdot v_S)E$$

This equation has also been derived by Ruffolo [1995] using a Focused Transport model. Since the Cosmic Rays couple to a cooling gas, they loose kinetic energy as well, leading Parker [1965] to assume the same $\frac{\partial E}{\partial t}$ for Cosmic Ray particles. The term is often called adiabatic cooling, even if this is highly misleading, since by interaction with a down cooling medium the cooling of the Cosmic Rays can not formally be called adiabatic. This leads to following equation

$$\frac{\partial n}{\partial t} + \frac{v_S}{r^2}\frac{\partial}{\partial r}(r^2 n) - \frac{1}{r^2}\frac{\partial}{\partial r}\left(\kappa r^2 \frac{\partial n}{\partial r}\right) - \frac{2}{3}\frac{v}{r}\frac{\partial}{\partial E}(nE) = 0$$

This is, however, not analytically solvable. A solvable approach first needs the introduction of another effect:

We observe a flux convected by the solar wind, we still need to correct for relative motion of the observer with respect to the solar wind. This leads to a correction factor for the observed flux, the Compton-Getting factor, introduced for Solar modulation by [Gleeson and Axford, 1968b] and rewritten in [Moraal, 2013] as:

$$C = -\frac{1}{3}\frac{\partial}{\partial}\frac{\log n}{\log p}$$

Now we reduce the formula to its steady one-dimensional form and neglect adiabatic energy changes:

$$\kappa \cdot \frac{\partial n}{\partial r} - C \cdot v_S \cdot n = 0$$

The Force Field Solution (FFS) is an often used, one parametric approximation of the Solar Modulation achieved by solving this expression. In the solution, usually the flux J instead of the particle density n is used, however, the assumptions and general solution are the same. The flux J of a particle with kinetic Energy T is given as [Gleeson and Axford, 1968a]

$$J_i(\Phi) = J_{LIS,i}(T + \Phi)\frac{T + 2E_{0,i}}{(T + \Phi)(T + \Phi + 2E_{0,i})}$$

J	=	flux
Φ	=	$(Ze/A)\phi$
Ze	=	charge of the particle
A	=	mass number of the particle
ϕ	=	Modulation Parameter
J_{LIS}	=	Local Interstellar Spectrum

The Modulation Parameter ϕ has the dimension of a force field, hence the name, but should not be interpreted as such, since the particles energy does not change in our assumptions.

Because of the solar modulation of Cosmic Rays, their spectra not only change in dependence of time, but also location. HELIOS A was the first spacecraft carrying an instrument able to measure spectra of ACR and GCR in the inner heliosphere. Because of the launches of Solar Orbiter and Parker Probe Plus the aim of this publication is to provide spectra of ACR and GCR oxygen during the quiet solar phase of the HELIOS missions for reference.

6.1 PUBLICATION 2: ENERGY SPECTRA OF CARBON AND OXYGEN WITH HELIOS E6. RADIAL GRADIENTS OF ANOMALOUS COSMIC RAY OXYGEN WITHIN 1 AU

As reference for the HELIOS E6 near Earth the Charged Particle Measurements Experiment (CPME) onboard Interplanetary Monitoring Platform (IMP)-8 [Sarris et al., 1976] is used. IMP-8 was sending data from October, 1973 to October, 2006. The instrument was able to measure fluxes of protons in 11 energy channels between 0.29 and 140 MeV, and alpha particles in 6 channels between 0.64 and 52 MeV/n.

While the E6 is located at 1 AU for short periods of time, it is almost never at the same location as the CPME because of the different orbit periods around Sun. Because of this, the spectra of the two instruments are different most of the time as phenomena like CIRs are heavily dependent on solar latitude. By averaging over a long enough time frame it is assumed that the quiet time spectra of the CPME and the E6 correspond to each other at 1 AU.

In the publication carbon and oxygen spectra as well as the radial dependence of the latter one are shown. The carbon spectrum and the oxygen spectrum close to 1 AU match quite well with measurements from IMP-8, while the radial gradient of ACR-oxygen is much larger than in the outer heliosphere, see Figure 6 in [Marquardt et al., 2018].

The obtained gradients, however, support the prognosis of the gradient decreasing with distance from Sun calculated by Strauss and Potgieter [2010].

A&A 610, A42 (2018)
https://doi.org/10.1051/0004-6361/201731490

Astronomy & Astrophysics

Energy spectra of carbon and oxygen with HELIOS E6

Radial gradients of anomalous cosmic ray oxygen within 1 AU

J. Marquardt[1], B. Heber[1], M. S. Potgieter[2], and R. D. Strauss[2]

[1] Christian-Albrechts-Universität zu Kiel, Leibnizstr. 11, 24118 Kiel, Germany
e-mail: marquardt@physik.uni-kiel.de
[2] Centre for Space Research, North-West-University, Potchefstroom 2520, South Africa

Received 3 July 2017 / Accepted 6 December 2017

ABSTRACT

Context. Anomalous cosmic rays (ACRs) are well-suited to probe the transport conditions of cosmic rays in the inner heliosphere. We revisit the HELIOS data not only in view of the upcoming Solar Orbiter experiment but also to put constraints on particle transport models in order to provide new insight into the boundary conditions close to the Sun.
Aims. We present here the energy spectra of galactic cosmic ray (GCR) carbon and oxygen, as well as of ACR oxygen during solar quiet time periods between 1975 to 1977, utilizing both HELIOS spacecraft at distances between ∼0.3 and 1 AU. The radial gradient ($G_r \approx 50\%$/AU) of 9–28.5 MeV ACR oxygen in the inner heliosphere is about three times larger than the one determined between 1 and 10 AU by utilizing the Pioneer 10 measurements.
Methods. The chemical composition as well as the energy spectra have been derived by applying the $dE/dx - E$-method. In order to derive these values, special characteristics of the instrument have been taken into account.
Results. A good agreement of the GCR energy spectra of carbon and oxygen measured by the HELIOS E6 instrument between 0.3 and 1 AU and the Interplanetary Monitoring Platform (IMP) 8 at 1 AU was found. For ACR oxygen, we determined a radial gradient of about 50%/AU that is three times larger than the one between 7 and 14 AU, indicating a strong change in the inner heliosphere.

Key words. Sun: heliosphere – solar-terrestrial relations – cosmic rays

1. Introduction

The current paradigm of anomalous cosmic rays (ACRs) can be summarized as follows: interstellar neutrals that have been swept into the heliosphere are ionized in the heliosphere to become so-called pickup ions (PUIs; Fisk et al. 1974). Because of their high ionization potentials, He, N, O, and Ne are able to penetrate to within a few AU of the Sun before this happens (see Drews et al. 2016, and references therein). These singly ionized PUIs (Moebius et al. 1985) are subject to the Lorentz force and are therefore bound to the outward convecting heliospheric magnetic field. They become accelerated at the heliospheric termination shock (Pesses et al. 1981) and then diffuse into the heliosphere as mainly singly ionized energetic particles (Klecker et al. 1995). The crossings of the termination shock first by Voyager 1 (V1) and later by Voyager 2 (V2) have led to a new paradigm because the ACR spectra were not of the expected form (Decker et al. 2005). Several alternative acceleration models have been introduced since then (for a review, see Potgieter 2013, and references therein).

The interaction of energetic charged particles with the heliospheric magnetic field (HMF) reduces their intensities with decreasing distance to the Sun. Transport effects, in particular the adiabatic energy lose effect, yield the well known $I(E) \propto E$ proportionality for galactic cosmic rays (GCRs) at energies below about 100 MeV nucleon^{-1} (for a review, see Moraal 1993, and references therein).

Figure 1 displays the quiet-time energy spectra of hydrogen, helium, oxygen, nitrogen and carbon as measured during the 1970s solar minimum. While hydrogen shows the expected energy dependence with $I(E) \propto E^1$, all other elements show an upturn in the spectrum that is caused by the anomalous component that is most prominent for oxygen and nitrogen. Thus ACRs were first recognized by their different spectral shape at low energies (Hovestadt et al. 1973; Garcia-Munoz et al. 1973). The radial and latitudinal distribution of ACRs in the heliosphere can be determined by studying the evolution of the energy spectra of ions as a function of radial distance as well as latitude. The resulting radial and latitudinal gradients are therefore important to understand the transport of energetic particles in the heliosphere. Most studies concentrate on the gradients in the outer heliosphere using data from the pioneering space missions launched in the 1970s, such as Pioneer 10, Pioneer 11, V1, and V2, with the Interplanetary Monitoring Platform (IMP) 8 utilized as a baseline for their studies (see Fig. 1).

Webber et al. (1977) found a mean radial gradient of 20%/AU with a value of 25%/AU within 5 AU and 10%/AU from 5 to 10 AU, and of 5%/AU beyond 10 AU for anomalous oxygen. In a later publication, Webber et al. (1979) revised the values to 15%/AU. This value was used by Trattner et al. (1995, 1996) for the 1990s $A > 0$-solar magnetic epoch in order to determine the latitudinal gradients utilizing Ulysses and Solar Anomalous and Magnetospheric Particle Explorer (SAMPEX) measurements. However, Cummings et al. (1990, 1995) found the radial gradient to depend on the radial distance as $r^{-0.96}$ and $r^{-1.7}$ for an $A < 0$ and $A > 0$ solar magnetic epoch, respectively. Recent determinations of the radial gradient were performed by Cummings et al. (2009) for an $A < 0$-magnetic epoch utilizing

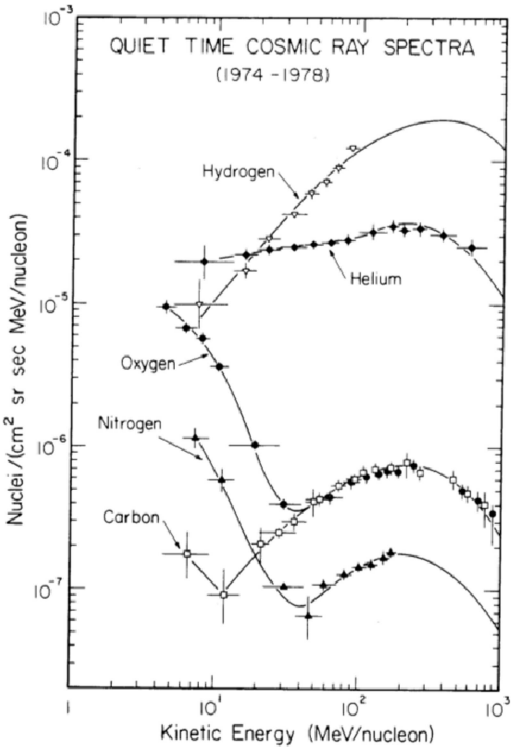

Fig. 1. Quiet-time energy spectra for the elements H, He, C, N, and O measured at 1 AU over the period from 1974 to 1978. We note the "anomalous" enhancements in the low-energy spectra of He, N, and O (Fig. 1.2 of Christian 1989).

the measurements from the low-energy telescopes aboard the Solar Terrestrial Relations Observatory (STEREO) A and B and Ulysses leading to a radial gradient of 45%/AU and 51%/AU at 4.5 to 15 and 7.3 to 15.6 MeV nucleon^{-1}, respectively. Because of the strong dependence of the radial gradient on distance, larger radial gradients are expected in the inner than in the outer heliosphere. The only future measurements of ACR oxygen within the inner heliosphere will be performed by the *Parker* Solar Probe (Fox et al. 2016). However, recently we showed that the HELIOS E6 detector (Kunow 1981) is capable of separating the chemical composition up to neon (Marquardt et al. 2015). Therefore, we revisit here the energetic particle measurements gathered by the HELIOS experiment during the solar minimum from 1974 to 1977. In what follows, we apply the pulse height analysis developed by Marquardt et al. (2015) in order to determine reliable energy spectra for carbon and oxygen to infer the non-local differential radial gradient for ACR oxygen in the inner heliosphere between ~0.3 and 1 AU.

2. HELIOS and experiment 6 (E6)

HELIOS A and HELIOS B were launched on December 10, 1974 and January 15, 1976, respectively. The two almost identical space probes were sent into ecliptic orbits around the Sun. The orbital period around the Sun was 190 days for HELIOS A and 185 days for HELIOS B, and their perihelia were 0.3095 and 0.290 AU, respectively. The upper panels of Figs. 2 and 3 display the radial distance of HELIOS A and B from the launch of HELIOS A in 1974 to the end of 1978, receptively. Marked by the green and blue shaded regions are the close and far periods for which the spacecraft were within 0.45 AU and beyond 0.9 AU from the Sun. The lower panels of both figures indicate

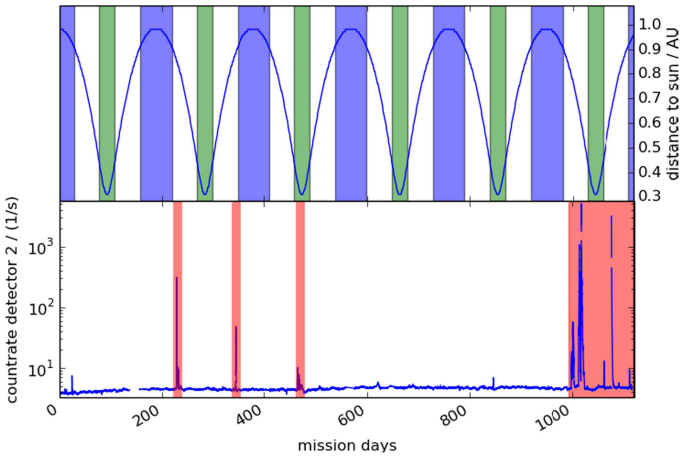

Fig. 2. *Upper panel*: radial distance of the HELIOS A spacecraft from the Sun. Indicated by the green and blue shaded regions are the close and far periods for which the spacecraft was within 0.3 and 0.45 AU, and 0.9 and 1 AU, respectively. *Lower panel*: count rate of $Z \geq 2$ ions with energies from about 4 to 13 MeV nucleon^{-1} for helium. Shaded periods have been omitted in our analyses.

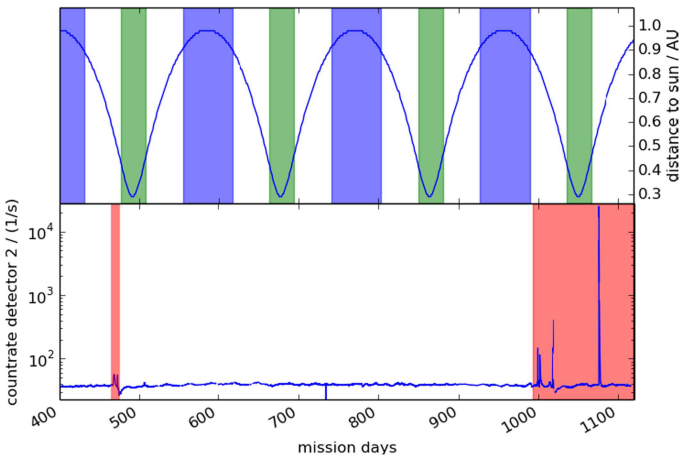

Fig. 3. Similar to Fig. 2, but for HELIOS 2.

the hourly averaged count rate of 4 to 13 MeV nucleon^{-1} ions with $z \geq 2$. Time periods that indicate intensity increases due to solar energetic particle events are indicated by the red shaded regions and have been omitted in our analysis.

The Kiel experiment, E6, has been described in detail by Kunow (1981). It is one of three particle detectors aboard HELIOS that allowed the study of energetic particles in the energy range from 1.3 MeV nucleon^{-1} to above 1000 MeV nucleon^{-1} for ions and from 0.3 to 8 MeV for electrons. Recently, Marquardt et al. (2015) showed that the instrument is capable of determining the chemical composition from hydrogen to neon in the energy range from a few to several tenths of a MeV nucleon^{-1}.

The detector system is sketched in Fig. 4 and consists of five semi-conductor detectors of increasing thickness indicated in the figure; while the first two detectors, D1(A) and D2(B), are silicon-surface-barrier detectors with a thickness of 100 and 1000 μm, the other three are lithium drifted detectors with a thickness of 3000 μm. The first two (D1 and D2) are used for determining the lowest energy channels for the definition of the geometry factor for stopping particles (energy ranges

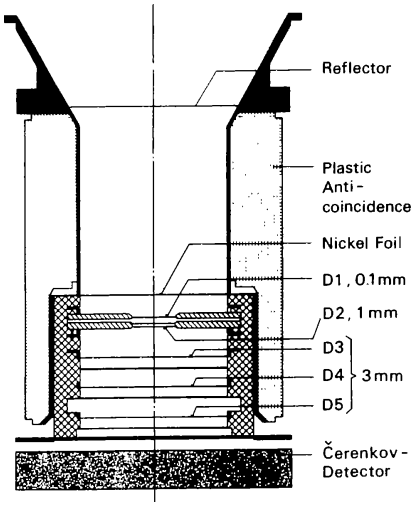

Fig. 4. Schematic of the HELIOS E6 (adapted from Marquardt et al. 2015).

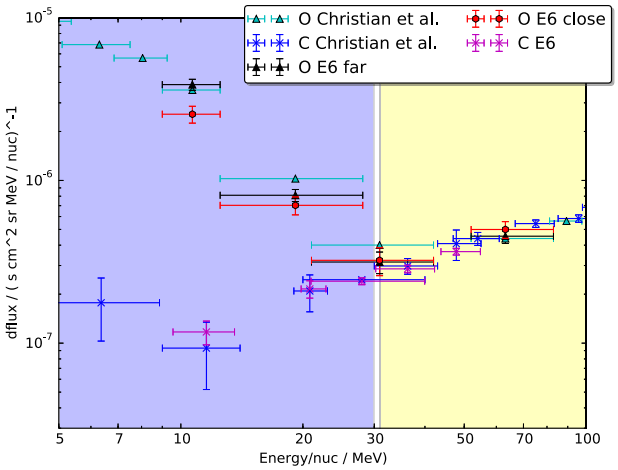

Fig. 5. Energy spectra of carbon and oxygen measured by the E6 in comparison with the data taken from Fig. 1.

below 51 MeV nucleon^{-1}), as well as for discriminating between electrons and ions. Since the thickness of 100 μm does not allow us to measure minimum ionizing particles, electrons are separated from ions by the following trigger conditions:

– no signal in the first detector $\longrightarrow$ electron;
– signal in the first detector $\longrightarrow$ ion.

To avoid false identifications by these discrimination conditions, the first and second detectors are as close as possible to each other. Charged particles, which penetrate the fifth detector and the aluminum absorber beneath, are detected in the Sapphire-Cerenkov-detector. The Cerenkov-threshold for this material (n = 1.8) is E_s = 210 MeV nucleon^{-1}. Because the Sapphire-Cerenkov-detector also delivers scintillation light, particles in the energy range above 51 MeV nucleon^{-1} are included in an integral channel.

3. Data correction and analysis

The E6 particle telescope relies on the dE/dx – E-method (see e.g. McDonald & Ludwig 1964). In order to interpret the measured data, a detailed understanding of the instrument is needed and can be obtained by modelling the physical processes inside the detector taking into account the instrument geometry as well as the environment (e.g. Heber et al. 2005; Marquardt et al. 2015). We need to correct for the so-called edge effects. Due to the decreasing charge collecting efficiency, from a certain radius outward the measured energy loss is spatially-dependent. This effect is particularly severe for the first two detectors, as described by Marquardt et al. (2015). Figure 5 displays the energy spectra of carbon (magenta symbols) and oxygen (black and red symbols) measured by HELIOS E6, binned in the same way as the energy spectra shown in Fig. 1. For oxygen we were able to restrict the time period under investigation to the periods when the spacecraft was beyond 0.9 AU. Due to the limited counting statistics, the whole time period, including periods when the spacecraft was close to the Sun, has to be used for carbon. The values for carbon (blue symbols) and oxygen (green symbols) from Fig. 1 have been added, indicating a reasonable agreement between the HELIOS and IMP observations. We note that for oxygen we utilized time periods when the spacecraft was beyond 0.9 AU. Due to the reduced statistics we need to take into account all periods for carbon, including the ones when HELIOS is within 0.9 AU. Therefore, we utilize only the HELIOS measurements in what follows. In order to determine radial gradients in the inner heliosphere, we divide the radial distances from the Sun into a set of measurements obtained during all far (1.0–0.9 AU) and close (0.45–0.3 AU) time periods (see Figs. 2 and 3). Since an upturn in the energy spectra is notable for energies below 30 MeV nucleon^{-1}, oxygen ions below and above 30 MeV nucleon^{-1} are classified as ACRs and GCRs, respectively. For carbon, the total number of observed particles is insufficient to determine a radial gradient.

4. Results

Table 1 and Fig. 5 summarize the oxygen fluxes measured by HELIOS E6. The fluxes for oxygen are given in the same energy ranges as for IMP 8 (see Fig. 1). We use the fluxes during the far periods as a proxy for the 1 AU measurements.

Table 1 provides the oxygen fluxes in the energy range 9–28 MeV nucleon^{-1}, similar to the energy range of 19–23.5 MeV nucleon^{-1} used by Webber et al. (1981). Assuming that temporal changes of the ACR oxygen flux are smaller than radial changes, we can calculate the corresponding radial gradient, G_r, as

$$G_r = \ln\left(\frac{I_{far}}{I_{close}}\right)\frac{1}{\Delta r} \quad (1)$$

using Δr = 0.6 AU. These gradients are summarized in Table 2. The uncertainties given in the table take into account the statistical uncertainties only.

For GCR oxygen the ratio I_{far}/I_{close} is consistent with unity, thus implying a very small radial gradient. Webber et al. (1981) investigated the radial gradients of ACR oxygen measured from 1972 to 1980 by the Pioneer 10 and IMP spacecraft. They showed that the radial gradient had only slight variations from 1974 to 1977 when Pioneer 10 moved from about 7 AU to about 14 AU. In their Fig. 2 they give a mean value of G_r = 15 %/AU. The upper panel of Fig. 6 shows the Pioneer 10 to IMP ratio in the energy range between 9 and 28.5 MeV nucleon^{-1} as a function of radial distance for the solar minimum period of solar cycle 22. The data are taken from (Webber et al. 1981) Fig. 2, and indicated on the figure by magenta triangles. In addition, the HELIOS close to far ratio, at ~0.38 AU, obtained during the time span from 1975 to

Table 1. Oxygen (O) fluxes I_{far} and I_{close} and their relative uncertainty averaged over all time periods marked in Figs. 2 and 3 for time periods when the spacecraft distance were >0.9 and <0.45 AU, respectively.

Element	E_1 MeV nuc^{-1}	E_2 MeV nuc^{-1}	I (far) p cm^{-2} sr s MeV nuc^{-1}	ΔI %	I (close) p cm^{-2} sr s MeV nuc^{-1}	ΔI %
O	9	13	3.88×10^{-6}	7	2.55×10^{-6}	11
O	13	28	0.811×10^{-6}	8	0.703×10^{-6}	12
O	21	48	0.315×10^{-6}	15	0.323×10^{-6}	19
O	52	83	0.454×10^{-6}	9	0.500×10^{-6}	11
O	9	28.5	1.37×10^{-6}	6	1.04×10^{-6}	4
O	30	85	0.435×10^{-6}	4	0.459×10^{-6}	3

Notes. The first two columns give the lower and upper energy limits.

Table 2. Average radial gradients G_r and their lower and upper limits, in the last two columns, for the energy range summarized in Table 1.

Element	E_1 MeV nuc^{-1}	E_2 MeV nuc^{-1}	G_r %/AU	G_r^l %/AU	G_r^u %/AU
O	9	13	73	50	99
O	13	28	25	0	54
O	21	48	−4	−43	45
O	52	83	−17	−41	12
O	9	28.5	48	36	60
O	30	85	−10	−20	0

mid 1977, is included as the black square. The middle and lower panels of the figure show the radial gradient, calculated by using Eq. (1), as a function of time and distance. From this figure it is evident that a strong increase with decreasing distance in the radial gradient must occur in the inner heliosphere within 2 AU.

The red triangles in the lower panel of Fig. 6 show the results of the computations described by Strauss & Potgieter (2010). Whereas the computations show an increase of the ACR-oxygen gradient from 14 AU inwards, peaking between 2 and 3 AU, the Pioneer 10 measurements show a nearly constant radial gradient of about 10 to 15%/AU from 3 to 14 AU, but the gradient then follows the predicted trend beyond 10 AU. However, the HELIOS measurements indicate a larger radial gradient that is in good agreement with the maximum gradient of the model, although much closer to the Sun. Pioneer 10 measurements between 7 to 14 AU coincide with the time of the HELIOS observations.

The results shown in Fig. 6 therefore indicate that ACR oxygen can easily penetrate into the inner heliosphere within 0.6 AU. The fact that the model and observations agree beyond ~10 AU is indeed encouraging, even more so that the maximum value of the gradient, $G_r^{max} \sim 45$%/AU, also seems to be consistent with the model prediction.

The quantitative differences between the model and observations should, however, be investigated in detail in future. Reasons for the disagreement may include: (1) Since the Pioneer observations within 7 AU were obtained during a different phase of the solar cycle, these measurements may be influenced by temporal effects, while the computations are solutions of a steady-state model. (2) Near the Sun, and especially within 1 AU, the inner boundary condition assumed in the model may influence the calculated gradient (see also the discussion by Strauss & Potgieter 2010). (3) The assumed Parker (1965) transport equation might

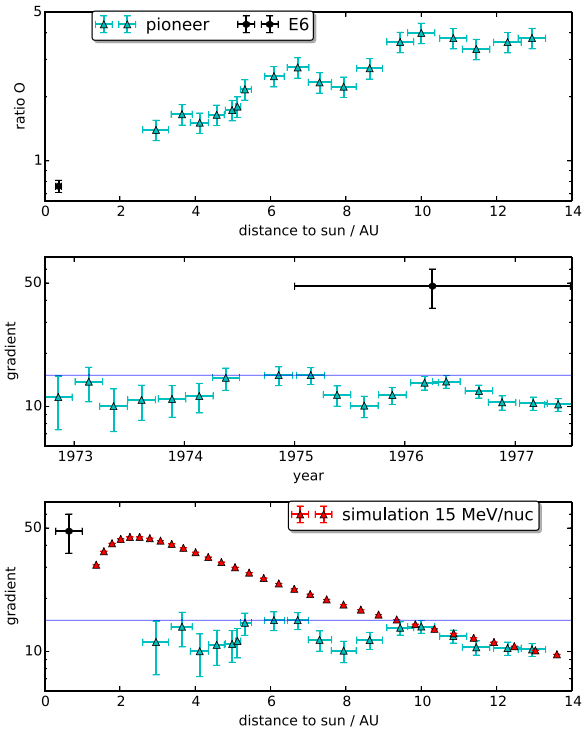

Fig. 6. *Upper panel*: radial dependence of the ACR oxygen flux ratio in the energy range between 9 and 23.5 MeV nucleon^{-1}. Data beyond 1 AU are taken from Webber et al. (1981). *Middle* and *lower panels*: temporal and radial variation of the radial gradient. The red symbols show the computations from the modelling of Strauss & Potgieter (2010).

not be valid closer to the Sun as magnetic focussing can lead to an anisotropic ACR distribution. (4) Ultimately, the computed gradients depend on the diffusion and drift coefficients as assumed in the model. They, on their part, are based on the underlaying assumed turbulence, diffusion, and drift theories, which may need to be refined for ACR oxygen by observance of the new measurements presented here.

5. Summary and conclusion

Marquardt et al. (2015) showed that the HELIOS E6 experiment is well suited for measuring the chemical composition of particles from carbon to neon. Here, we determined the quiet-time spectrum of carbon and oxygen in the energy range from

9 MeV nucleon^{-1} to above 80 MeV nucleon^{-1}. A good agreement between the HELIOS and the IMP measurements, as reported by Christian (1989), was found. In order to compute the radial gradient in the inner heliosphere, the data set was divided into a period when the spacecraft was within 0.45 AU ($I_{\rm close}$) and another period with distances greater than 0.9 AU ($I_{\rm far}$).

For GCR oxygen with energies between 30 and 80 MeV nucleon^{-1}, the ratio between the fluxes measured close to and far from the Sun is consistent with 1.0 ± 0.1, indicating no significant radial gradient. However, for ACR oxygen, a significant radial gradient of $G_{\rm r} = 73^{+26}_{-23}$%/AU and $G_{\rm r} = 25^{+29}_{-25}$%/AU was found for 9 to 13 and 13 to 28 MeV nucleon^{-1}. By assuming a spectral shape of $I(E) \propto E^1$ for the GCRs and subtracting this GCR contribution from the flux in the 13 to 28 MeV nucleon^{-1} range, the gradient increases to $G_{\rm r} = 40$%/AU. However, due to the uncertainties of this method a detailed error estimation is beyond the scope of this work.

When using the whole energy range from 9 to 28.5 MeV nucleon^{-1}, we find $G_{\rm r} = 48^{+12}_{-12}$%/AU. This energy range was used also by Webber et al. (1981) to determine the radial dependence of $G_{\rm r}$ beyond 1 AU. The radial gradient that we report here is about three times larger than the one determined between 1 and 10 AU by utilizing the Pioneer 10 measurements.

Comparing results from these Pioneer 10 measurements to HELIOS results, we find that the radial gradient of ACR oxygen significantly increases within the first 2 AU from the Sun. Evidently, ACR oxygen, with a rigidity much larger than GCR oxygen, may penetrate the heliosphere to come very close to the Sun, exhibiting in the process a very steep gradient. Future information to validate our results will come from the *Parker* Solar Probe.

Acknowledgements. The work was partly carried out within the framework of the bilateral BMBF-NRF-project "Astrohel" (01DG15009) as supported by the Bundesministerium für Bildung und Forschung (BMBF) and the South African National Research Foundation (NRF).

References

Christian, E. R. 1989, PhD thesis, California Institute of Technology, Pasadena
Cummings, C. A., Mewaldt, A. R., Stone, C. E., & Webber, R. W. 1990, Int. Cosmic Ray Conf., 6, 206
Cummings, A. C., Mewaldt, R. A., Blake, J. B., et al. 1995, Geophys. Res. Lett., 22, 341
Cummings, A. C., Tranquille, C., Marsden, R. G., Mewaldt, R. A., & Stone, E. C. 2009, Geophys. Res. Lett., 36, L18103
Decker, R. B., Krimigis, S. M., Roelof, E. C., et al. 2005, Science, 309, 2020
Drews, C., Berger, L., Taut, A., & Wimmer-Schweingruber, R. F. 2016, A&A, 588, A12
Fisk, L. A., Kozlovsky, B., & Ramaty, R. 1974, ApJ, 190, L35
Fox, N. J., Velli, M. C., Bale, S. D., et al. 2016, Space Sci. Rev., 204, 7
Garcia-Munoz, M., Mason, G. M., & Simpson, J. A. 1973, ApJ, 182, L81
Heber, B., Kopp, A., Fichtner, H., & Ferreira, S. E. S. 2005, Adv. Space Res., 35, 605
Hovestadt, D., Vollmer, O., Gloeckler, G., & Fan, C. Y. 1973, Int. Cosmic Ray Conf., 2, 1498
Klecker, B., McNab, M. C., Blake, J. B., et al. 1995, ApJ, 442, L69
Kunow, H. 1981, Cosmis ray experiment on board the solar probes Helios-1 and 2 (experiment no. 6), Tech. Rep.
Marquardt, J., Heber, B., Hörlöck, M., Kühl, P., & Wimmer-Schweingruber, R. F. 2015, J. Phys. Conf. Ser., 632, 012016
McDonald, F. B., & Ludwig, G. H. 1964, Phys. Rev. Lett., 13, 783
Moebius, E., Hovestadt, D., Klecker, B., Scholer, M., & Gloeckler, G. 1985, Nature, 318, 426
Moraal, H. 1993, Nucl. Phys. B Proc. Suppl., 33, 161
Parker, E. N. 1965, Planet. Space Sci., 13, 9
Pesses, M. E., Eichler, D., & Jokipii, J. R. 1981, ApJ, 246, L85
Potgieter, M. S. 2013, Liv. Rev. Sol. Phys., 10, 3
Strauss, R. D., & Potgieter, M. S. 2010, J. Geophys. Res. (Space Phys.), 115, A12111
Trattner, K. J., Marsden, R. G., Sanderson, T. R., et al. 1995, Geophys. Res. Lett., 22, 337
Trattner, K. J., Marsden, R. G., Bothmer, V., et al. 1996, A&A, 316, 519
Webber, W. R., McDonald, F. B., & Trainor, J. H. 1977, Int. Cosmic Ray Conf., 3, 233
Webber, W. R., McDonald, F. B., Trainor, J. H., & von Rosenvinge, T. T. 1979, Int. Cosmic Ray Conf., 5, 353
Webber, W. R., McDonald, F. B., von Rosenvinge, T. T., & Mewaldt, R. A. 1981, Int. Cosmic Ray Conf., 10, 92

6.2 PUBLICATION 3: ENERGY SPECTRA OF CARBON AND OXYGEN WITH HELIOS E6. RADIAL GRADIENTS OF ANOMALOUS COSMIC RAY OXYGEN WITHIN 1 AU

GCR particles typically have higher energies than ACR particles. Since high energy particles are less effected by solar modulation, the radial gradient of their flux is typically smaller than the gradient of the ACRs. For determining such a gradient usually of the magnitude of some percent, usually a reference spectrum is needed for the same time and conditions. However, as mentioned in the previous chapter, at most times there is no other spacecraft at the same conditions as HELIOS A or B. Thus, sufficient averaging is needed again to reduce location dependent and short timescale effects.

Since, however, there are also large timescale effects in the same order of magnitude as the radial effects, averaging too long will yield wrong results. In this publication an approach is shown for protons. The procedure to obtain the GCR spectra above 50 MeV is discussed as well.

The resulting spectrum is in very good agreement with the theoretically expected spectrum and could even be used to determine the modulation parameter Φ from the Force Field Solution (FFS), see Figure 30.

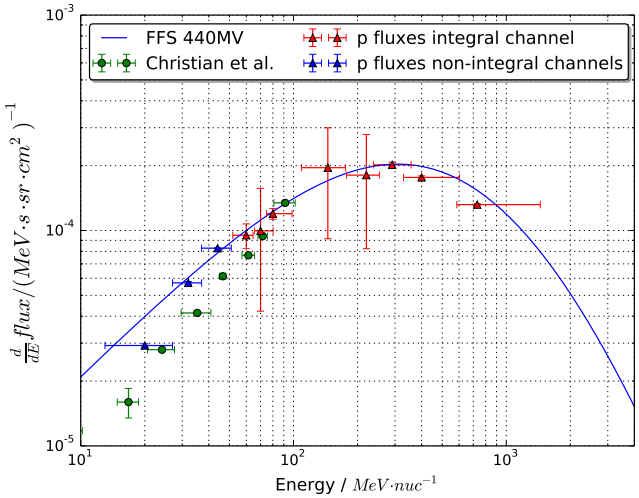

Figure 30: Blue and red symbols show the Helios proton fluxes from the energy channels for stopping and penetrating protons, respectively. The green symbols are the fluxes measured by IMP 8. The blue line shows the force field solution utilizing a modulation parameter Φ = 440 MV.[Marquardt and Heber, 2019]

A&A 625, A153 (2019)
https://doi.org/10.1051/0004-6361/201935413

Astronomy & Astrophysics

Galactic cosmic ray hydrogen spectra and radial gradients in the inner heliosphere measured by the HELIOS Experiment 6

J. Marquardt and B. Heber

Christian-Albrechts-Universität zu Kiel, Germany
e-mail: marquardt@physik.uni-kiel.de

Received 6 March 2019 / Accepted 24 April 2019

ABSTRACT

Context. The HELIOS solar observation probes provide unique data regarding their orbit and operation time. One of the onboard instruments, the Experiment 6 (E6), is capable of measuring ions from 4 to several hundred MeV nucleon^{-1}.
Aims. In this paper we aim to demonstrate the relevance of the E6 data for the calculation of galactic cosmic ray (GCR), anomalous cosmic ray (ACR), and solar energetic particle (SEP) fluxes for different distances from the sun and time periods.
Methods. Several corrections have been applied to the raw data: determination of the Quenching factor of the scintillator, correction of the temperature dependent electronics, degradation of the scintillator as well as the effects on the edge of semi-conductor detectors.
Results. Fluxes measured by the E6 are in accordance with the force field solution for the GCR and match models of the anomalous cosmic ray propagation. GCR radial gradients in the inner heliosphere show a different behaviour than in the outer heliosphere.

Key words. Sun: heliosphere – solar-terrestrial relations – cosmic rays

1. Introduction

In October 2011, the European Space Agency (ESA) announced the selection of Solar Orbiter as one of the Cosmic Vision M missions, with the launch envisioned for 2019/2020. On August 12, 2018 the National Aeronautics and Space Administration (NASA) Parker Solar Probe was launched and reached its first perihelion on November 9, 2018. Thus, we have again spacecraft that determine in-situ the properties and dynamics of plasma, fields, and particles in the inner heliosphere. Ng et al. (2016) showed recently a solar cycle variation of 1–10 GeV γ-rays measured by the *Fermi* satellite, which is caused by galactic cosmic ray (GCR) particles interacting with the solar atmosphere. In order to investigate such temporal evolution it is worthwhile revisiting the energetic particle measurements by the HELIOS Experiment 6 (E6) performed in the 1970s within 0.4 AU in the light of advanced analysis and modelling techniques.

It has been recently shown that the E6 instrument is capable of measuring the distribution of anomalous cosmic ray (ACR), and GCR ions from carbon ($z = 6$) to silicon ($z = 14$) in the energy range from a few megaelectron-volt (MeV) nucleon^{-1} to several tens of MeV nucleon^{-1} in the inner heliosphere during solar minimum (Marquardt et al. 2018), resulting in the first measurement of the radial gradient of anomalous oxygen within the Earth orbit. Bialk (1996) and Droege (1999) showed that the energy range of the instrument can be extended to above several 100 MeV nucleon^{-1}, allowing us to determine the energy spectra and the radial gradient of GCRs' hydrogen in the inner heliosphere from 0.3 to 1 AU.

GCRs encounter a turbulent solar wind with the embedded heliospheric magnetic field (HMF) when entering the heliosphere. This leads to significant global and temporal variations in their intensity and in their energy as a function of position inside the heliosphere. This process is identified as the solar modulation of GCRs (see for example Potgieter 2013, and references therein). The analysis of the radial gradient of ACR oxygen in the inner heliosphere within 0.5 AU by Marquardt et al. (2018) shows the need to improve particle transport models towards the Sun.

In what follows we show that the measurement capabilities of HELIOS E6 allow us to determine the hydrogen spectra up to above 800 MeV nucleon^{-1}. Figure 1 from Christian (1989) displays the quiet-time energy spectra for H, He, C, N, and O taken during quiet times from 1974 to 1978 1 AU by Interplanetary Monitoring Platform (IMP) 8. We validate our results against the GCR hydrogen measurements shown there. The accuracy of the instrument allows us to give upper limits of the radial gradient that are consistent with the ones reported by McDonald et al. (1977) and Webber et al. (1981) between 1 and 4.5 AU.

2. Instrumentation

HELIOS A and HELIOS B were launched on December 10, 1974 and January 15, 1976, respectively. The two almost identical spinning space probes were sent into ecliptic orbits around the Sun. The orbital period around the Sun was 190 days for HELIOS A and 185 days for HELIOS B, and their perihelia were 0.3095 AU and 0.290 AU, respectively.

A sketch of the E6 sensor is shown in Fig. 2. It consists of a stack of five silicon semiconductor detectors (SSD; D1 to D5) and one Sapphire Cherenkov detector surrounded by a plastic anti-coincidence detector. The five SSDs function as a "standard" $\mathrm{d}E/\mathrm{d}x - E$ telescope (Brunstein 1964) with the Cherenkov detector used as anti-coincidence (see for example Marquardt et al. 2018, and references therein) allowing us to measure hydrogen to silicon energy spectra in the energy range from a few to several tenths of MeV nucleon^{-1}. This method is based on at least two energy deposits, one in a thin detector transmitting ($\mathrm{d}E/\mathrm{d}x$) and another one in a thick detector

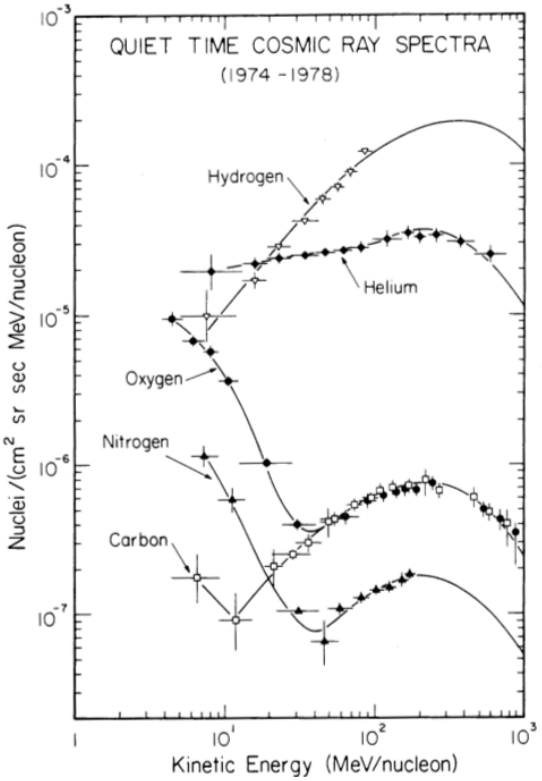

Fig. 1. Quiet-time H, He, C, N, and O energy spectra measured at 1 AU over the period from 1974 to 1978. The ACR component is reflected in the spectra by an enhancement at low energies for He, N, and O (Fig. 1.2 of Christian 1989). The GCR component dominates at energies above 30 MeV nucleon^{-1} for N and O and 50 MeV nucleon^{-1} for He, respectively.

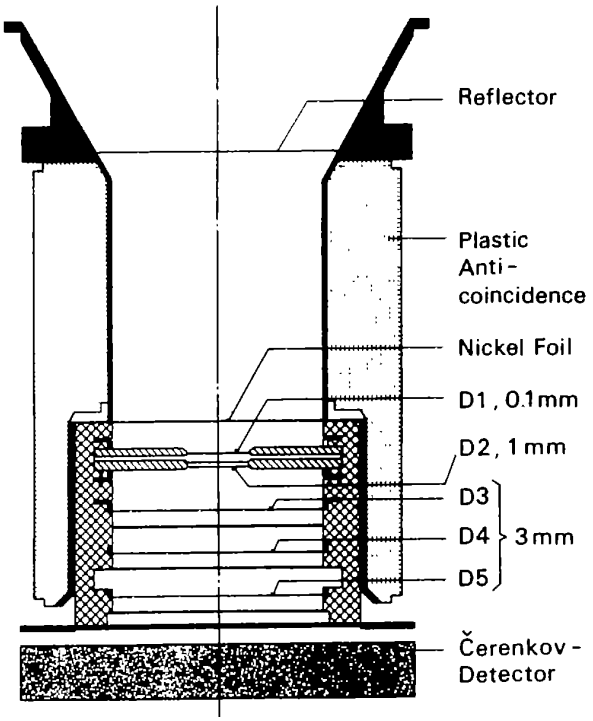

Fig. 2. Schematic of the E6 detector setup.

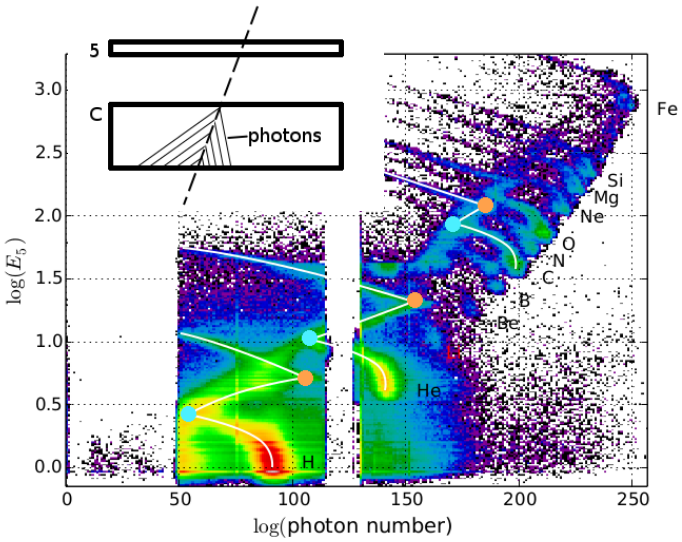

Fig. 3. Integral channel of the HELIOS E6. The orange point marks the penetration of the Cherenkov (C) detector, the blue point marks the exceeding of light speed inside the medium resulting in the particles emitting Cherenkov-Radiation.

stopping the incident particle (E) (more details can be found in Marquardt et al. 2015, and references therein). At energies above ~50 MeV protons trigger the sapphire Cherenkov detector. In order to increase the geometric factor, both detectors D1 and D2 are not required for a valid coincidence. These integral channels are called P51 for protons and A48 for heavier ions and the identification of ions is based on the $\mathrm{d}E/\mathrm{d}x - \mathrm{d}E/\mathrm{d}x$ and $\mathrm{d}E/\mathrm{d}x - C$ method (Kühl et al. 2016; Linsley 1955).

The $\mathrm{d}E/\mathrm{d}x - \mathrm{d}E/\mathrm{d}x$ method is based on the energy loss in two detectors allowing us to identify different particle species in certain energy ranges. However, this method has two major disadvantages, which are (1) some areas of the two dimensional energy loss plane are populated by different elements and (2) the signal from particles that penetrate the instrument from the back cannot no longer be distinguished from the ones that penetrate the instrument from the front. By adding a Cherenkov detector the overlap of different species can be minimized and one can discriminate against backward penetrating particles. This so called $\mathrm{d}E/\mathrm{d}x - C$-method (Linsley 1955) is applied to charged particles that completely penetrate a semi-conductor detector 5 and a Cherenkov detector C, which is placed underneath (see inset in Fig. 3). If they penetrate C faster in the dielectric material than light can propagate, they produce a measurable light flash (Cherenkov radiation). The threshold speed of $v > c/n$ depends on the refractive index n of the material. Plotting the energy-loss by ionization, ΔE in A, as a function of the Cherenkov detector signal results in characteristic curves, clearly separated for different atomic numbers, with their slopes depending on particle speed. Thus, the method allows an identification of the penetrating particles and a determination of their energy above a threshold speed. Figure 3 shows measurements by Helios E6, where the Cherenkov detector is made of sapphire, which is also a scintillator responding to the ionization energy loss of the particle in the detector. The different ion tracks are identified in the figure and the orange and blue circles mark those points along the track where the particles penetrate the sapphire and where the Cherenkov light production starts, respectively. Thus, the $\mathrm{d}E/dx - dE/\mathrm{d}x$ method is used along the tracks starting at the orange point and ending at the blue point, and the $\mathrm{d}E/\mathrm{d}x - C$ method after the blue point. As is evident from Fig. 3, charged particle measurements can suffer from various

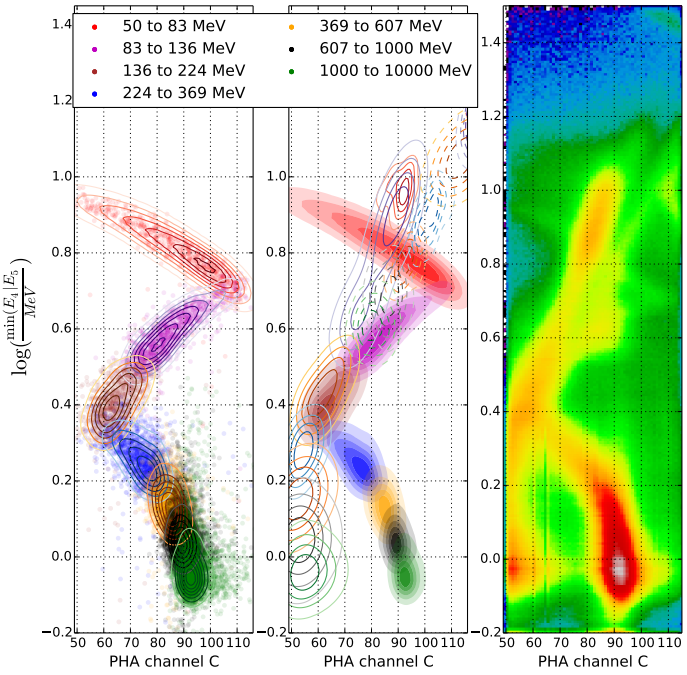

Fig. 4. Simulated protons in the integral channel. We colour-coded the different input energy ranges for the simulation; they are logarithmic equidistant except for the last integral bin. The lines on the middle panel are for backwards protons and the dashed lines for backwards He. On the *right panel*, real measurements are shown for comparison. All energies are in MeV nucleon^{-1}.

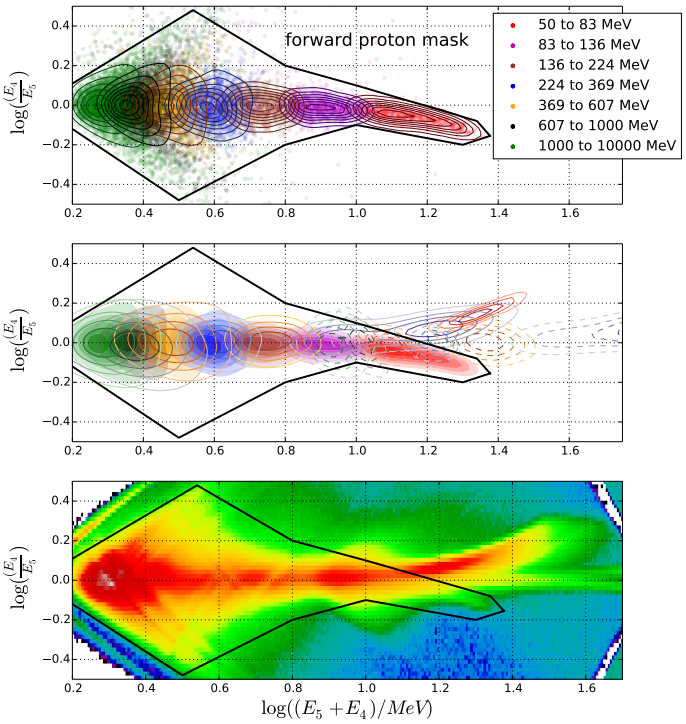

Fig. 5. Simulated protons in the integral channel. We colour-coded the different input energy ranges for the simulation; they are logarithmic equidistant except for the last integral bin. The lines on the *middle panel* are for backwards protons and the dashed lines for backwards He. On the *lowest panel* real measurements are shown for comparison. All energies are in MeV nucleon^{-1}.

imperfections. Therefore, modelling of the physical processes and of the instrument geometry, as well as the environment, is essential to understand such measurements (e.g. Heber et al. 2005; Kühl et al. 2015; Marquardt et al. 2015).

3. Experiment 6 modelling

In order to understand the Helios E6 response to penetrating ions, a GEometry And Tracking (GEANT) 4 simulation (Agostinelli et al. 2003) has been setup that has to include optical photon tracking as well as Birk's quenching (Birks 1951) in the sapphire detector, as discussed in what follows.

While usual anorganic scintillation counters reach a typical scintillation yield of one photon per 100 eV deposited energy, the sapphire Cherenkov detector scintillates with an efficiency of one photon per 50 keV deposited energy. The reason for this is the self-absorption of the emitted light inside the scintillator and the emitted photons being of higher energy than the photon energy at which the photo-multiplier reaches peak efficiency. In common anorganic scintillators those effects are bypassed by doping the base material. Due to the low scintillation efficiency of the detector, the light output from scintillation falls in the same order of magnitude as the light output from Cherenkov radiation. Otherwise it wouldn't be possible to measure the Cherenkov effect and scintillation light with the same detector. The sum of the emitted photons can be seen in Fig. 3. Cherenkov radiation is emitted as soon as particles have a higher speed than light in the medium; in the case of the sapphire $v_n = V_0/n = 0.566 \cdot c$ with $n = 1.77$ has been used. Cherenkov radiation is always emitted anisotropically while scintillated photons are isotropic.

In Fig. 3 it is also noticeable that neither the orange nor the blue points align. This is due to quenching (Birks 1951). The higher the energy deposit per path length, $\frac{\mathrm{d}E}{\mathrm{d}x}$, the lower the number of photons per energy deposit. Furthermore, the upper side of the detector C has been blackened to avoid the reflection of light. For speeds much larger than v_n the light output is dominated by Cherenkov light that reflects the direction of the incoming particles. Thus, Cherenkov light from particles entering the detector from behind gets absorbed, while photons from the scintillation process are still counted. This leads to a separation of forward and backward penetrating particle tracks in Fig. 3. However, particles with speed $v < v_n$ lead to a photon distribution that is isotropic resulting in insufficient discrimination between forward and backward particles below $0.566 \cdot c$. In order to improve the rejection of backwards penetrating ions, we calculated the expected distributions for forward and backward penetrating protons as well as the ones for backward penetrating helium in Figs. 4 and 5. In all our simulations, quenching in the sapphire detector has been taken into account, by using Birk's formula

$$\frac{\mathrm{d}L}{\mathrm{d}x} = S \frac{\frac{\mathrm{d}E}{\mathrm{d}x}}{1 + k_\mathrm{B} \frac{\mathrm{d}E}{\mathrm{d}x}}, \tag{1}$$

using as parameter $S = \frac{20}{MeV}$ and $k_\mathrm{B} = 50 \cdot 10^{-6} \frac{\mathrm{mm}}{\mathrm{MeV}}$.

Taking the above-mentioned effects into account, we performed a simulation with one Billion protons in the energy range from 40 MeV nucleon^{-1} up to 10 GeV nucleon^{-1} impinging isotropically on the E6 sensor. Results for protons that cross the sensor from the front are summarized in the left panel of Fig. 4 and in the top panel of Fig. 5. The first of the two figures displays the minimum logarithmic energy loss ΔE in SSD 4 and SSD 5 as a function of the light output of the Cherenkov detector C in six different energy bands from 50–83 MeV nucleon^{-1}

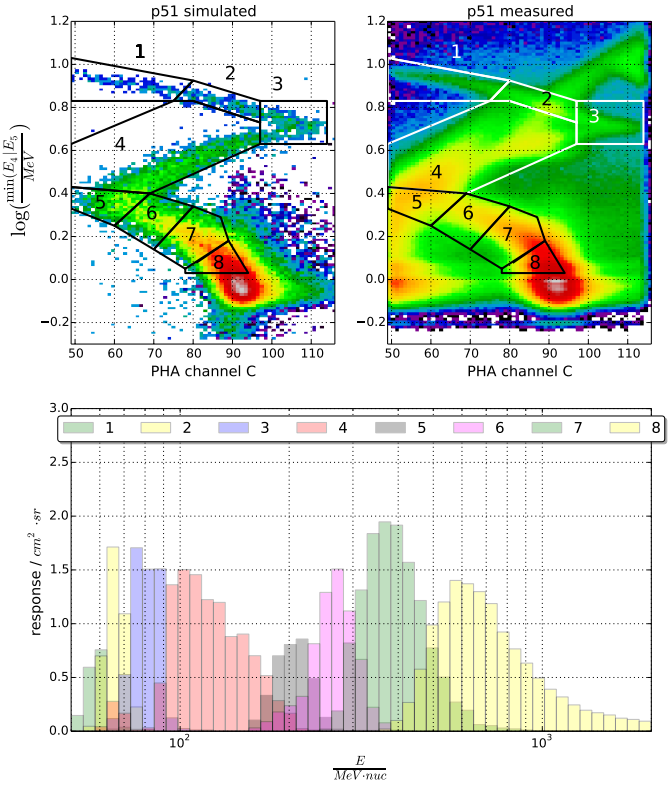

Fig. 6. Simulated protons on the *left* and corrected measured protons on the *right* in the integral channel. *Bottom*: responses for the boxes shown in upper panels.

(red contour lines) to 607–1000 MeV nucleon^{-1} (black countour lines). The width of these channels is chosen so that they are spaced equally in the logarithm of the energy boundaries. An integral channel from 1000 to 10 000 MeV is shown by the green contour lines. We note that $min(\Delta E_4, \Delta E_5)$ results in a sharper pattern since it minimizes the stochastic nature of the energy deposition (see also Kühl et al. 2015). The right panel of Fig. 4 displays the corresponding quiet-time measurements obtained from December 1974 to July 1977. By comparing both panels with each other, we find that the calculated track reflects significant features in the measurements as there are the position of the turning points when crossing the detector and the onset of the Cherenkov effect. However, we find some significant features that must be caused by backward penetrating helium and protons. In order to make use of all the information available to us, the upper panel of Fig. 5 displays the position of the energy intervals in the difference of the logarithmic energy losses in SSD 5 and SSD 4 versus the sum of the logarithmic energy losses in SSD 4 and SSD 5 matrix. Although the energy losses converge above a certain energy (here above ~83 MeV), differences are found for lower energies. The computed distribution can therefore be used to define a mask with all valid entries for forward penetrating protons. The middle panels of both figures display in addition the distribution for protons and helium penetrating the instrument from the back indicated by the solid and dashed contour lines, respectively. The different colours of the contour lines give the incoming energy range of the backward penetrating particles in MeV nucleon^{-1}. Comparing the middle panel and the right panel of Fig. 4 and the middle and the lower panel of Fig. 5, all simulated features are seen in the in-flight matrix indicating that the simulation reflects the measurements very well. From both figures one notes that the contour lines for backward penetrating protons below 83 MeV are well outside the mask (Fig. 5) and the forward penetrating proton track in Fig. 4. A significant reduction can even be obtained up to 136 MeV protons (cyan contour lines). In the energy range from 136 to 230 MeV backward penetrating and forward penetrating protons cannot be distinguished. Above 230 MeV the Cherenkov effect sets in and the tracks in Fig. 4 separate again. The dashed contour lines in the middle panel of both figures show the distributions for backward penetrating helium. The mask defined in Fig. 5 rejects backward penetrating helium with energies lower than ~350 MeV nucleon^{-1} (blue dashed contour lines). At energies above this threshold forward penetrating protons and helium cannot be distinguished. In Fig. 6 (right panel) we applied our mask to the in-flight measurements in $\min\left(\frac{dE}{dx}_{SSD5}, \frac{dE}{dx}_{SSD4}\right) - C$ distribution. Although we retrieve a significant reduction of the contribution of backward penetrating particles, we are left with areas that cannot be cleaned. To obtain energy spectra we defined eight boxes as shown in the upper left and right panel in Fig. 6 for the simulated and measured matrix, respectively. The boxes were defined as a compromise between equal logarithmic energy spacing and splitting the different particle populations. Boxes 1 and 3 were chosen to completely avoid contamination from backward penetrating particles. Box 2 only contains backward penetrating helium. Box 4 was chosen to contain the parts of the spectra in which separation of forwards and backwards protons as well as backwards helium are impossible to distinguish from one another. Box 5 is free of helium and the energy of forwards and backwards protons is roughly the same, allowing for easier statistical separation. Boxes 6 and 7 are again free of contamination and spaced equally. Box 8 has a sharp cut-off to avoid electrons and near relativistic protons from entering the box. We note that electrons play a very minor role as they will be always minimally ionizing and at near-light speed and are thus below and to the right of box 8. The lower panel displays the computed forward penetrating proton response functions $R_\alpha^{i=p}(E)$ as a function of the kinetic energy E for each box ranging from about 50 MeV to above 2 GeV. Following Sullivan (1971) the measured count rate C_i for each channel is given by

$$C_i = \sum_{\alpha=1}^{n} \int_0^\infty R^i{}_\alpha(E) J_\alpha(E) \mathrm{d}E, \tag{2}$$

with $\sum_\alpha$ being the sum over all particles species contributing to each channel C_i, and $J_\alpha(E)$ being the energy spectrum for each particle species. The total contribution is then given by the integral over all possible energies. For an ideal detector, that is a detector that is only sensitive to one particle type with a response function that is constant R_i in the energy range from E_l to E_u and otherwise zero:

$$R(E) = \begin{cases} 0 & \text{for } 0 < E < E_l \\ R_i & \text{for } E_l \le E \le E_U \\ 0 & \text{for } E > E_u \end{cases} . \tag{3}$$

In that case, Eq. (2) reduces to

$$C_i = R_i \cdot (E_u - E_l) \cdot I(\langle E \rangle), \tag{4}$$

where $\langle E \rangle$ is the mean energy of channel i and $J_i(\langle E \rangle)$ can be easily computed by

$$I(\langle E \rangle) = \frac{C_i}{R_i \cdot (E_u - E_l)}.$$

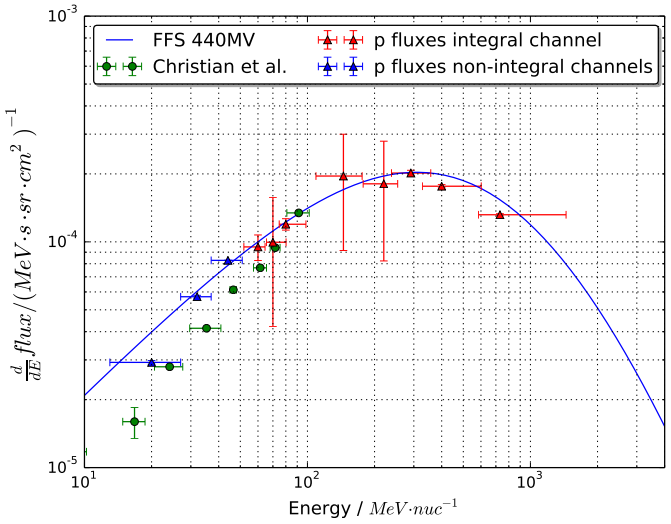

Fig. 7. Blue and red symbols show the Helios proton fluxes from the energy channels for stopping and penetrating protons, respectively. The green symbols are the fluxes measured by IMP 8 taken from Fig. 1. The blue line shows the force field solution utilizing a modulation parameter $\Phi = 440$ MV. Details can be found in the text.

Although the response function for each box is deviating from the ideal ones described by Eq. (3), we approximate $R \cdot (E_u - E_l)$ by the integral of the response function $\int_{E_l}^{E_u} R_i(E)\,\mathrm{d}E$ and $\langle E \rangle$ is the energy E for which the response function has a maximum. The results are visualized in Fig. 7. In this figure we added three channels for stopping protons to extend the energy range down to about 10 MeV (see Marquardt et al. 2018, and references therein). While the y errors account for statistical errors only, the x errors mark the energies when the response has been decreased to $\frac{1}{6}$ of the maximum response of each box. This simple method has been chosen since it shows in an intuitive way the results applicable to a response function that has a box or a gaussian shape, respectively. For comparison the green symbols display the hydrogen measurements from Fig. 1. Taking into account the different measurement times from 1974 to 1978 for IMP 8 and from the end of 1974–1977 for Helios A, the agreement between both data sets is remarkably good. Taking these uncertainties into account, our analysis shows that the E6 can be utilized to determine proton energy spectra in the range from 10–50 MeV from energy channels of stopping particles and from 60 to about 600 MeV for penetrating particles.

During quiet times the energy spectra of protons can be approximated by the force field solution (FFS, see Gleeson & Axford 1968; Caballero-Lopez & Moraal 2004, and references therein). As local interstellar spectrum (LIS) we used the one given by Burger et al. (2000),

$$J_i(\Phi) = J_{\mathrm{LIS},i}(T + \Phi)\frac{T + 2E_{0,i}}{(T + \Phi)(T + \Phi + 2E_{0,i})}, \tag{5}$$

where $\Phi = (\mathrm{Ze}/A)\phi$ is the modulation function and ϕ is the modulation parameter. Rewriting Eq. (2) we can minimize the norm

$$\left\| \sum_{i=1}^{8} \left(C_i - \sum_{\alpha=1}^{n} \int_0^{\infty} R^i{}_{\alpha}(E) J^{\phi}_{1\,\mathrm{AU}}(E)\,\mathrm{d}E \right) \right\| \tag{6}$$

in order to obtain the modulation parameter that fits the Helios E6 measurements best. Figure 8 (left panel) shows the norm as a function of the modulation parameter ϕ showing a minimum at $\phi = 440$ MV. Using data from the neutron monitor network Usoskin et al. (2005) and Gieseler et al. (2017) computed Bartels rotation averaged modulation parameters from 1951 to 2004 using the LIS from Burger et al. (2000). From 1974 to the end of 1978 and from the launch of Helios A in December 1974 and the end of 1977, ϕ varies from $\phi_{\mathrm{min}} = 404$ to $\phi_{\mathrm{max}} = 670$ and from $\phi_{\mathrm{min}} = 404$ to $\phi_{\mathrm{max}} = 494$, respectively. The mean values are $\langle\phi\rangle = 474 \pm 28$ and $\langle\phi\rangle = 435 \pm 23$, respectively. The latter value compares well with the one found in our analysis. The right panel visualizes the distribution of the total measured count rates in comparison to the calculated ones. Since the response of box 8 never reached 0 (see Fig. 6) we estimate the contribution from protons above 10 GeV by assuming that the response function is constant between 10 and 100 GeV. This extra contribution is shown by the green box on top of the blue one in Fig. 8. Thus we conclude that protons above 10 GeV play a very minor role.

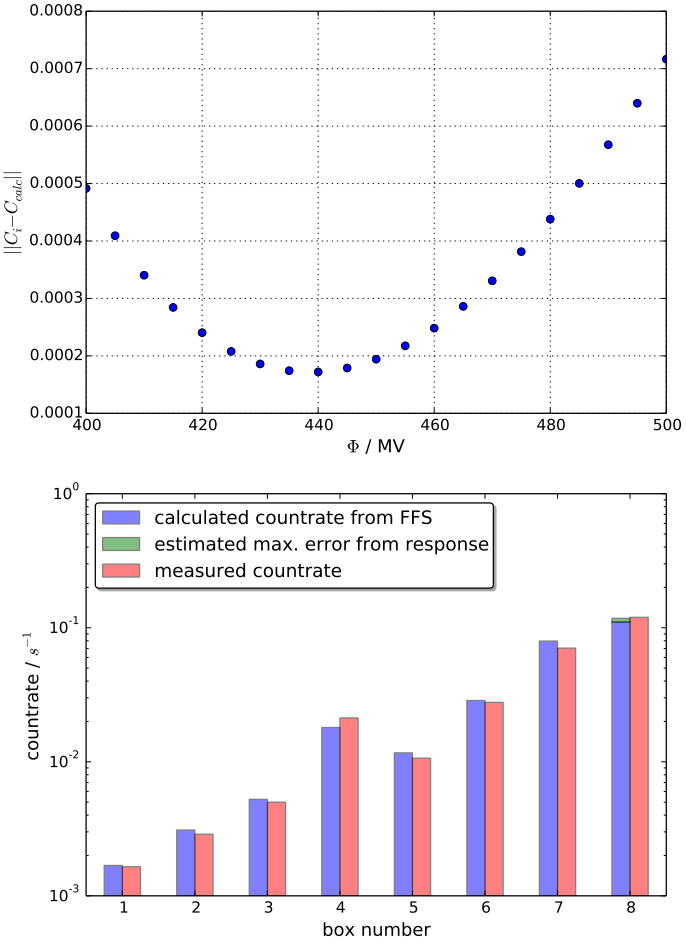

Fig. 8. *Upper panel*: norm of the difference between calculated and measured count rates as a function of the modulation parameter ϕ. *Lower panel*: proton count rates measured and calculated from FFS seen in Fig. 7.

4. Radial gradients

Another important open question is how cosmic rays are transported towards the Sun in the inner heliosphere. Marquardt et al. (2018) showed that anomalous cosmic ray oxygen penetrates deeper into the inner heliosphere as predicted by computations. Strauss & Potgieter (2010) and recently Ng et al. (2016) found

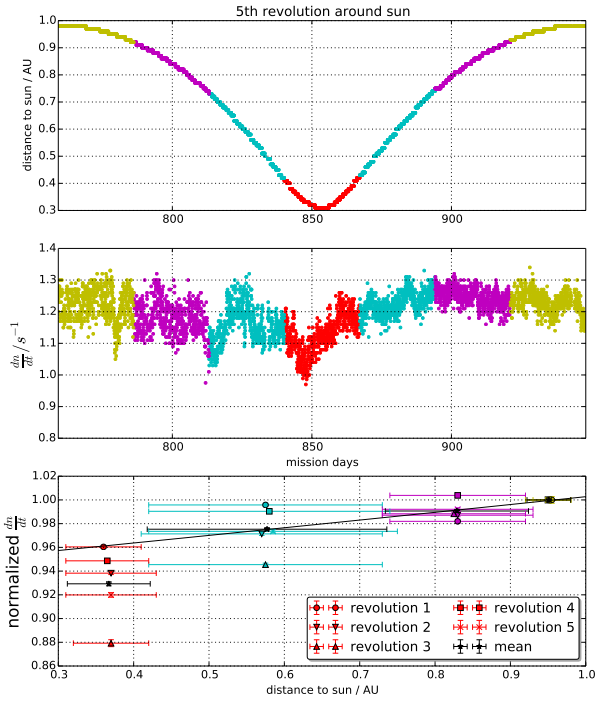

Fig. 9. *Top panel*: radial distance to sun versus time. We colour-coded the length of one Bartels rotation centred around the closest point to sun. *Middle panel*: corresponding count rates. *Lowest panel*: averaged count rates for different revolutions versus the distance.

solar cycle variation in the 1–10 GeV γ-rays measured by the *Fermi* satellite in the vicinity of the Sun. Thus in contrast to our current understanding, cosmic rays penetrate deeply into the Sun's corona. In order to advance our understanding, it is important to know the radial variation of the GCR flux within 1 AU. With the improved data analysis of the E6 experiment, we investigate in what follows the radial gradient of galactic cosmic ray protons in the energy range from about 250 to about 700 MeV, combining boxes 6–8. We investigate the radial variation using a two-step approach. Since the flux obtained in this channel results from the product of the integral channel and the number of entries in boxes 6–8, we first determine the radial variation in the integral channel and then the one in the box channel. The integral channel is the channel that measures forward and backward penetrating protons and electrons and backward penetrating helium above 50 MeV nucleon^{-1} for ions and above 10 MeV for electrons. Figure 9 displays in the top and middle panels the radial distance to the Sun and the count rate in the integral proton channel for the fifth orbit of Helios 1 from December 30, 1976 (mission day 750) to July 18, 1977 (mission Day 950). Marked by different colours are Bartels rotation averages centred around the closest approach, allowing us to determine the radial dependence of this count rate. In the lowest panel, the mean of the Bartels average of the count rates prior and after closest approach are displayed as a function of radial distances for all orbits, which occurred during quiet times from launch of the satellite to July 18, 1977. In order to compare the different orbits to each other all count rates are normalized to the ones observed between 0.9 and 1 AU. Although we find a wide spread, a clear trend of decreasing flux with radial distance is obtained. In order to minimize the influence of temporal variations we average the normalized values for all five orbits. They are shown in Fig. 9 by the black bullets. By fitting a line to the logarithms of the three outer bins we obtain a radial gradient of 6.6 ± 4% AU^{-1}.

Table 1. Selected radial gradients obtained in the heliosphere by McDonald et al. (1977), Webber et al. (1981), Bialk (1996), and this study.

Distance range (AU)	G_r (% AU^{-1})	Energy (MeV)
From McDonald et al. (1977)		
1.25–4.2	4.1 ± 3.7	210–275
1.25–4.2	2 ± 4	275–380
1.25–4.2	1.3 ± 5	380–460
1–3.8	0 ± 4	210–275
1–3.8	2.5 ± 4	275–380
1–3.8	3.8 ± 5	380–460
From Webber & Lockwood (1981)		
2–28	2.5 ± 0.5	>60
This study		
0.4–1	6.6 ± 4	>50
0.3–1	2 ± 2.5	250–700

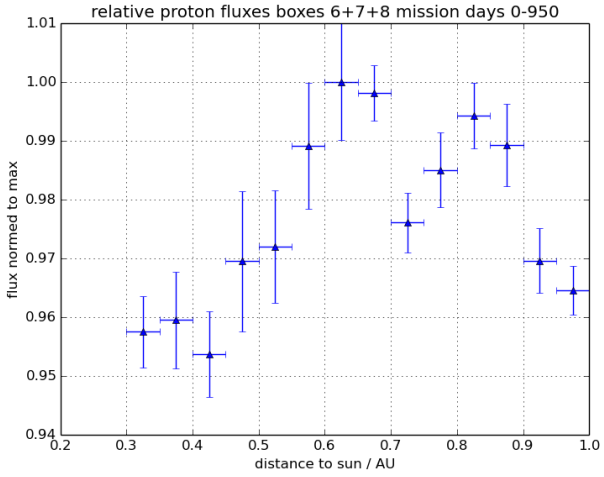

Fig. 10. Flux in the energy range from 250 to 700 MeV as a function of radial distance using a bin width of 0.05 AU. The values have been normalized to the maximum value at a distance of 0.6 AU. Details can be found in the text.

This value is consistent with the one obtained by Bialk (1996) but larger than the ones published by McDonald et al. (1977) and Webber & Lockwood (1981) summarized in Table 1. We note that the flux at 0.35 AU is much lower than the expected one from our fit. This is in agreement with the observation of the radial gradient of anomalous oxygen increasing in the inner heliosphere (Marquardt et al. 2018).

In the second step we used the same approach as for the integral channel for the differential proton channel sensitive to protons between 250 and ~700 MeV. Here we binned the data so that we get a radial resolution of 0.05 AU per bin as displayed in Fig. 10. The values have been normalized to the maximum value at a distance of about 0.6 AU. We note that transient and recurrent Forbush Decreases (Richardson 2004; Richardson & Cane 2011), which are short term flux decreases in the cosmic ray flux, lead to larger variation (error) than the statistical ones. However, Fig. 10 shows no clear overall trend. In order to estimate the radial gradient we need to minimize the influence of temporal effects. Therefore we divided the data set into measurements close to the Sun (0.3–0.6 AU) and far away from the Sun (0.7–1 AU), respectively. Our analysis leads to a radial

gradient of $G_R = 2 \pm 2.5\%\,\mathrm{AU}^{-1}$ that is in good agreement with the one published by McDonald et al. (1977), Bialk (1996), and Webber et al. (1981). Because of the limited E6 capabilities the uncertainties in the differential flux measurements do not indicate any increase of the radial gradient towards the Sun. Although the count rate profile of the integral channel as well as the anomalous oxygen indicate an increase of the radial gradient within 0.5 AU, only the measurements from the Parker Solar Probe will validate or disprove the Helios observations presented here.

5. Summary and conclusions

The Experiment 6 (E6) aboard the Helios space probes was designed to measure ions and electrons in the energy range from a few MeV nucleon^{-1} to above 50 MeV nucleon^{-1} and 0.15 and above 10 MeV for electrons. In order to compute the proton energy spectrum above 50 MeV nucleon^{-1}, the instrument utilizes the $\frac{dE}{dx} - C$ method. A sophisticated model of the instrument has been developed on the basis of the GEometry And Tracking (GEANT)-4 package. We computed the response of the instrument not only to forward penetrating protons but also to hydrogen and helium that penetrate the sensor from behind. In order to reduce the background to these unwanted contributions, the energy loss distributions in the two silicon detectors have been evaluated. By adding a simple mask the background of backward protons below 130 MeV could be reduced significantly. For energies between 130 and 250 MeV, backward and forward penetrating protons cannot be distinguished from the signal of the last three detectors. At higher energies from above 250 MeV the Cherenkov effect sets in and forward and backward penetrating particle tracks separate again (see Fig. 5). Applying the "background" rejection derived from simulations an energy response (lower panel in Fig. 6) for different masks shown in the upper two panels of Fig. 6 were computed. These response functions were used to compute the GCR spectrum during quiet times from December 1974 to July 1977. The flux in each mask (box) was determined by applying a simple inversion. Taking into account the different measurement periods used in the study by Christian (1989) and our analysis, the spectra derived from Helios and IMP 8 measurements agree very well with each other. Our analysis resulted in $\phi = 440$ MV, which is in very good agreement with mean $\phi = 435$ MV derived from the values published by Usoskin et al. (2005). Thus we conclude that Helios E6 can be used to determine the proton spectra up to above 600 MeV. However, not only the intensity close to Earth can be determined but also the radial gradient within 1 AU. In contrast to Webber & Lockwood (1981) who determined a radial gradient of $2.5 \pm 0.5\%\,\mathrm{AU}^{-1}$ between 2 and 28 AU, we found a radial gradient of $6.6 \pm 4\%\,\mathrm{AU}^{-1}$ between 0.3 and 1 AU for above 50 MeV protons. Our analysis indicates an increasing radial gradient within 0.5 AU. The analysis from Bialk (1996) using an integral channel with energies above 135 MeV results in somewhat lower gradients. This trend is continued when we determine the radial gradient for protons in the energy range between 250 and 600 MeV protons to $2 \pm 2.5\%\,\mathrm{AU}^{-1}$, which is in good agreement with the values found by McDonald et al. (1977) obtained between about 1 to about 4 AU. The Parker Solar Probe has explored the inner heliosphere on its first orbit during the same magnetic polarity of the Sun as in the 1970s and during solar minimum conditions. Therefore the results from the Parker Solar Probe will enable us to find out the following information: (1) whether the radial gradient during the current solar cycle is consistent with the one obtained in the 1970s between 0.5 and 1 AU; (2) whether the radial gradient increases with decreasing distance to the Sun within 1 AU; and (3) in the event that the Parker Solar Probe results confirm the HELIOS results, we can ascertain the implications for cosmic ray propagation models.

References

Agostinelli, S., Allison, J., Amako, K., et al. 2003, Nucl. Instrum. Methods Phys. Res. Sect. A, 506, 250
Bialk, M. 1996, PhD Thesis, Christian-Albrechts-Universität zu Kiel
Birks, J. B. 1951, Proc. Phys. Soc. Sect. A, 64, 874
Brunstein, K. A. 1964, Phys. Rev., 133, 1520
Burger, R. A., Potgieter, M. S., & Heber, B. 2000, J. Geophys. Res., 105, 27447
Caballero-Lopez, R. A., & Moraal, H. 2004, J. Geophys. Res. (Space Phys.), 109, A01101
Christian, E. R. 1989, PhD Thesis, California Institute of Technology, Pasadena
Droege, W. 1999, Proceedings of the 26th International Cosmic Ray Conference, August 17–25, 232
Gieseler, J., Heber, B., & Herbst, K. 2017, J. Geophys. Res. (Space Phys.), 122, 10
Gleeson, L. J., & Axford, W. I. 1968, ApJ, 154, 1011
Heber, B., Kopp, A., Fichtner, H., & Ferreira, S. E. S. 2005, AdSpR, 35, 605
Kühl, P., Banjac, S., Dresing, N., et al. 2015, A&A, 576, A120
Kühl, P., Gómez-Herrero, R., & Heber, B. 2016, Sol. Phys., 291, 965
Linsley, J. 1955, Phys. Rev., 97, 1292
Marquardt, J., Heber, B., Hörlöck, M., Kühl, P., & Wimmer-Schweingruber, R. F. 2015, J. Phys. Conf. Ser., 632, 012016
Marquardt, J., Heber, B., Potgieter, M. S., & Strauss, R. D. 2018, A&A, 610, A42
McDonald, F. B., Lal, N., Trainor, J. H., Van Hollebeke, M. A. I., & Webber, W. R. 1977, ApJ, 216, 930
Ng, K. C. Y., Beacom, J. F., Peter, A. H. G., & Rott, C. 2016, Phys. Rev. D, 94, 023004
Potgieter, M. S. 2013, Liv. Rev. Sol. Phys., 10, 3
Richardson, I. G. 2004, Space Sci. Rev., 111, 267
Richardson, I. G., & Cane, H. V. 2011, Sol. Phys., 270, 609
Strauss, R. D., & Potgieter, M. S. 2010, J. Geophys. Res. (Space Phys.), 115, A12111
Sullivan, J. D. 1971, Nucl. Instrum. Methods, 95, 5
Usoskin, I. G., Alanko-Huotari, K., Kovaltsov, G. A., & Mursula, K. 2005, J. Geophys. Res. (Space Phys.), 110, A12108
Webber, W. R., & Lockwood, J. A. 1981, J. Geophys. Res., 86, 11458
Webber, W. R., McDonald, F. B., von Rosenvinge, T. T., & Mewaldt, R. A. 1981, Int. Cosmic Ray Conf., 10, 92

6.2.1 *Supplemental material: Event analysis*

The technique for analysing high energy proton spectra introduced in publication 3 (section 6.2) can also be applied to solar events. In this example, the event from 22.11.1977 will be shown.

The event has been registered by HELIOS A and B as well as IMP-8 at earth, making this a relatively widespread event. The positions of the three spacecrafts are shown in Figure 31.

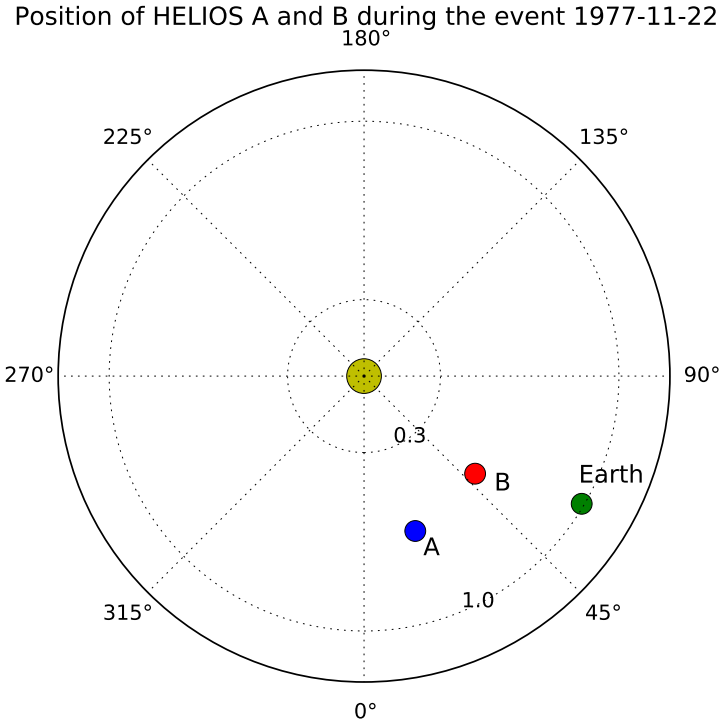

Figure 31: Positions of Earth (IMP-8), HELIOS A and HELIOS B during the event from 22.11.1977.

For the event analysis the number of boxes has been increased by one. Also, not all of the boxes have been used, but instead only the boxes without contribution from backwards particles have been used. The correction of the other boxes 2,4 and 5 is only possible with exact knowledge of the backwards flux. This condition is not met during events since the fluxes are not isotropic and highly time dependent.

An other box numbered 9 has been added in the high energy and β range. Figure 32 shows this box together with all the other boxes from Publication 3 (section 6.2). Also shown are electron contributions above 10 MeV in the boxes. It is evident that box 9 is highly contaminated by electrons but it is virtually impossible to get a clean measurement of the very high energy proton contribution.

The Ground Level Enhancement (GLE) from 22.11.1977 was observed by multiple spacecrafts, including IMP-8, HELIOS A and HELIOS B. The lower energy range spectra have already been analysed by [Droege, 1999]

The Figures 33 and 34 show the proton spectra utilizing the boxes from Figure 32. For comparison the calculate flux from [Droege, 1999] is shown for HELIOS A. The discrepancies can most likely be explained by different chosen time windows.

The fluxes from box 9 in Figure 33 and 34 have an unknown contribution of high energy electrons, as those are believed to be prevalent at similar events [Kühl et al., 2017].

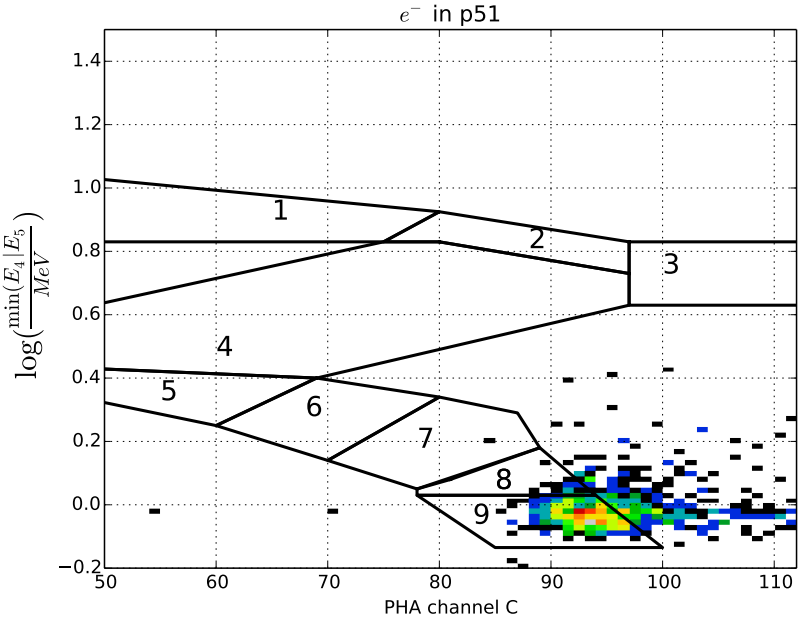

Figure 32: histogram of the energy deposit of $>$ 10 MeV electrons in the minimum of detectors 4 or 5 versus C. Also shown are the boxes for the event analysis.

The spectra are divided in three time intervals: The spectrum before the event is shown in green, the early phase of the event in red and the late phase in cyan. A higher time resolution is difficult to achieve because of the bad statistics for the PHA data, which is needed for the spectra.

The spectra from both spacecrafts show a large contribution above 1 GeV in the early phase of the event, which may be explained by $>$ 10 MeV electrons being misidentified as protons. Particles arriving at Earth at this energies typically cause a GLE, which indeed has been observed for this event.

After it has already been shown that the HELIOS E6 provided unique and reliable data, this example shows that HELIOS E6 data can also be relevant for the investigation of event properties like their spread, energy spectra and time profiles.

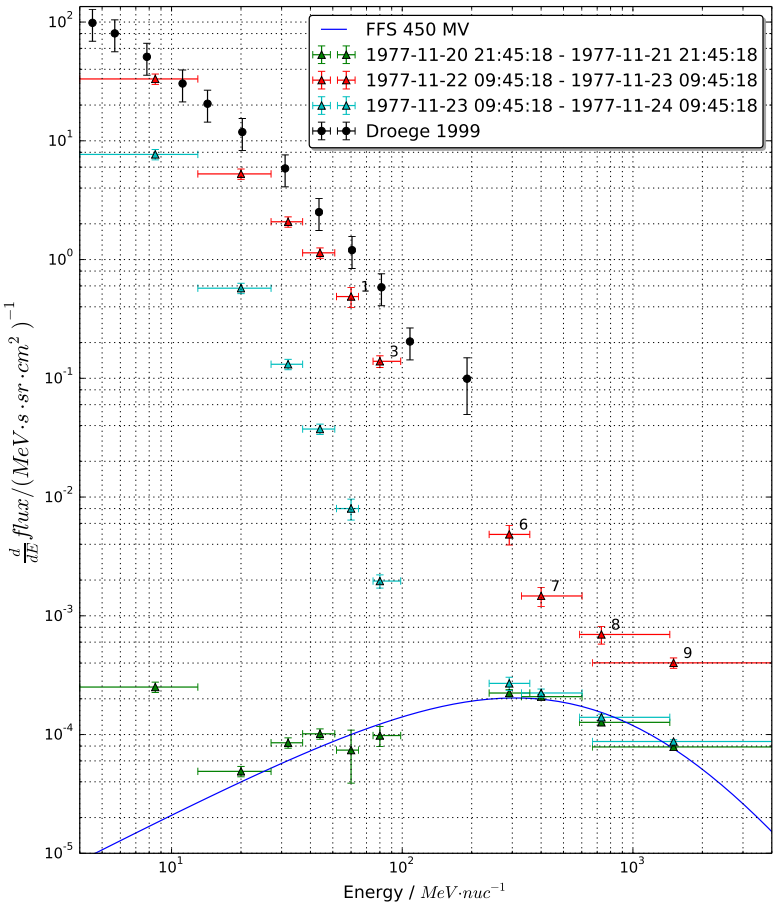

Figure 33: Spectrum of the E6 on HELIOS A during the event from 22.11.1977. Spectrum before the event is shown in green, the early phase of the event in red and the late phase in cyan. In black the spectrum from Droege [1999]. The numbers correspond to the used boxes from section 6.2.

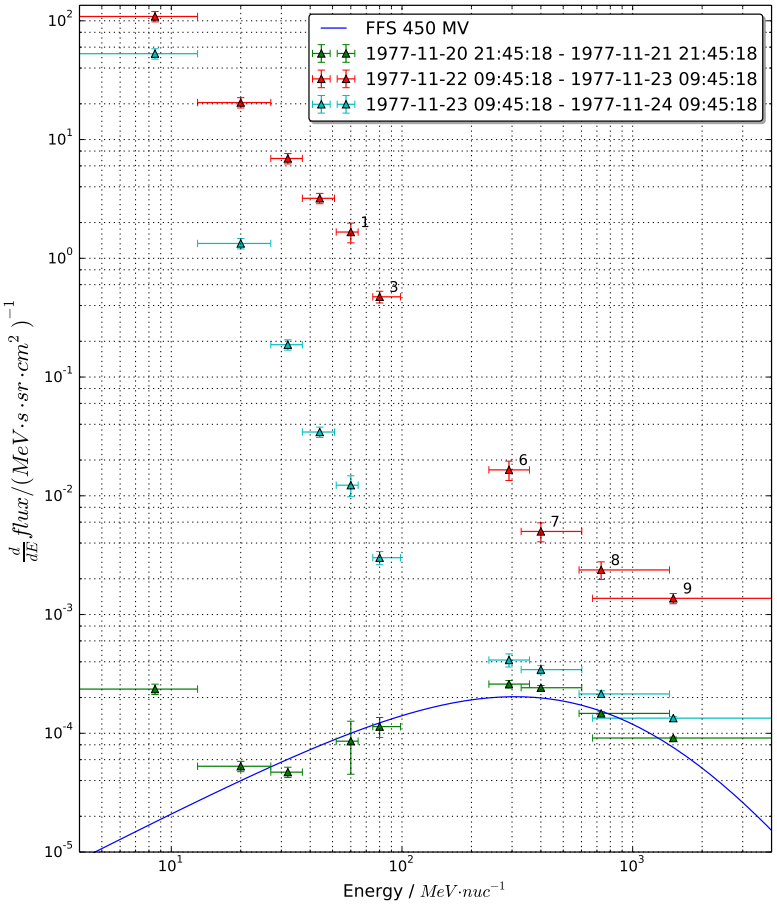

Figure 34: Spectrum of the E6 on HELIOS B during the event from 22.11.1977. Spectrum before the event is shown in green, the early phase of the event in red and the late phase in cyan. The numbers correspond to the used boxes from section 6.2.

7

SUMMARY AND OUTLOOK

In order to better understand the modulation of charged particles in space, one needs to take into account every performed measurement there is.The HELIOS mission provides valuable data because of its unique orbit and operation time. It has been shown that by thoroughly re-analysing the data important physical quantities can still be derived. Since even after data from Solar Orbiter and Parker Solar Probe will be acquired, HELIOS will still be the only spinning twinned spacecraft measuring in the inner heliosphere, making it's data suitable for a wide variety of studies.

To derive physical quantities from the data, several effects had to be corrected for:

- differences in the temperature dependence of the detectors
- effects on the edges of the first two detectors
- degradation of the C-detector
- differences in the processing of Cerenkov and scintillation light because of the different wave-lengthes from the PMT
- saturation of the PMT
- consideration and determination of quenching properties of the C-detector
- contamination with backward particles and particles of a different species for the integral coincidence logic

Based on those corrections first the possibility of chemical abundance studies has been investigated. It was found that the E6 was capable of gathering enough data to show the abundances of primary GCR elements from H to Si and also to generate energy spectra.

Secondly the effects of solar modulation of ACR oxygen particles has been investigated and the gradient for anomalous oxygen has been determined for the first time in the inner heliosphere and is with $(48 \pm 12)\%/\mathrm{AU}$ much steeper than expected from measurements in the outer heliosphere. It agrees, however, qualitatively with recent models of solar modulation.

Thirdly the modulation of above 50 MeV hydrogen has been investigated by utilizing the unique sapphire Cerenkov-scintillation detector of the E6. The gradient of galactic hydrogen above 200 MeV has been determined to be $(2 \pm 2.5)\%/\mathrm{AU}$. This value agrees quite well with other measurements and predictions.

Another discovered point of interest is the changing behaviour of Cherenkov radiation and scintillated radiation. While it still remains unclear what causes their time dependent differences, it is an effect that needs to be considered for other missions that use a Cerenkov-detector.

While there are electron measurements from the E6, only the E08 and E2 channels have usable PHA data. Without this data, the flux is difficult to determine because of the edge effect. Thus it is very difficult to reconstruct the electron flux above 10 MeV, especially since electron event spectra usually can't be described by a single power law.

The quantities derived in this work will provide an important point of reference for all deep space particle measurements as well as an additional point for the development of new models.

BIBLIOGRAPHY

S. Agostinelli. Geant4-a simulation toolkit. *Nuclear Instruments and Methods in Physics Research Section A: Accelerators, Spectrometers, Detectors and Associated Equipment*, 2003.

M. Bialk. *Energiereiche Protonen von 4 - 1000 MeV im inneren Sonnensystem : Messungen des Kieler Teilchenteleskops an Bord der Raumsonden HELIOS 1 und 2*. PhD thesis, Christian-Albrechts-Universität zu Kiel, 1996.

W. Droege. Acceleration of Solar Flare Particles to Relativistic Energies. In *26th International Cosmic Ray Conference (ICRC26), Volume 6*, volume 6 of *International Cosmic Ray Conference*, page 232, Jan 1999.

H. A. Enge. *Introduction to nuclear physics*. Addison-Wesley Pub. Co., London, 1966.

N. J. Fox, M. C. Velli, S. D. Bale, R. Decker, A. Driesman, R. A. Howard, J. C. Kasper, J. Kinnison, M. Kusterer, D. Lario, M. K. Lockwood, D. J. McComas, N. E. Raouafi, and A. Szabo. The solar probe plus mission: Humanity's first visit to our star. *Space Science Reviews*, 204(1):7–48, Dec 2016. ISSN 1572-9672. doi: 10.1007/s11214-015-0211-6. URL https://doi.org/10.1007/s11214-015-0211-6.

J. Fuckner. Entwicklung von Messverfahren und Durchführung von Eichmessungen am HELIOS-Experiment 6. Diplomarbeit, Institut für reine und angewandte Kernphysik der Christian-Albrechts-Universität zu Kiel, 1974.

L. J. Gleeson and W. I. Axford. Solar Modulation of Galactic Cosmic Rays. *Astrophysical Journal*, 154:1011, Dec 1968a. doi: 10.1086/149822.

L. J. Gleeson and W. I. Axford. The Compton-Getting Effect. *Astrophysics and Space Science*, 2(4):431–437, Dec 1968b. doi: 10.1007/BF02175919.

B. Heber. Rechnersimulation der Protonen-Eichmessungen für das Kieler Experiment an Bord der Raumsonde Helios. Saatsexamensarbeit, Institut für reine und angewandte Kernphysik der Christian-Albrechts-Universität zu Kiel, 1989.

B. Heber. Nachweischarakteristik des Kieler Experiment an Bord der Sonnensonde Helios für Protonen im interplanetaren Raum. Diplomarbeit, Institut für reine und angewandte Kernphysik der Christian-Albrechts-Universität zu Kiel, 1991.

M. Hörlöck, B. Heber, J. Marquardt, and P. Kühl. Data based correction of HELIOS E6 Measurements - Proton Contamination of relativistic electron measurements. *Central European Astrophysical Bulletin*, accepted for publication, 2019.

B. Iwers. Energieeichung und Bestimmung des Auflösungsvermögens des HELIOS-Experiments E6 am Hamburger Isochron-Zyklotron. Diplomarbeit, Institut für reine und angewandte Kernphysik der Christian-Albrechts-Universität zu Kiel, 1976.

G. F. Knoll. *Radiation Detection and Measurement*. Wiley, University of Michigan, 3nd edition, 2000.

P. Kühl, N. Dresing, B. Heber, and A. Klassen. Solar Energetic Particle Events with Protons Above 500 MeV Between 1995 and 2015 Measured with SOHO/EPHIN. *Solar Physics*, 292(1):10, Jan 2017. doi: 10.1007/s11207-016-1033-8.

H. Kunow, G. Wibberenz, G. Green, H. Hempe, B. Iwers, R. Mueller-Mellin, M. Witte, J. Fuckner, and A. Popp. Ein Experiment zur Messung der kosmischen Strahlung an Bord der Sonnensonden HELIOS-1 und -2 (Experiment 6). Technical report, Forschungsbericht W 81-016 des BMFT, Aug 1981.

M. S. Longair. *High Energy Astrophysics Volume 1*. Press Syndicate of the University of Cambridge, University of Cambridge, 2nd edition, 1992.

J. Marquardt and B. Heber. Galactic cosmic ray hydrogen spectra and radial gradients in the inner heliosphere measured by the HELIOS Experiment 6. *A&A*, 625:A153, 2019. doi: 10.1051/0004-6361/201935413. URL https://doi.org/10.1051/0004-6361/201935413.

J. Marquardt, B. Heber, M. Hörlöck, P. Kühl, and R. F. Wimmer-Schweingruber. GEANT 4 simulation of the Helios cosmic ray telescope E6: Feasibility of chemical composition studies. *Journal of Physics Conference Series*, 632(1):012016, August 2015. doi: 10.1088/1742-6596/632/1/012016.

J. Marquardt, B. Heber, M. S. Potgieter, and R. D. Strauss. Energy spectra of carbon and oxygen with HELIOS E6 - Radial gradients of anomalous cosmic ray oxygen within 1 AU. *A&A*, 610:A42, 2018. doi: 10.1051/0004-6361/201731490. URL https://doi.org/10.1051/0004-6361/201731490.

R. Mewaldt, 2003. URL http://www.srl.caltech.edu/ACE/ASC/DATA/level3/fluences/.

H. Moraal. Cosmic-ray modulation equations. *Space Science Reviews*, 176(1):299–319, Jun 2013. ISSN 1572-9672. doi: 10.1007/s11214-011-9819-3. URL https://doi.org/10.1007/s11214-011-9819-3.

R. Mueller-Mellin, G. Green, B. Iwers, H. Kunow, G. Wibberenz, J. Fuckner, H. Hempe, and M. Witte. Datenverarbeitung für ein Experiment zur Untersuchung der kosmischen Strahlung an Bord der Sonnensonden HELIOS-1 und -2 (Experiment 6). Technical report, Forschungsbericht W 82-009 des BMFT, Jul 1982.

D. Müller, R. G. Marsden, O. C. St. Cyr, H. R. Gilbert, and The Solar Orbiter Team. Solar orbiter. *Solar Physics*, 285(1):25–70, Jul 2013. ISSN 1573-093X. doi: 10.1007/s11207-012-0085-7. URL https://doi.org/10.1007/s11207-012-0085-7.

NASA, 2004. URL https://heasarc.gsfc.nasa.gov/Images/misc_missions/helios_traj.gif.

E. N. Parker. The passage of energetic charged particles through interplanetary space. *Planetary and Space Science*, 13(1):9–49, January 1965.

N. V. Pogorelov, H. Fichtner, A. Czechowski, A. Lazarian, B. Lembege, J. A. le Roux, M. S. Potgieter, K. Scherer, E. C. Stone, R. D. Strauss, T. Wiengarten, P. Wurz, G. P. Zank, and M. Zhang. Heliosheath Processes and the Structure of the Heliopause: Modeling Energetic Particles, Cosmic Rays, and Magnetic Fields. *Space Science Reviews*, 212(1-2):193–248, Oct 2017. doi: 10.1007/s11214-017-0354-8.

R. Reinhard. Voruntersuchungen für ein Teilchenexperiment an Bord der Sonnensonde (HELIOS). Diplomarbeit, Institut für reine und angewandte Kernphysik der Christian-Albrechts-Universität zu Kiel, 1970.

D. Ruffolo. Effect of Adiabatic Deceleration on the Focused Transport of Solar Cosmic Rays. *Astrophysical Journal*, 442:861, Apr 1995. doi: 10.1086/175489.

E. T. Sarris, S. M. Krimigis, and T. P. Armstrong. Observations of magnetospheric bursts of high-energy protons and electrons at 35 re with imp 7. *Journal of Geophysical Research (1896-1977)*, 81(13):2341–2355, 1976. doi: 10.1029/JA081i013p02341. URL https://agupubs.onlinelibrary.wiley.com/doi/abs/10.1029/JA081i013p02341.

R. Schwenn. Solar wind and its interaction with the magnetosphere: measured parameters. In *The Mesosphere and Thermosphere*, pages 3–17, Jan 1981.

R. Schwenn and E. Marsch. *Physics of the inner heliosphere. 1. Large-scale phenomena.*, volume 20 of *Physics and Chemistry in Space*. Springer-Verlag, 1990. ISBN 3-540-52081-3.

U. K. Senanayake, V. Florinski, A. C. Cummings, and E. C. Stone. Spectral Evolution of Anomalous Cosmic Rays at Voyager 1 beyond the Termination Shock. *The Astrophysical Journal*, 804(1):12, May 2015. doi: 10.1088/0004-637X/804/1/12.

J. A. Simpson. Elemental and Isotopic Composition of the Galactic Cosmic Rays. *Annual Review of Nuclear and Particle Science*, 33:323–382, Jan 1983. doi: 10.1146/annurev.ns.33.120183.001543.

R. D. Strauss and M. S. Potgieter. Modeling anomalous cosmic ray oxygen gradients over successive solar cycles. *Journal of Geophysical Research (Space Physics)*, 115:A12111, December 2010. doi: 10.1029/2010JA015690.

ACKNOWLEDGMENTS

An dieser Stelle möchte ich die Gelegenheit ergreifen, denjenigen zu danken, die mich bei der Erstellung dieser Dissertation mit Rat und Tat über die Jahre unterstützt haben.

An erster Stelle bedanke ich mich bei meinem Doktorvater Prof. Dr. Bernd Heber, der diese Arbeit ermöglicht hat und und jederzeit bereit war, Probleme ausfürlich zu diskutieren und neue Impulse zu geben.

Lars Berger und Patrick Kühl danke ich für mehrfaches, gründliches Korrekturlesen dieser Arbeit.

Carsten Wallmann sah sich neue Ergebnisse meistens als erster an und hat durch seine Kritik die Visualisierung oft deutlich verbessert. Außerdem danke ich ihm für die eine oder andere willkommene Ablenkung.

Der Gruppe Extraterrestrische Physik danke ich für etliche beantwortete Fragen zu einer Vielzahl an Themen.

Zu guter Letzt danke ich meiner Familie, meinen Freunden und meiner Freundin Hanna, die mich in dieser Zeit unermüdlich unterstützt haben.

ERKLÄRUNG

Ich versichere an Eides Statt, dass ich die vorliegende Dissertation in Form und Inhalt eigenständig angefertigt habe. Abgesehen von der Beratung durch meine Betreuer und der angegebenen Literatur wurde die Arbeit ohne fremde Hilfe erstellt. Ich versichere, dass ich keine andere als die angegebene Literatur verwendet habe. Diese Versicherung bezieht sich auch auf alle in dieser Arbeit enthaltenen Grafiken und bildlichen Darstellungen.

Die Arbeit als Ganzes wurde bisher keiner anderen Prüfungsbehörde vorgelegt. Teile der Arbeit wurden bereits in Fachzeitschriften veröffentlicht und sind als solche gekennzeichnet. Die Quellennachweise der in den einzelnen Veröffentlichungen referenzierten Inhalte finden sich in der jeweiligen Veröffentlichung selbst und werden nicht zusätzlich im Quellennachweis dieser Arbeit aufgeführt. Für das Einbinden der Veröffentlichungen in diese Arbeit wurde die ausdrückliche Genehmigung der publizierenden Fachzeitschrift eingeholt.

Ich erkläre abschließend, dass die Arbeit unter Einhaltung der Regeln guter wissenschaftlicher Praxis der Deutschen Forschungsgemeinschaft entstanden ist. Mir wurde kein akademischer Grad entzogen.

Kiel, 2019

Johannes Marquardt